SANDIA REPORT

SAND2018-13304
Unlimited Release
Printed March 2018

High Resolution Measurements and Modeling in the Arctic

Erika L. Roesler, Ben Hillman, Dari Dexheimer, Lauren Dennis, Matthew McChesney, Jasper Hardesty, Siddharth Namachivayam, Akshay Jain

Prepared by
Sandia National Laboratories
Albuquerque, New Mexico 87185 and Livermore, California 94550

Sandia National Laboratories

Issued by Sandia National Laboratories, operated for the United States Department of Energy by National Technology and Engineering Solutions of Sandia, LLC.

Available to DOE and DOE contractors from
U.S. Department of Energy
Office of Scientific and Technical Information
P.O. Box 62
Oak Ridge, TN 37831

Telephone: (865) 576-8401
Facsimile: (865) 576-5728
E-Mail: reports@osti.gov
Online ordering: http://www.osti.gov/scitech

Available to the public from
U.S. Department of Commerce
National Technical Information Service
5301 Shawnee Rd
Alexandria, VA 22312

Telephone: (800) 553-6847
Facsimile: (703) 605-6900
E-Mail: orders@ntis.gov
Online order: https://www.classic.ntis.gov/help/order-methods/

SAND2018-13304
Printed June 2018
Unlimited Release

High Resolution Measurements and Modeling in the Arctic

Erika L. Roesler, Ben Hillman, Dari Dexheimer, Lauren Dennis,
Matthew McChesney, Jasper Hardesty, Siddharth Namachivayam, Akshay Jain
Department of Atmospheric Sciences
Sandia National Laboratories
P.O. Box 5800
Albuquerque, NM 87185-9999

Abstract

This report details the activity of the project, "High Resolution Modeling and Measurements in the Arctic" spanning Fiscal Years 2016 - 2018 supported by the Sandia National Laboratories Laboratory Directed Research and Development (LDRD) program. The project's primary goal was to test the hypothesis that global climate model bias of low boundary layer clouds lacking liquid water in the Arctic could be improved by increasing horizontal resolution in the model. As model resolution is constrained by computational resources, four different model types were explored and compared to test the project's primary theory. Given the Arctic is a data-sparse region lacking robust data sets of liquid water in clouds, this project also obtained *in situ* measurements of low clouds with sensors on a tethered balloon system to constrain and compare with the models. Although other model biases remained, the liquid water path generally increased with resolution, supporting the original hypothesis.

Acknowledgments

This work is funded by the Sandia National Laboratories Laboratory Directed Research and Development (LDRD) program.

The data sources were many, and each are acknowledged. Data sources include the NOAA High Resolution sea surface temperature data provided by the NOAA/OAR/ESRL PSD, Boulder, Colorado, USA, from their Web site.[1] Data was also obtained from NOAA coop weather stations in Alaska.[2] The Atmospheric Radiation Measurement (ARM) User Facility, a U.S. Department of Energy (DOE) Office of Science user facility managed by the Office of Biological and Environmental Research, was also a primary source of data. Specific DOIs for the data streams will be given in peer-reviewed editions of this work. The World Climate Research Programme's Working Group on Coupled Modeling, which is responsible for CMIP, and the associated climate modeling groups, such as NCAR's CCSM and DOE's E3SM, are acknowledged for producing and making available their model output. For CMIP, the U.S. Department of Energy's Program for Climate Model Diagnosis and Intercomparison provides coordinating support and led development of software infrastructure in partnership with the Global Organization for Earth System Science Portals. CALIPSO satellite retrieval data was obtained from the IPSL ClimServ[3], who provide the CALIPSO data product for the Cloud Feedback Model Intercomparison Project (CFMIP). We would like to acknowledge the European Centre for Medium-Range Weather Forecasts (ECMWF) for providing the ERA-Interim.[4] Finally, data was obtained from the Arctic System Reanalysis.[5]

We would like to thank the Department of Energy's Atmospheric Radiation Measurement Program and staff that made data collection in extreme environments which include Casey Longbottom, Monty Apple, Jasper Hardesty, Fred Helsel, Todd Houchens, Dan Lucero, Ben Bishop, Al Bendure, Bruce Edwardson, and Erich Havner. The aforementioned operators provided many of the photos taken at Oliktok Point that are used in this report. We would like to thank Mark Ivey, Mark Taylor, Mark Boslough, Bill Spotz, Oksana Guba, Pete Bosler, Andrew Bradley, Andrew Stayer, Micheal Deakin, and Greg Barnett for helpful discussions along the way. We would also like to thank Thomas Ackerman, Gijs de Boer, Lori Parrott, Amy Halloran, Erik Webb, Peter Davies, and Marianne Walk for their helpful discussions, vision, and support in this project.

We would also like to thank our SO and OS for their support during this project.

---

[1] `http://www.esrl.noaa.gov/psd/`

[2] `https://wrcc.dri.edu/summary/Climsmak.html`

[3] `http://climserv.ipsl.polytechnique.fr/cfmip-obs/Calipso_goccp.html`

[4] `http://rda.ucar.edu/#!lfd?nb=y&b=proj&v=ECMWF\%20Interim\%20Reanalysis`

[5] `http://rda.ucar.edu/datasets/ds631.0/`

Contents

Appendix

List of Figures

List of Tables

Nomenclature

Abbreviation	Definition
AFZ	Arctic Frontal Zone
AGL	Above Ground Level
AGCM	Atmospheric General Circulation Model
AMF-3	ARM Mobile Facility - 3
AO	Arctic Oscillation
ARM	Atmospheric Radiation Measurement
ARMBE CLDRAD	ARM Best Estimate Cloud Radiation Value Added Product
ASR	Arctic System Reanalysis
BER	Biological and Environmental Research
CCSM	Community Climate System Model
CESM	Community Earth System Model
DOE	Department of Energy
DOY	Day of Year
DTS	Distributed Temperature Sensor
E3SM	Energy Exascale Earth System Model
ECMWF	European Climate Modeling and Weather Forecasting
EMI	Electromagnetic Interference
ERASMUS	Evaluation of Routine Atmospheric Sounding Measurements using Unmanned Systems
ERA	ECMWF Re-Analysis
FORJ	Fiber Optic Rotary Joint
GCM	Global Climate Model
GUI	Graphical User Interface
ICARUS	Inaugural Campaigns for ARM Research using Unmanned Systems
KAZR	Ka-band ARM zenith radar
LASSO	LES-ARM Symbiotic Simulation and Observation
LES	Large Eddy Simulation
LWC	Liquid Water Content
LWS	Leaf Wetness Sensor
MMF	Multi-scale Modeling Framework
MWR	Microwave Radiometer
MSL	Mean Sea Level
NAO	North Atlantic Oscillation
NSA	North Slope of Alaska
RAOB	Universal RAwinsonde OBservation program
RF	Radio Frequency
RRM	Regionally Refined Model
RWB	Rosby Wave Breaking
SGP	Southern Great Plains
SLWC	Supercooled Liquid Water Content
SP	Superparameterization
SST	Sea Surface Temperature
TBS	Tethered Balloon System
UAS	Unmanned Aerial Systems
VIPS	Video Ice Particle Sensor

Chapter 1

Introduction

Surface temperatures in the Arctic are increasing more rapidly in comparison with the rest of the globe (Forster et al., 2007; Trenberth et al., 2007), a phenomenon often referred to as Arctic Amplification.

Due to the remoteness and inaccessibility of the Arctic region, documentation of these environmental changes and even of the general climatology of the Arctic is limited compared with more accessible locations around the globe. The extreme terrain and harsh winters in the Arctic limit the timespan and conditions under which extensive measurements can be taken. Not only are individual observations and campaigns relied upon more heavily, but more dependency is placed upon models to provide an estimate of climatological conditions in areas without measurements. Because of this, it is important to determine whether models accurately represent actual climatological conditions in the Arctic. In order to gain more knowledge of particular Arctic phenomena that are not currently well understood, both measurements and modeling are used. In this pursuit, it is imperative to compare models and measurements in an effort to understand the true conditions in the Arctic.

The presence and properties of clouds are important for modulating radiative fluxes. The phase of these clouds are particularly important because liquid and ice clouds have different radiative properties. Liquid-containing clouds at temperatures below the freezing level (i.e., supercooled liquid) are common in the Arctic, but these clouds have traditionally been difficult to simulate in large-scale models of the atmosphere. Much work has gone into understanding of the processes important to the formation and maintenance of supercooled liquid clouds but our understanding of these processes is still limited and not well-represented in large-scale atmospheric models (Morrison et al., 2012).

Low clouds show the most climate sensitivity to increased greenhouse gas concentrations (Brient and Schneider, 2016; Schneider et al., 2017). In the data poor region of Arctic where climate is changing rapidly, the change in low cloud cover is unknown and uncertain under increasing greenhouse gas concentration scenarios. How the clouds will respond and how they will change the energy budget of the Arctic are open questions. However, the tool to answer this question (i.e., global climate models (GCMs)) cannot resolve low clouds and currently represent them through parameterizations. The spatial resolution needed is akin to a global Large Eddy Simulations (LES) with tens to hundreds of meters horizontal grid spacing. This ability might not be possible until 2060 when computing resources and algorithms are developed to support this resolution (e.g.

Schneider et al., 2017). Still, global LES might not be needed everywhere, just in places that are data-rich and with high cloud sensitivities. Ideally, these places would be representative of cloud regimes seen elsewhere on the planet. This idea is in practice at the Department of Energy (DOE) Atmospheric Radiation Measurement (ARM) program, at several fixed and mobile sites located in various cloud regimes, such as on the North Slope of Alaska (NSA). One assumption is that clouds observed and measured at these sites would provide knowledge that could be applied to similar cloud systems elsewhere on the planet.

The purpose of this work is to begin to understand how global LES simulations might represent Arctic low clouds before such a model exists by bridging different models with different resolutions together under similar conditions to understand their ability to represent low clouds. These models are constrained and compared against measurements from the NSA and satellites. Figure 1.1 graphically summarizes the model configurations used in this project to test from low resolution atmospheric general circulation models (AGCMs), to variable resolution AGCMs, to AGCMs with multi-scale convection through a superparameterization, to LES. This report documents analysis of global and local datasets from models and measurements over the North Slope of Alaska with the singular goal of improving the current state of knowledge of low clouds in that region.

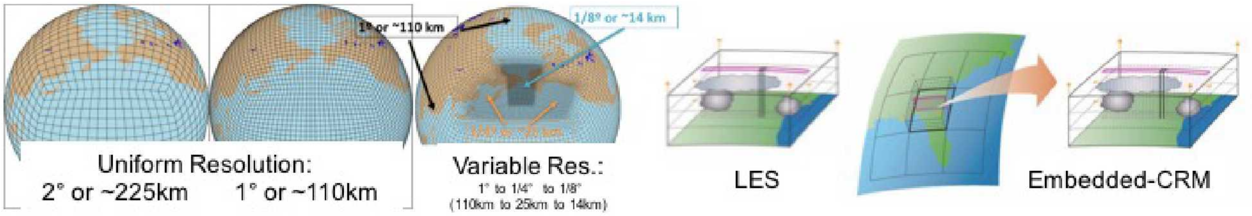

Figure 1.1. Model configurations proposed to be used in the project. From left to right, uniform 2° resolution, uniform 1° resolution, variable resolution with resolutions denoted in the subfigure, LES, and superparameterization.

Project goals included comprehensive measurements and modeling to answer the overarching question: "Can model bias in low-level Arctic cloud amount be reduced by increasing model resolution?" Measurements are performed to constrain the models.

For the modeling portion of this project, the hypothesis is that the kinetic-energy (KE) spectrum becomes more broad with higher resolutions as larger magnitudes of vertical velocities are produced in the model. These larger magnitudes of vertical velocities drive a more energetic cloud in the boundary layer, accessing water vapor sources to maintain a non-zero liquid water path. Two types of models with the ability to run with multiple resolutions are used to test this hypothesis. These models include limited-domain Large Eddy Simulations (LES) and global atmospheric models. Different configurations of the global atmosphere models are used. These are further described in the following chapters.

For the measurement portion of this project, more cloud liquid water datasets are needed. Although instrumentation exists that gives liquid water as a calculated data product based on retrievals from radiometric instrumentation and algorithms, these data products contain large uncertainties as they are based on assumptions of the environment that may be uncharacteristic of the Arctic. Thus, more information is needed to understand model bias. New instrumentation and sensors were used in this project to take *in situ* measurements of cloud properties using a tethered balloon system. This work is described in Chapter 3.

Chapter 2

Comparison of Cloud-Related Climatology of the North Slope of Alaska using ARM Data, ERA-Interim Reanalysis Data, and CCSM CMIP5 Data to Inform Regionally Refined Model Simulations

2.1 North Slope Climatology in Reanalysis, Climate Models, and ARM Data

The Arctic has been identified as a site of rapid environmental change compared with the rest of the globe, and an important site of study as work is performed to understand how increased greenhouse gas emissions will alter the region's climate. Due to the remoteness and inaccessibility of the Arctic region, documentation of these environmental changes and even of the general climatology is limited compared to more populous and accessible locations around the globe. The difficult terrain and harsh winters in the Arctic limit the timespan and conditions under which measurements can be taken. Not only are individual observations and campaigns relied upon more heavily, but more dependency is placed upon models to provide an estimate of climatological conditions in areas without measurements. Because of this, it is important to determine how accurate models represent climatological conditions in the Arctic. In order to gain more knowledge of particular Arctic phenomena (i.e., the representation of low-level Arctic clouds) that are not currently well understood, both measurements and modeling are used. In this pursuit, it is imperative to compare models and measurements in an effort to understand the true conditions in the Arctic. The work for this project focuses on one region of the Arctic: the North Slope of Alaska.

The climate of the North Slope of Alaska (NSA) is affected by several persistent weather patterns and topographical features. Figure 2.1 pictorially highlights these features. The NSA is a coastal region, and persistent weather patterns include changing sea ice and sea surface temperatures. The topography of Alaska, such as the Brooks Range, the coast of Siberia (causing differential heating), and the southern Alaskan coastal terrain (causing wind) affect the region's climate (Hughes and Cassano, 2015). The Aleutian Islands, on which a semipermanent low resides, can act as guides or blocks for moisture transport, Rossby wave breaking, and cyclones into the Bering Strait. The Bering Strait itself also has variable sea surface temperatures and sea ice coverage (Carton et al., 2015; Hughes and Cassano, 2015; Liu and Barnes, 2015).

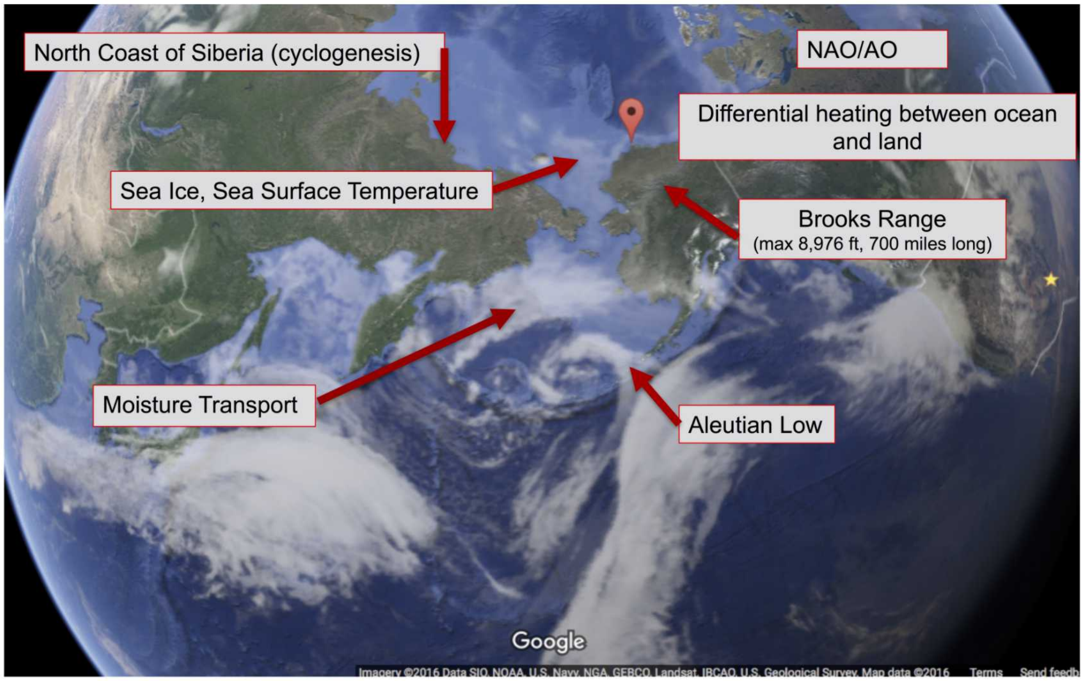

(Serreze et al. 2001, Vavrus 2013, Crawford and Serreze 2014, Carton et al. 2015, Liu and Barnes 2015, F. Krikken and W. Hazeleger 2015)

Figure 2.1. Persistent weather and climatology features that affect the climate of the North Slope of Alaska.

Major mechanisms of variability include the Arctic Frontal Zone (AFZ), moisture fluxes from Rossby Wave Breaking (RWB), and the North Atlantic Oscillation (NAO)/Arctic Oscillation (AO).

The Arctic Frontal Zone (AFZ) is a narrow band of strong horizontal temperature gradients resulting from differential atmospheric heating between the Arctic Ocean and snow-free land (Crawford and Serreze, 2014). The ocean surface stays relatively cool compared to the strong heating of the land surface, and this differential heating creates an Arctic jet-like feature at about 250 hPa. The feature is most noticeable in July. The AFZ is distinct from the polar frontal zone, and it is the origin of cyclones tracking into the Arctic Ocean (Reed and Kunkel, 1960). The summertime AFZ is strongest in Alaska, specifically near the Brooks Range (Crawford and Serreze, 2014). Coastal mountain ranges like the Brooks Range may enhance the AFZ because they prevent cold air from pushing inland (Reed and Kunkel, 1960; Serreze et al., 2001).

Liu and Barnes (2015) found that much of the transient moisture brought into the Arctic is brought from the midlatitudes by extreme moisture events. These events are closely related to Rossby Wave Breaking (RWB), which is responsible for about 68% of extreme poleward moisture transport by transients across 60°N in winter and 56% of extreme poleward moisture transport in summer. This extreme moisture transport maximizes over the North Pacific around the Bering

Strait. Liu and Barnes (2015) found the interannual variability of RWB-related transport is strongly influenced by the El Nino/Southern Oscillation (ENSO) and the North Atlantic Oscillation (NAO), which also tends to shift the midlatitude jet stream.

The North Atlantic Oscillation - Arctic Oscillation (NAO-AO) are two highly correlated standing modes of atmospheric pressure variability in the Northern Hemisphere (Thompson and Wallace, 1998; Deser et al., 2000). The Arctic Oscillation (AO) is the manifestation at the surface of changes in the strength of the polar vortex aloft, and its manifestation is very similar to the North Atlantic Oscillation (NAO) (Thompson and Wallace, 1998). The North Atlantic Oscillation is the main mechanism of variability in the North Atlantic region and is a measure of the oscillation between the Azores high and the Icelandic low resulting in changes to the surface air temperature and precipitation (Hurrell, 1995, 1996). The changing values of sea level pressure during positive and negative phases of these modes contributes to sea ice anomalies (e.g. Fang and Wallace, 1994; Walsh and Sater, 1981) and thus affect the climatology of the North Slope region. Most climate models have documented bias in inability to reproduce the strength and location of the AO dipole when compared to observations (Jin-Qing et al., 2013).

These large-scale Arctic climate features affect the low cloud amount over the North Slope of Alaska by changing the timing, extent, and macrophysical properties such as depth and liquid water content. The presence and properties of the clouds then affect the local energy budget (e.g. Morrison et al., 2012). Relationships between low clouds and sea ice, NAO-AO, and extreme events are beginning to be documented (e.g. Kay et al., 2008). In light of documenting trends and relationships in this region, it is even noted that the characteristic climatology of the Bering Strait (and thus other high latitude areas) might be changing, where as it was a more “Arctic” climate prior to the 1960s and is transitioning to a sub-Arctic-like climate (e.g. Wang et al., 2006).

Prior to creating simulations from the models shown in Figure 1.1, the low-cloud biases in climate models are first quantified by exploring differences between existing measurements and models data sets. In order to investigate the low-cloud climatology of the North Slope of Alaska as depicted by climate models and reanalysis data, historical CMIP5 CCSM simulations (Gent et al., 2011) are compared with ERA-I reanalysis data[1](Dee et al., 2011) at four sites: Barrow, Oliktok, Toolik Lake, and Atqasuk. Barrow and Oliktok are located along coastline while Toolik and Atqasuk are located farther inland. All sites are located north of the Brooks Range in Alaskan tundra (Figure 2.2). The latitudes and longitudes of those site are listed in Table 2.1.

Table 2.1. Latitude and Longitudes of North Slope Sites

Site	Latitude	Longitude
Barrow	71° 19’ 22.8” N	156° 36’ 32.4” W
Oliktok	70° 29’ 42.0” N	149° 53’ W
Atqasuk	70° 28’ 18.5” N	157° 24’ 25.2” W
Toolik	68° 38’ N	149° 36’ W

Given the data sparsity in the Arctic, few surface-based sites have historical, climate-length

---

[1] `http://rda.ucar.edu/#!lfd?nb=y&b=proj&v=ECMWF\%20Interim\%20Reanalysis`

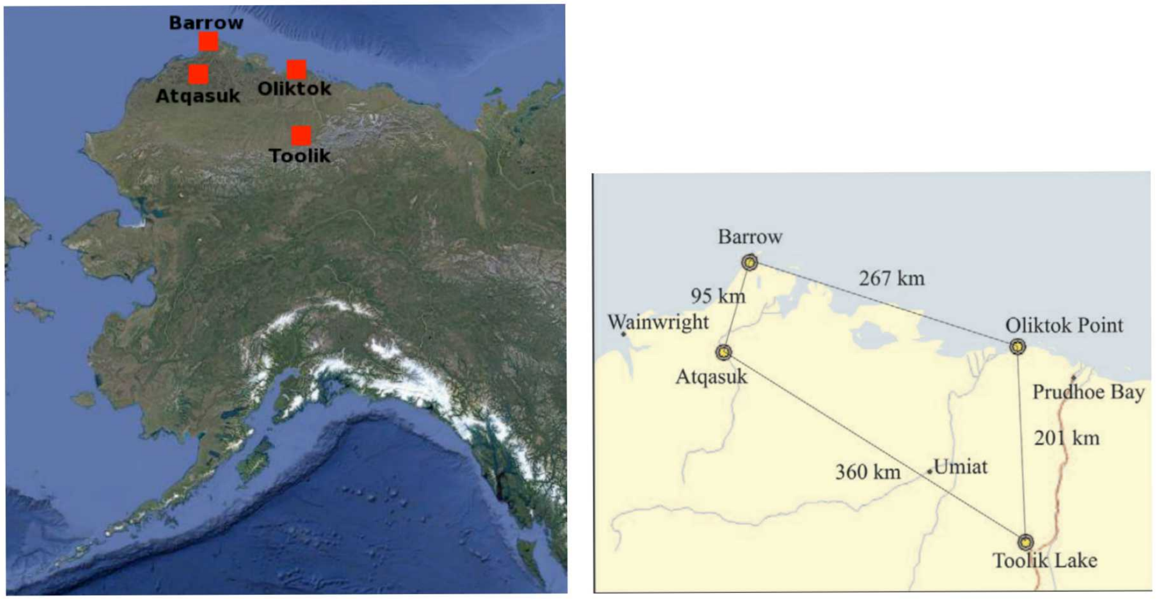

(a) (b)

Figure 2.2. Four research sites on the North Slope of Alaska (a) and the distances between the sites (b). The Barrow and Oliktok sites are actively operated by ARM but the Atqasuk site is now dormant. The Toolik Lake site is operated by the National Science Foundation.

data available (i.e., 10 or more years). The ARM Climate Research Facility's North Slope of Alaska site has been collecting data since 1996 giving twenty years of data, so it is a good source to compare with model data from CMIP5 CCSM simulations and reanalysis from ERA-I. The ARM Climate Research Facility "is a multi-platform scientific user facility with the objective of providing a detailed and accurate description of the Earth's atmosphere in diverse climate regimes to resolve the uncertainties in climate and earth system models."[2] The site has "*in situ* and remote sensing observatories designed to improve the understanding and representation, in climate and earth system models, of clouds and aerosols as well as their interactions and coupling with the Earth's surface." ARM sites on the North Slope of Alaska region have included Barrow, Oliktok, and Atqasuk. These sites have both *in situ* and remote sensing technologies which provide data in order to better understand cloud and radiative processes at high latitudes. These sites are managed by Sandia National Laboratories and collaboration occurs between researchers from national laboratories, universities, military entities, and others.

The ARM Decadal vision contains plans for creating high-resolution modeling areas, called 'megasites', over its sites that are complementary to the data collection activities (ARM Decadal Vision Report, 2014). A megasite program has started with the LASSO (LES-ARM Symbiotic Simulation and Observation) project over the Southern Great Plains (SGP) ARM site in Oklahoma.[3] The LASSO project uses high resolution modeling output along with ARM observations in order to create high resolution data packages that could be used by the climate research community to better understand local climate-relevant processes. A megasite over the NSA presents different challenges than the megasite over the SGP which include the coastal interface, varied surface conditions, and harsher climate for modeling and data collection.

In addition to understanding the climatologies of the North Slope with different data sets, this project also seeks to understand climatological differences (if any) between potential data collection sites for a potential North Slope modeling megasite. The active and inactive ARM sites of Barrow, Oliktok, Atqasuk, and NSF site of Toolik Lake (Figure 2.2) could become a megasite which would combine observational data and high resolution modeling, which then seeds this project's primary goal of understanding low cloud representation in AGCMs in for a future global LES model.

The ERA-I reanalysis data spans from 1979-2012, and the historical CMIP5 CCSM simulations span from 1850-2005. A shared timeframe of 1979-2005 can be used to compare the models and reanalysis. However, only the years 2000-2005 can be compared between the NSA ARM data, ERA-I reanalysis data, and CMIP5 CCSM simulation data. This time range is shorter than the desired 10 years. Years 1996-1999 cannot be included from the ARM data stream because of inconsistencies in data collection at the NSA ARM site.

Reanalysis data from ERA-I has similarities to the GCM data from CCSM. Both use a global model, but reanalysis data regularly receives observational data and ingests it into its output. The global model, on the other hand, is initialized with idealized but characteristic conditions and allowed to run nearly freely for a given duration of time. To further explain their differences, the

---

[2] `http://www.arm.gov/`

[3] `https://www.arm.gov/capabilities/modeling/lasso/`

creation of ERA-I data is described as follows: (from Dee et al. (2011))

> [abbr.] A sequential data assimilation scheme is used which advances forward in time using 12-hourly analysis cycles. In each cycle, available observations are combined with prior information from a forecast model to estimate the evolving state of the global atmosphere and its underlying surface. The algorithm then computes a variational analysis of the basic upper-air atmospheric fields (temperature, wind, humidity, ozone, surface pressure), followed by separate analyses of near-surface parameters (2 m temperature and 2 m humidity), soil moisture and soil temperature, snow, and ocean waves. These analyses are then used to initialize a short-range model forecast, providing the prior state estimates needed for the next analysis cycle. It is inferred that the model equations make it possible to extrapolate information from locally observed parameters to unobserved parameters in a physically meaningful way, and also to carry this information forward in time. The skill and accuracy of forecast model determines how well assimilated information can be retained: the better the model, the smaller adjustments made to match observations over time. The model also estimates physical parameters which may not be observed but are constrained by observations used when initializing the forecast (precipitation, turbulent fluxes, radiation, cloud properties).

Thus, ERA-I still has model biases. It is a reanalysis data product that takes available observations and prior information from a forecast model to estimate the evolving state of the global atmosphere and surface. There is a new parametrization to allow supersaturation with respect to ice in the cloud-free part of a grid-box at temperatures lower than 250K to increase the relative humidity. This parameterization assumes that ice nucleation and growth time-scales are short compared to model time step, so supersaturation only occurs in clear-sky portion of grid cell (Tompkins et al., 2017). The output has approximately 80 km resolution and 60 vertical levels with 6-hourly 3D variables, 3-hourly surface and 2D variables, and 4D-Vars of the upper-air atmospheric state.

The ERA-I data stream contains notable uncertainty in the Arctic and not all variables produced by reanalysis are equally reliable. The ERA-I data may contain biases compared with observational data due to the sparseness of available observational data which causes the reanalysis to be more model-dependent. This means that ERA-I relies more heavily on the model itself and the way it is built (assumptions, etc.) in the Arctic. For example, what Kalnay et al. (1996) describes as class-A variables can be well-defined by observations and can be better represented within reanalysis than observations alone. It is reported by Lindsay et al. (2014) that ERA-Interim reanalysis data is one of the more consistent reanalysis data sets when compared to independent observations in the Arctic area. Although, it also has been found that independent observations such as those taken at the NSA ARM sites can also have bias in cloud variables with height and phase depending upon the type of instrumentation is used (i.e., surface-based versus space-based observations) (Liu et al., 2017).

The CMIP5 CCSM data used was downloaded from the Earth System Grid. The monthly mean history files by decade (1960-2005) for each desired variable were downloaded. Higher frequency (i.e., 3 hourly, 6 hourly, and daily) were available from atmosphere-only type runs, but the full coupled system was needed for this analysis. The files with tags `b40_20th_1d_b08c5cn_139jp.cam2.h0.VARNAME.YYYYMM-YYYYMM.nc`

where VARNAME are all the h0 variables dumped out by the atmosphere model, and where YYYYMM ranges from 185001 to 200512 by decade (ex: 185001-185912) were downloaded. To create the seasonal climatologies, the average monthly data from 1961-2005 was used. Seasonal averages are calculated using a 1961-2005 average.

Variables compared between model and reanalysis include liquid water path, downwelling longwave radiation, the ARM Best Estimate Cloud Radiation Value Added Product (ARMBE CLDRAD), wind velocity, temperature, specific and relative humidity, cloud ice water content, cloud liquid water content, and liquid water path. The ARMBE CLDRAD is made specifically for comparison with global climate models and contains the best estimate of variables measured at the NSA ARM site. When available, hourly liquid water path measurements are averaged by month throughout 2001-2005. Ideally, more sites should be included in the comparison such as Oliktok, Toolik Lake, Atqasuk, and coastal areas around the Bering Strait. As this is not possible due to the short duration of data collection, non-overlapping times in the data sets, incomplete data acquisition, and instrument failure, the conclusions derived from this analysis will be biased towards NSA climatology.

The theory that higher-resolutions could improve climate model bias also spans to reanalysis data. The higher-resolution Arctic System Reanalysis (ASR) data[4] is documented to improve the near surface moisture fluxes and wind fields compared to the global ERA-I (Bromwich et al., 2016) with a horizontal resolution of 30 km. However, ASR does not have speciated cloud variables in its monthly mean files, so it could not be used for this analysis. ASR data has some monthly means, 3-hourly instantaneous snapshots, and variables in 2D and 3D for hindcasting for years 2000 through 2012. The horizontal variability increases in the ASR 30 km data product, and this can be seen in the seasonally-averaged state variables such as temperature, relative humidity, and sea level pressure shown in Figure 2.3 as documentation that this data product was deeply investigated for an Arctic data source before committing to ERA-I.

Specific humidity is measured within CCSM and ERA-Interim as the water vapor content divided by the total air content by mass in each grid box (kg kg^{-1}). Specific humidity was compared at Barrow, Atqasuk, Oliktok, and Toolik by using Q variables from ERA-I reanalysis data and CCSM historical CMIP5 simulation data. Seasonal means from 1979-2005 were calculated from monthly mean ERA-I data for the selected months over the 1979-2005. Seasonal climatologies for CCSM CMIP5 data were also calculated using monthly means. Mean seasonal specific humidity was plotted at each site using NCL by subscripting a site latitude and longitude, for which NCL returned the closest latitude and longitude. The profiles of the seasonal means are shown in Figure 2.4. Specific humidity is higher in CCSM in winter and fall months compared to ERA-I data. In summer and spring months, CCSM specific humidity is lower than ERA-I. The largest difference between the datasets occurs at the Toolik site in summer months, differing around 0.0015 (kg kg^{-1}) at 750 hPa. The difference increases as pressure increases. Differences between specific humidity values of each dataset is smallest during spring months and largest during summer months, and the differences between specific humidity values between the datasets is largest overall for the Toolik

---

[4] `http://rda.ucar.edu/datasets/ds631.0`

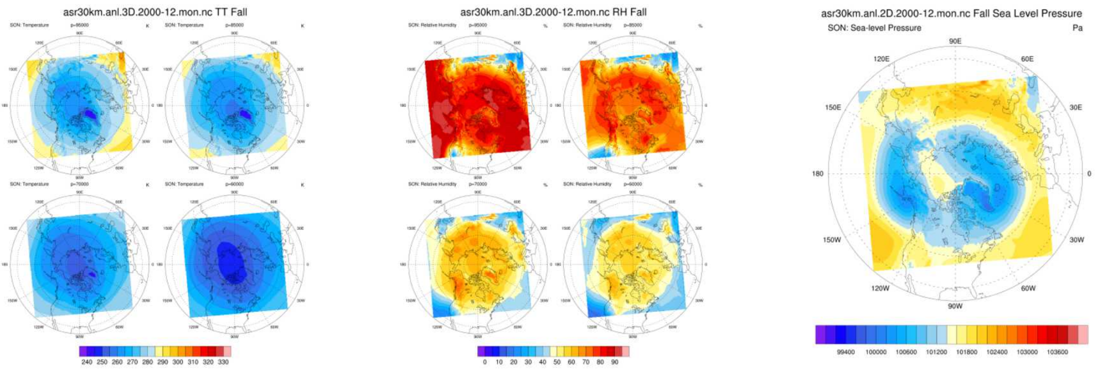

(a) ASR Fall temperature. **(b)** ASR Fall relative humidity. **(c)** ASR Fall sea level pressure.

Figure 2.3. Fall (September, October, November) climatology for temperature (left), relative humidity (middle), and sea level pressure (right) from the ASR data set spanning 2000-2012 for four model level heights (pressures).

site. Winter specific humidity is higher in CCSM compared to ERA-I, especially below 700 hPa. The difference between the actual values appears to be small at around 0.0005 (kg kg^{-1}) for most sites, and the variance through the vertical levels in both variables appears to have similar behavior. Spring specific humidity is lower in CESM CMIP5 historical simulation data compared to ERA-I, especially near the surface where values of specific humidity range from around 0.0008 to 0.00172 (kg kg^{-1}). Summer specific humidity (JJA) is lower in CESM compared to ERA-I, especially at the Toolik site below 700hPa. Fall specific humidity (SON) appears is higher in CESM in comparison ERA-I data at the same sites. Specific humidity appears is higher in CESM in winter and fall months compared to ERA-I data. In summer and spring months, CESM specific humidity is lower in comparison with ERA-I. Specific humidity is largest in summer months at all sites and smallest in winter. At 60 degrees of latitude (north or south), average specific humidity is around 0.004 kg/kg (versus around 0.018 kg/kg at the equator) (Ahrens, 2006).

Figure 2.5 compares temperature between ERA-I and CCSM at the four sites for data from 1979-2005 by atmospheric height. Because the surface of the Arctic is warming and much emphasis is placed on surface temperature increases, Figure 2.1 plots the annual monthly mean surface temperatures from 1960-2005. Toolik and Oliktok are notably warmer at the surface than Barrow and Oliktok during the summer months. During the winter months, the difference in the average surface temperature becomes smaller. A contour plot of the 850 hPa surface temperature by season over the extended North Slope region from CCSM is plotted in Figure 2.1, which shows the spatial variability over this area.

Relative humidity is measured in CCSM and ERA-Interim as the amount of water vapor in a grid cell divided by the amount of water vapor that would be needed to reach saturation at that temperature, represented as a percentage. Relative humidity was compared at Barrow, Atqasuk, Oliktok, and Toolik by using the RELHUM variable from the CCSM CMIP5 historical simulation

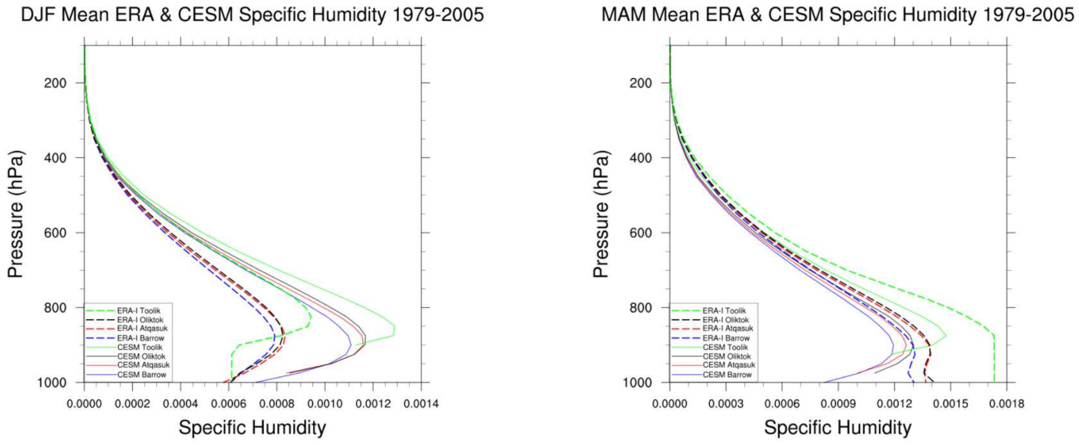

DJF Mean ERA & CESM Specific Humidity 1979-2005

MAM Mean ERA & CESM Specific Humidity 1979-2005

(a) Winter Specific Humidity

(b) Spring Specific Humidity

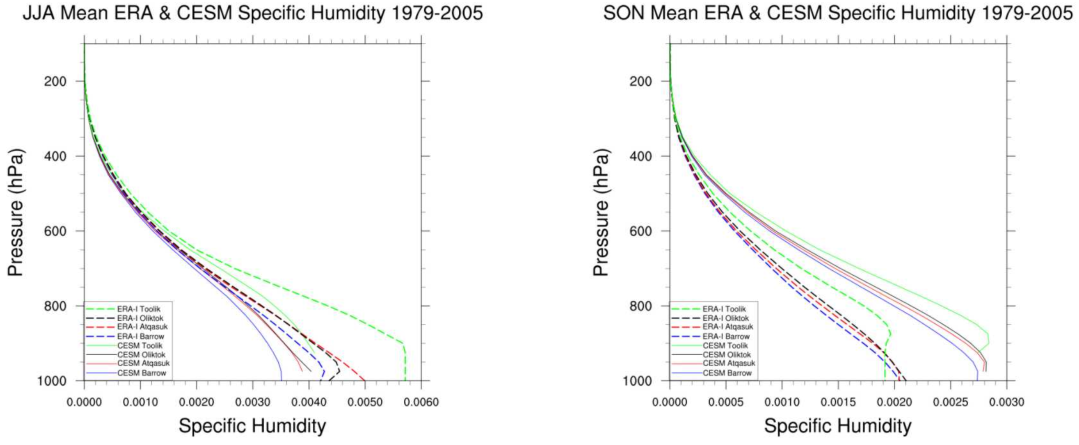

JJA Mean ERA & CESM Specific Humidity 1979-2005

SON Mean ERA & CESM Specific Humidity 1979-2005

(c) Summer Specific Humidity

(d) Fall Specific Humidity

Figure 2.4. Comparison of specific humidity in CMIP5 CCSM4 and ERA-I in seasonal means for Barrow, Oliktok, Atqasuk and Toolik.

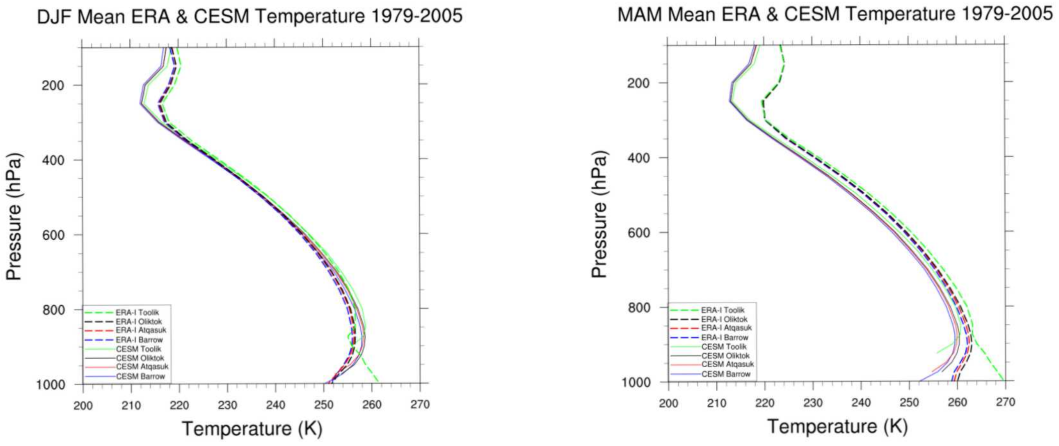

(a) Winter Temperature

(b) Spring Temperature

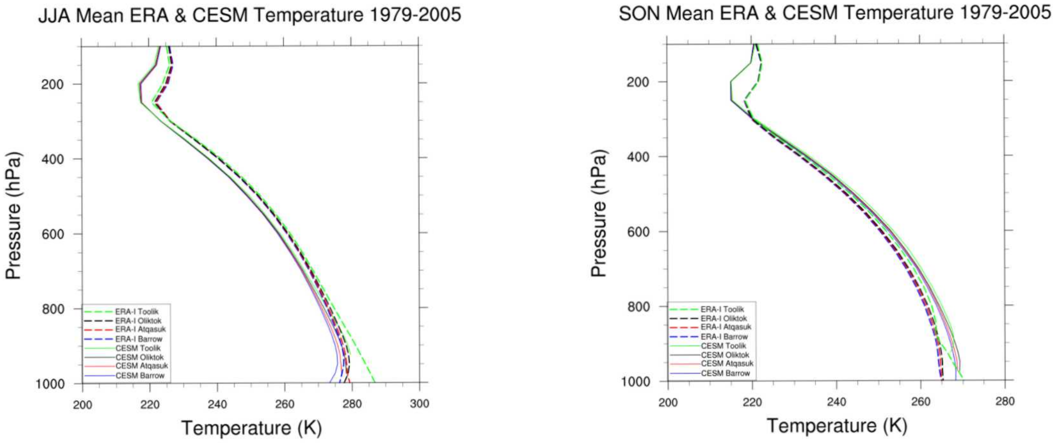

(c) Summer Temperature

(d) Fall Temperature

Figure 2.5. Comparison of temperature in CMIP5 CCSM4 and ERA-I in seasonal means for Barrow, Oliktok, Atqasuk and Toolik.

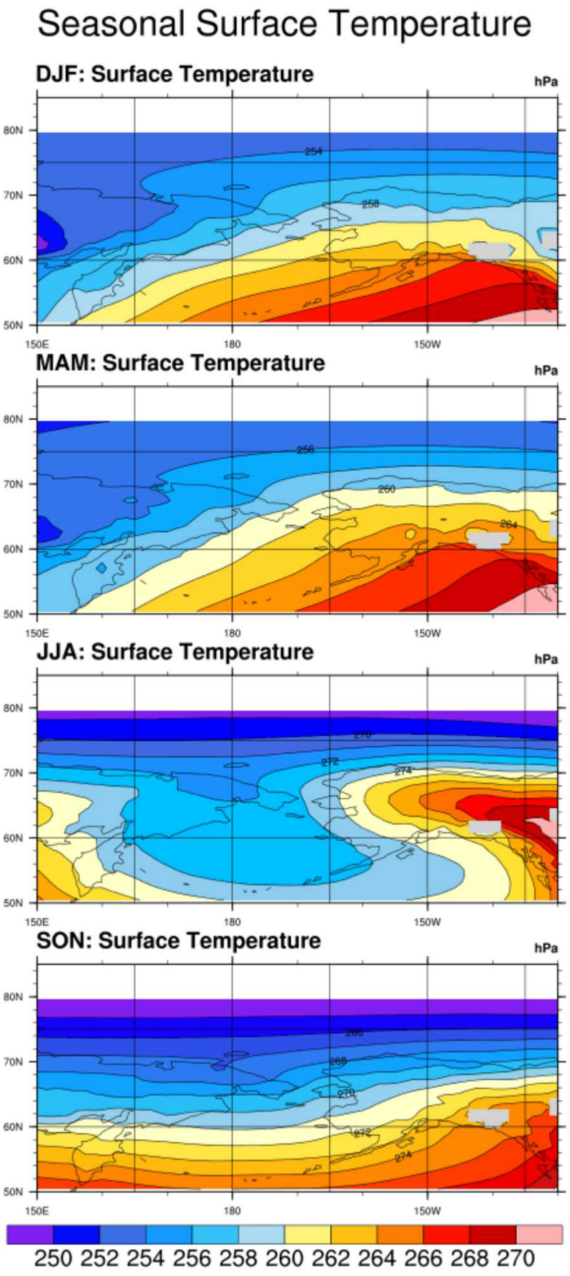

Figure 2.6. Near-surface (850hPa) average temperatures by season from CCSM4.

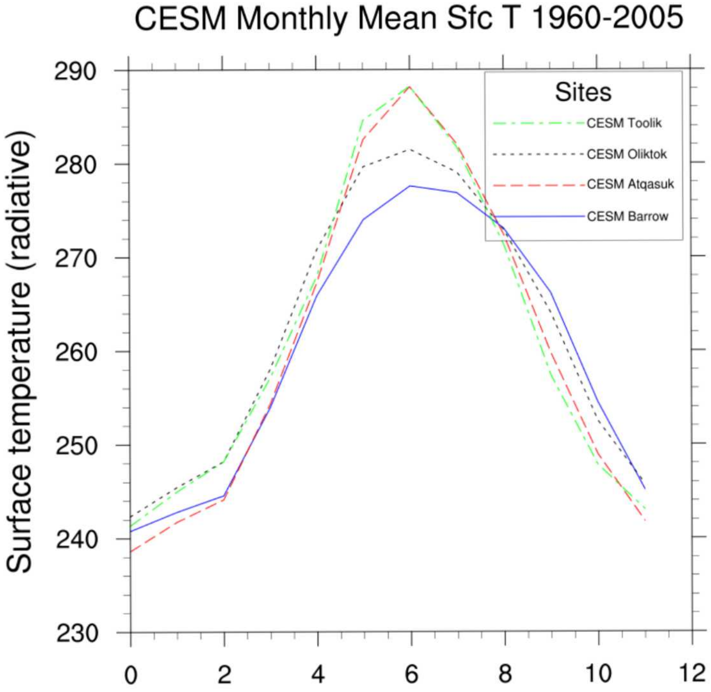

Figure 2.7. Monthly mean surface temperature for Barrow, Oliktok, Atqasuk, and Toolik from the CMIP5 CCSM4 data set. The first month is January, the last month is December.

data and the *R_GDS4_ISBL_S*123CCSM variable from ERA-I reanalysis data. Seasonal means from 1979-2005 were calculated from monthly means. Profiles of these means are shown in Figure 2.8. CCSM historical CMIP5 simulation data generally is higher in magnitude in comparison with ERA-Interim data, especially in fall months. However, in summer months CCSM has lower relative humidity under around 800 hPa, especially for the Toolik site. This measurement at this altitude agrees with the trend observed in specific humidity, in which CCSM consistently is lower in comparison with ERA-I in summer. However from around 750-300hPa, relative humidity is higher, diverging from the trend observed in specific humidity. This might be explained due to the temperature dependence of relative humidity. While CCSM appears to have lower specific humidity during summer and spring months and generally has higher relative humidity except under 850hPa in summer months, ECMWF model and analysis fields are too dry in the upper troposphere (e.g. Tompkins et al., 2017). This suggests that perhaps CCSM has lower humidity except at 850hPa, and is lower than is suggested by the plots shown. Differences in humidity values between the different datasets at all sites are smaller at higher altitudes than at lower altitudes. If ECMWF model and analysis fields are too dry in the upper troposphere, perhaps the difference between actual humidity and that portrayed by CCSM is greater than the difference depicted by comparing CCSM with ERA-Interim.

Wind speed was compared at the four sites from the U and V variables from the CCSM CMIP5 historical simulation data and the ERA-Interim reanalysis data. Seasonal climatologies were calculated from monthly means using the NCO toolbox. Profiles of these means are shown in Figure 2.9 comparing the wind speed and direction between ERA-I and CESM for data from 1979-2005. There are no sweeping determinations that can be made comparing CCSM to ERA-I, and in fact differences between mean wind speed generally tends to be small both between datasets and between sites. Below 500 hPa, mean wind speeds do not appear to reach more than 5 m s^{-1}. Above 500hPa, wind speeds never reach more than 20 m s^{-1} and usually don't reach more than 15 m s^{-1} except in winter. Mean wind speed appears lowest in summer at all altitudes.

From the 500mb winds, it was found the seasonal average wind speed maximums are consistently smaller in CCSM, the seasonal average wind speed minimums are smaller in CCSM in winter, spring, summer and fall. Table 2.2 lists the magnitude of the season's minimum, maximum, and standard deviation in the datasets. Also, the standard deviation between average grid wind speeds is larger in ERA-I than in CCSM. Wind pattern means in the datasets around the North Slope are shown in Figure 2.9.

Cloud liquid water content is the measurement of the amount of cloud liquid per grid box. This is a measurement of the mass of liquid per mass of air (kg kg^{-1}). Similarly, cloud ice water content is the measurement of cloud ice water per grid box. Seasonal means were calculated from monthly means at Barrow, Oliktok, Toolik, and Atqasuk. Figure 2.11 compares cloud liquid between ERA-I and CCSM at the four sites for data from 1979-2005, and Figure 2.12 compares cloud ice between ERA-I and CESM at the four sites for data from 1979-2005. Cloud liquid water content is lower in CCSM CMIP5 historical simulations in all months except for fall when compared to the ERA-I. Below 750 hPa, cloud liquid water content is lower in CCSM when comparison with ERA-Interim during the fall. Differences in cloud liquid water content between sites is fairly large. In the CCSM data, Toolik appears to have the most cloud liquid water content except very close to the surface,

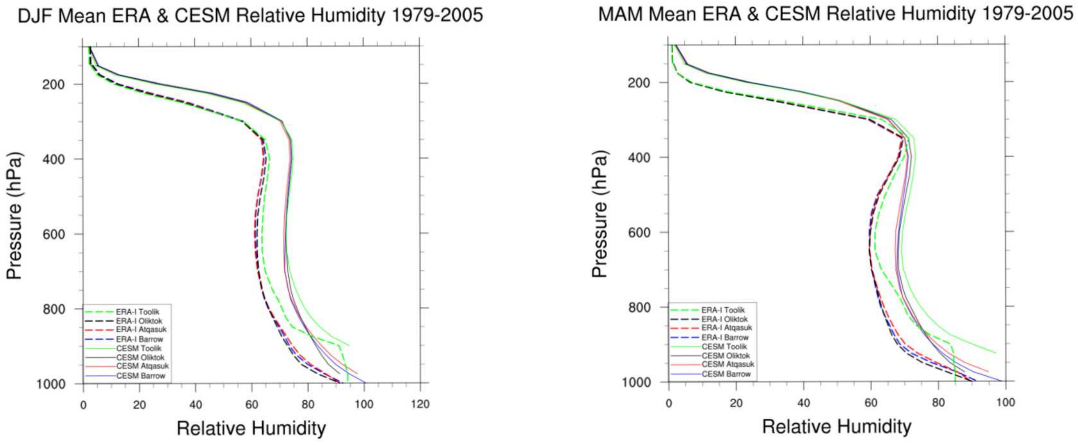

(a) Winter Relative Humidity

(b) Spring Relative Humidity

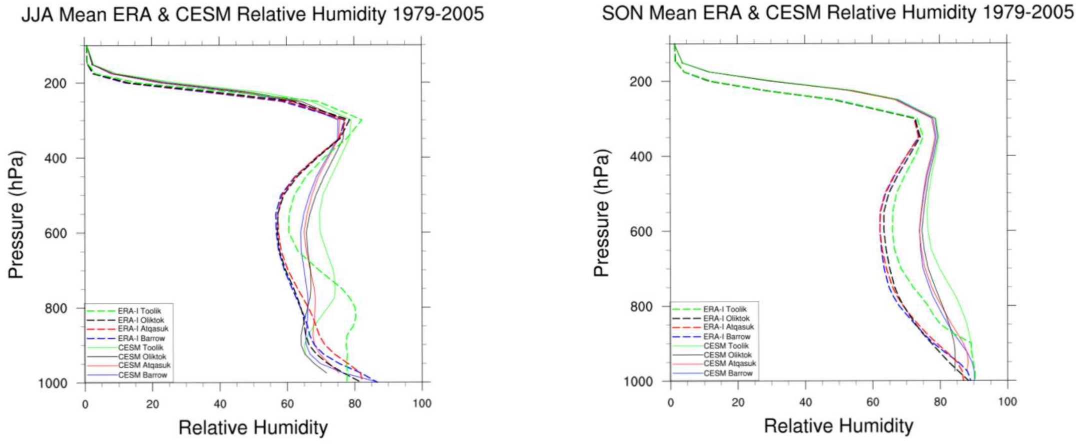

(c) Summer Relative Humidity

(d) Fall Relative Humidity

Figure 2.8. Comparison of relative humidity in CMIP5 CCSM4 and ERA-I in seasonal means for Barrow, Oliktok, Atqasuk and Toolik.

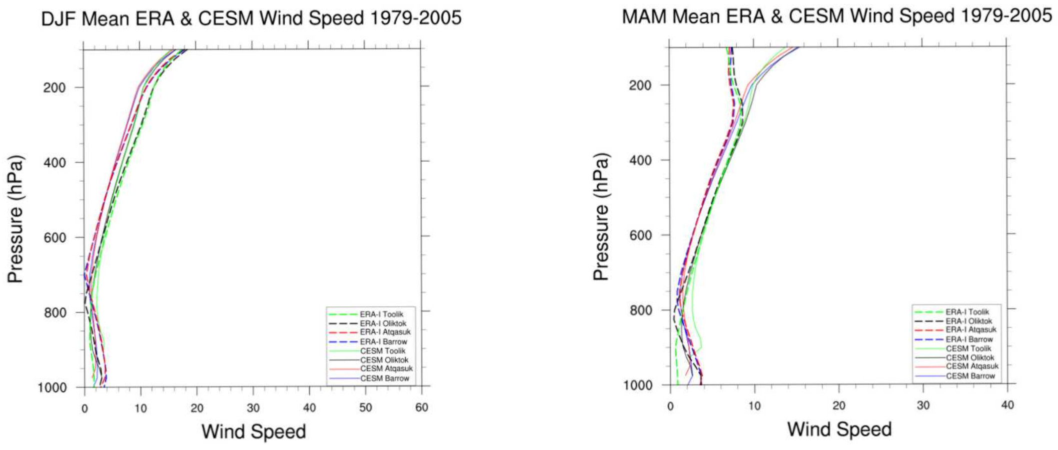

(a) Winter Wind Speed **(b)** Spring Wind Speed

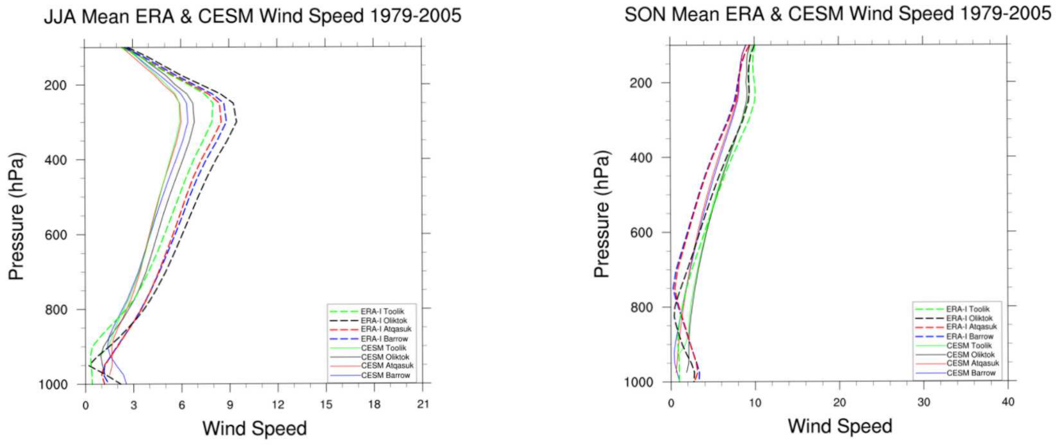

(c) Summer Wind Speed **(d)** Fall Wind Speed

Figure 2.9. Comparison of wind speeds in CMIP5 CCSM4 and ERA-I in seasonal means for Barrow, Oliktok, Atqasuk and Toolik.

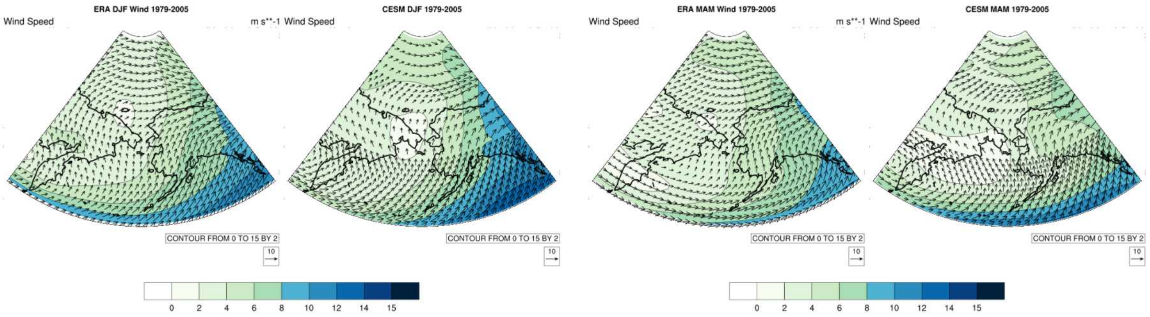

(a) Winter Wind Speed and Direction **(b)** Spring Wind Speed and Direction

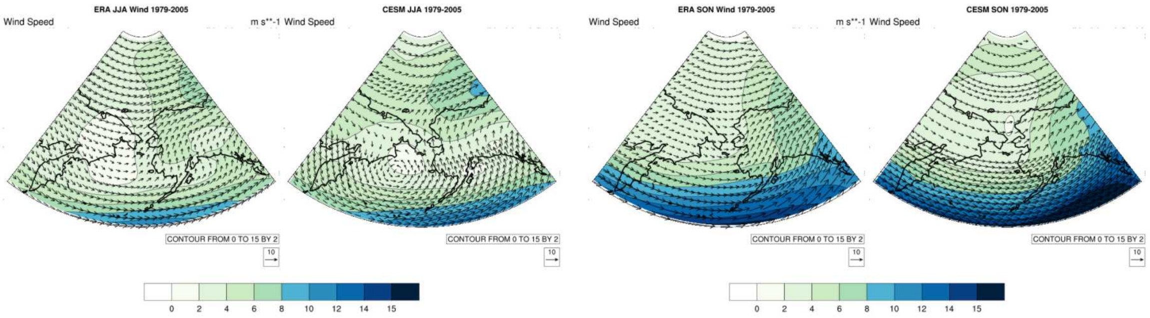

(c) Summer Wind Speed and Direction **(d)** Fall Wind Speed and Direction

Figure 2.10. Comparison of pattern of wind speeds and directions from CMIP5 CCSM4 (left) and ERA-I (right) over Oliktok (left) and Barrow (right) from 2000-2005.

Table 2.2. Seasonal's minimum, maximum, and standard deviation (between latitude and longitude locations) of the 500 mb wind speed (m s^{-1}) in the CCSM and ERA-I datasets.

Data Source	Season	Variable	Min.	Max.	Standard Deviation
CCSM	SON	Wind Speed (500mb)	1.161	15.2764	3.396433
ERA-I	SON	Wind Speed (500mb)	2.614834	24.22476	5.013885
CCSM	DJF	Wind Speed (500mb)	1.279716	11.86487	2.35033
ERA-I	DJF	Wind Speed (500mb)	0.0004978	16.77662	3.768197
CCSM	MAM	Wind Speed (500mb)	0.1830284	10.10167	1.879354
ERA-I	MAM	Wind Speed (500mb)	0.0891424	17.01571	3.300661
CCSM	JJA	Wind Speed (500mb)	0.0888757	11.02575	1.817671
ERA-I	JJA	Wind Speed (500mb)	0.0034591	17.72448	3.185138

but the ERA-I data suggests that Toolik has the least cloud liquid water content from around 850 hPa and below. Atqasuk and Barrow appear to have more liquid clouds than Oliktok and Toolik during winter. Spring and mean cloud liquid water content is lower in CESM historical CMIP5 simulations compared to ERA-Interim data. Mean cloud liquid water content between all sites is very similar during spring and deviates with height similarly. Variation in mean cloud liquid water content between sites is large during summer months. The average cloud ice content is lower in CCSM in all seasons, although summer ice cloud content at low levels (less than 900hPa) is not as low. ERA-Interim data show that Barrow has the most cloud ice water content near the surface and that Oliktok has the most cloud ice water content between 900 hPa and 650 hPa while from around 650 hPa to 200 hPa, Toolik has the most cloud ice water content. ERA-I data show much more deviation in the amount of cloud ice water content between sites than CESM data below 500 hPa. Compared to the state variables of temperature, humidity, and winds, the variability between the cloud liquids seasonally and in the datasets shows the nonlinear impact of the cloud microphysical parameterizations in CESM and ERA-I. Meaning, incremental increases in temperature and humidity do not appear to proportionally correlate to increases in liquid or ice cloud.

Figures 2.13, 2.14, and 2.15 show the annual cycle of total water (liquid and ice), cloud water, and cloud ice, respectively, from the CCSM4 simulations over Barrow and the ERA-I output over Oliktok. The two different sites were chosen for the two different data sets to provide a qualitative comparison between these variables. Notably, an annual cycle of cloud liquid and ice appears in the years 2000-2005 over these locations in these two datasets. Liquid dominates the lower levels, and ice dominates the upper levels of the atmosphere. The pattern of liquid and ice in these two datasets between Barrow and Oliktok leads to a hypothesis that these two locations are climatologically similar. It is also seen from the mean profiles that Oliktok and Barrow are climatologically similar in the CCSM and ERA-I datasets. From the profiles, the main differences between sites occur between Toolik and all other sites. Toolik is farther inland, where the weather is less regulated by the ocean. The trends between CCSM4 and ERA-Interim variables are generally the same, but less similar for cloud variables.

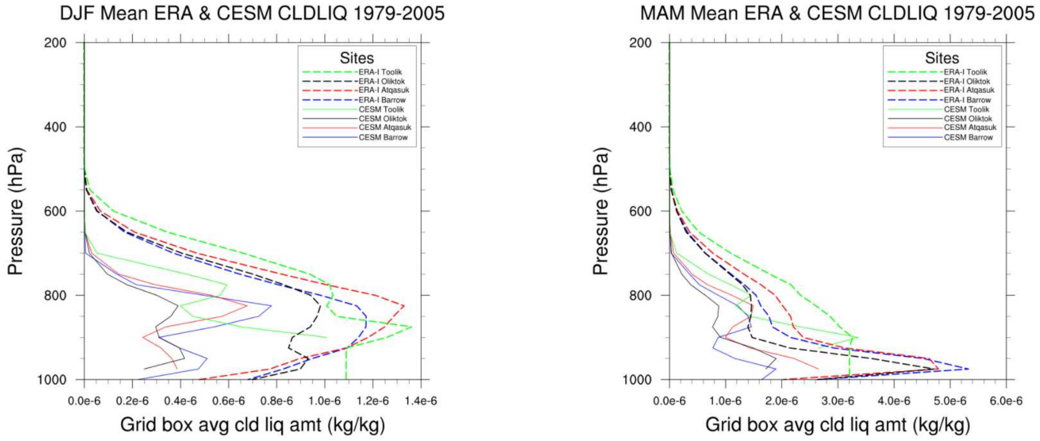

(a) Winter Cloud Liquid

(b) Spring Cloud Liquid

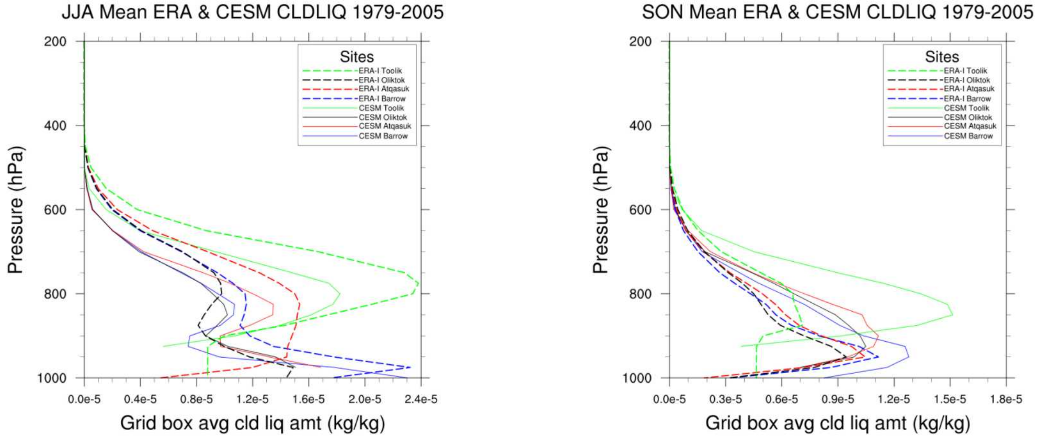

(c) Summer Cloud Liquid

(d) Fall Cloud Liquid

Figure 2.11. Comparison of cloud liquid water content in CMIP5 CCSM4 and ERA-I in seasonal means for Barrow, Oliktok, Atqasuk and Toolik.

To gain a comprehensive view of the differences between the datasets over the region, Figure 2.16 shows the cloud liquid climatologies by season and their differences from the CCSM and ERA-I datasets over the North Slope of Alaska region. The lack of cloud liquid water at 850 hPa in DJF and MAM between both CCSM4 and ERA-I is notable, while the reoccurrence of cloud

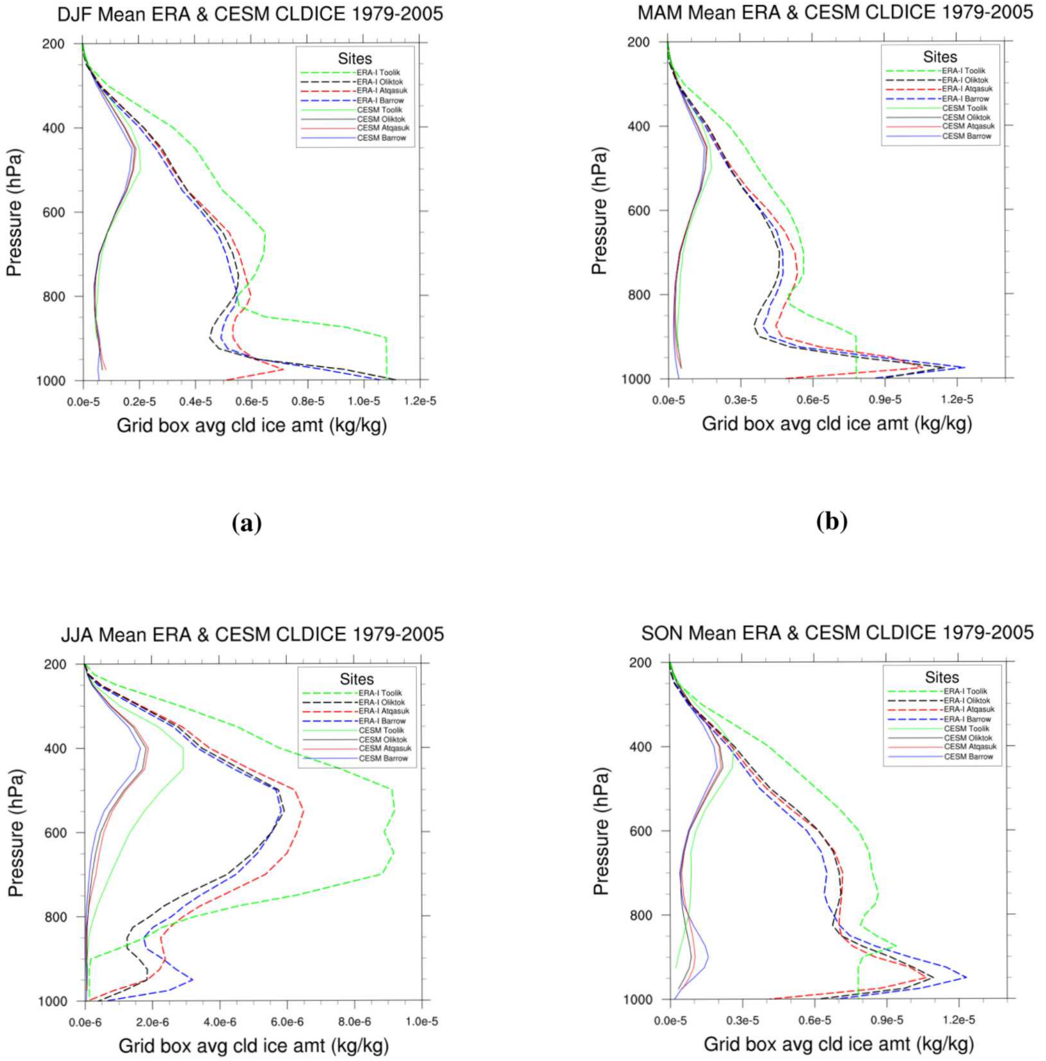

(a) (b)

(c) (d)

Figure 2.12. Comparison of cloud ice water content in CMIP5 CCSM4 and ERA-I in seasonal means for Barrow, Oliktok, Atqasuk and Toolik.

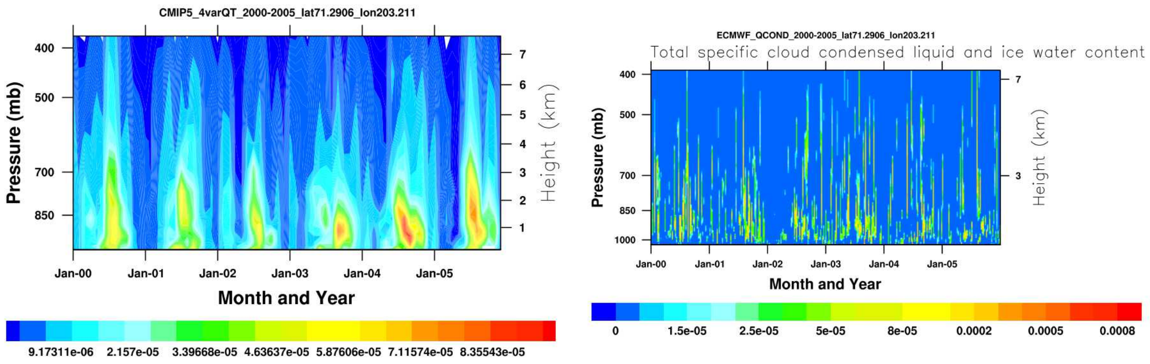

(a) Annual cycle of total cloud condensate from CCSM4 over Oliktok.

(b) Annual cycle of total cloud condensate from ERA-I over Barrow.

Figure 2.13. Qualitative pattern of total cloud condensate (liquid and ice) in from CMIP5 CCSM4 (left) and ERA-I (right) over Oliktok (left) and Barrow (right) from 2000-2005.

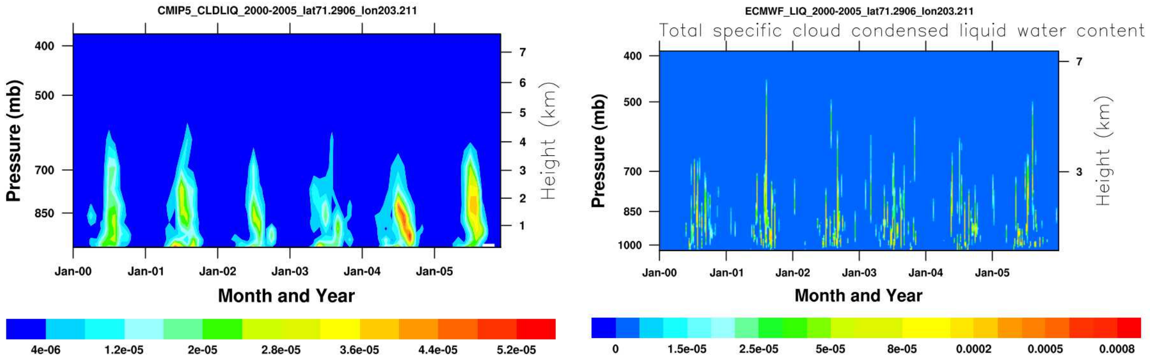

(a) Annual cycle of cloud liquid from CCSM4 over Oliktok.

(b) Annual cycle of cloud liquid from ERA-I over Barrow.

Figure 2.14. Grid box averaged cloud liquid amount (kg kg^{-1}) from CMIP5 CCSM4 (left) and ERA-I (right) over Oliktok (left) and over Barrow (right) from 2000-2005.

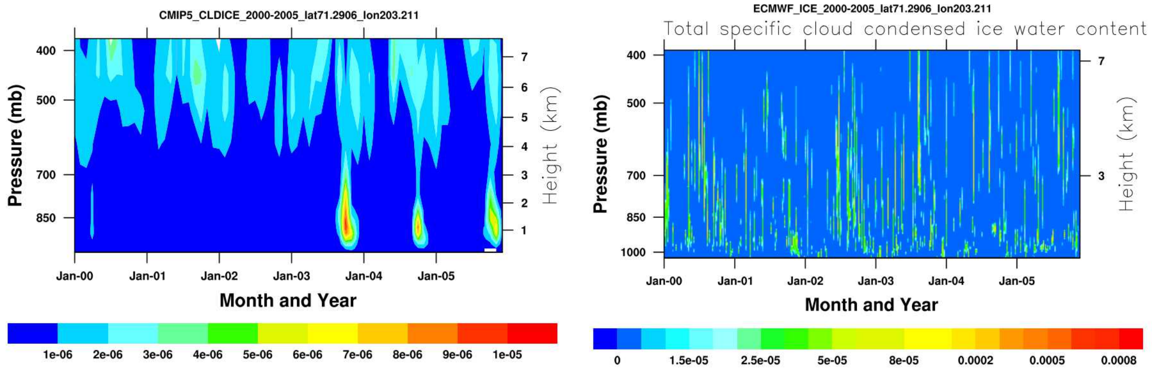

(a) Annual cycle of cloud ice amount from CCSM4 over Oliktok.

(b) Annual cycle of cloud ice amount from ERA-I over Barrow.

Figure 2.15. Grid box averaged cloud ice amount (kg kg^{-1}) from CMIP5 CCSM4 (left) and ERA-I (right) over Oliktok (left) and Barrow (right) from 2000-2005.

liquid water content in the warmer seasons of JJA and SON is also similar.

Cloud fraction is a qualitative variable and not much analysis should be placed on it. The variable should not be compared between different datasets. Plots of cloud fraction are shown here as qualitative aids in Figure 2.17 over the region and Figure 2.18 by height over Barrow. Interpreting CCSM4 output shows high variability in average cloud cover over the region, but less variability in cloud over over Barrow itself. The summer season, JJA, has the least amount of clouds by season according to CCSM4. Finally, Figure 2.19 gives a qualitative impression of the annual cycle of cloud cover from CCSM4 and ERA-I data over the period 2000-2005 over Barrow. Notice the peaks in cloud cover in the Fall months, then reduces in the winter.

As discussed in earlier text, ERA-I and CCSM4 have noted biases in Arctic climate. Grounding this bias agains observations is important for future development. The source of observations to which CCSM4 and ERA-I can be compared is from the ARM instrumentation which was used to created an estimated cloud liquid water path at Barrow. Figure 2.20 plots the annual mean and standard deviation between the three data sets at Barrow. The phase of the amplitude of the global datasets (CCSM4 and ERA-I) peak one-to-two months too early compared to the ARM observations, which peaks in September. Additionally, the global data sets are consistently low in cloud liquid water path by about 50%.

Bringing this back to how the cloud amount (or lack thereof) causes changes to surface heating (and thereby changing the amount of sea ice loss predicted and Arctic Amplification implications),

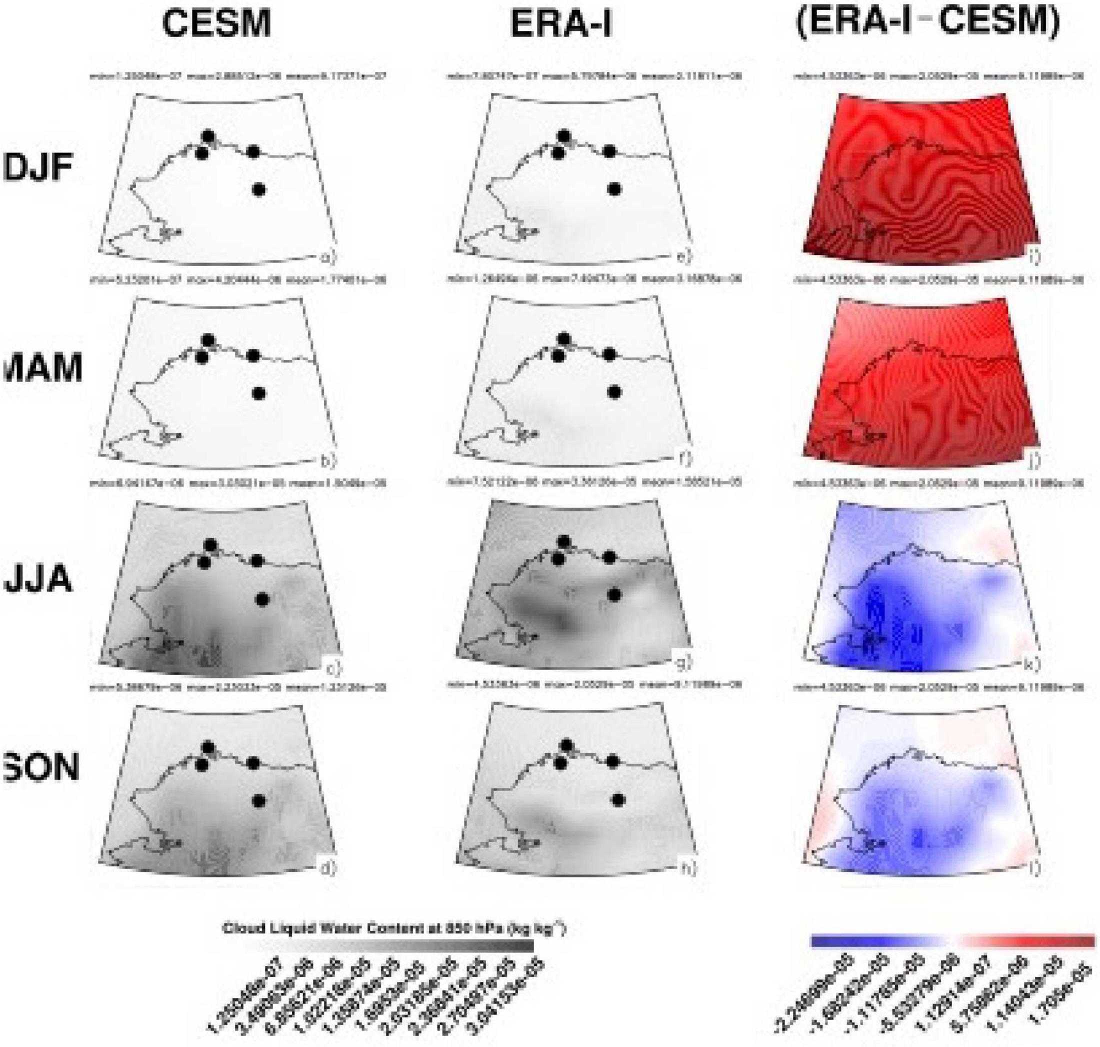

Figure 2.16. Cloud liquid water content at 850 hPA (kg kg^{-}1) from ERA-I, CESM, and the difference of the datasets from 1979-2005 over the North Slope of Alaska Region averaged into seasonal means. The minimum, maximum, and mean values are also given.

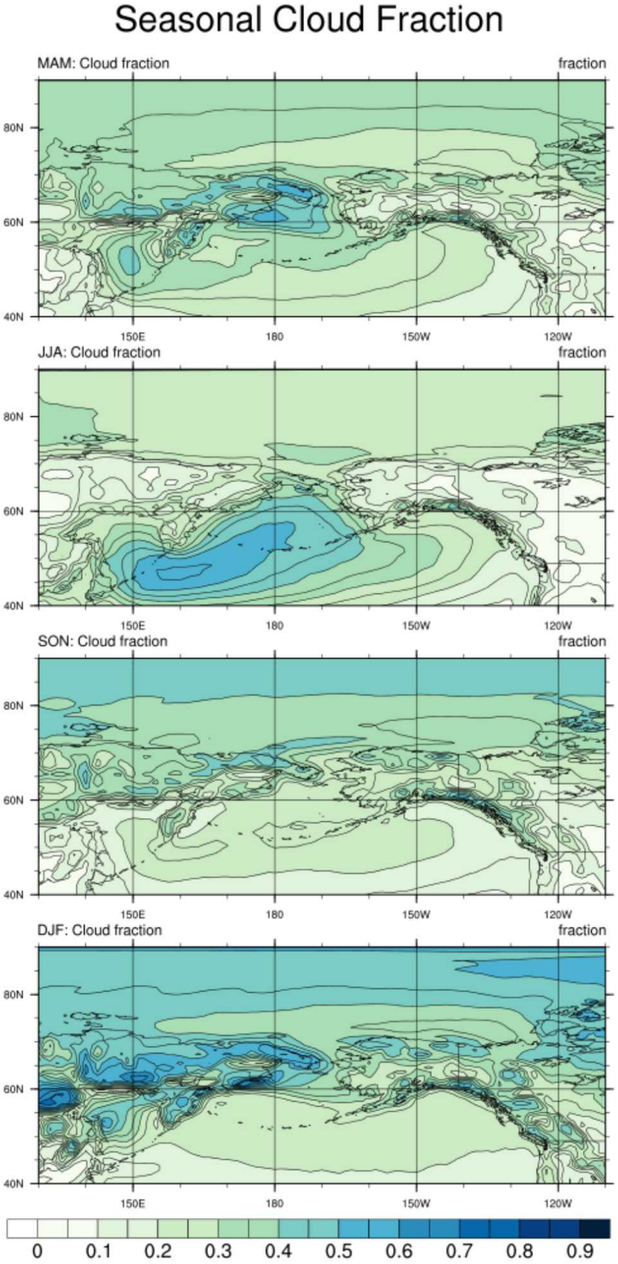

Figure 2.17. Average seasonal cloud fraction by season from the CCSM4 simulation output over the North Slope Region.

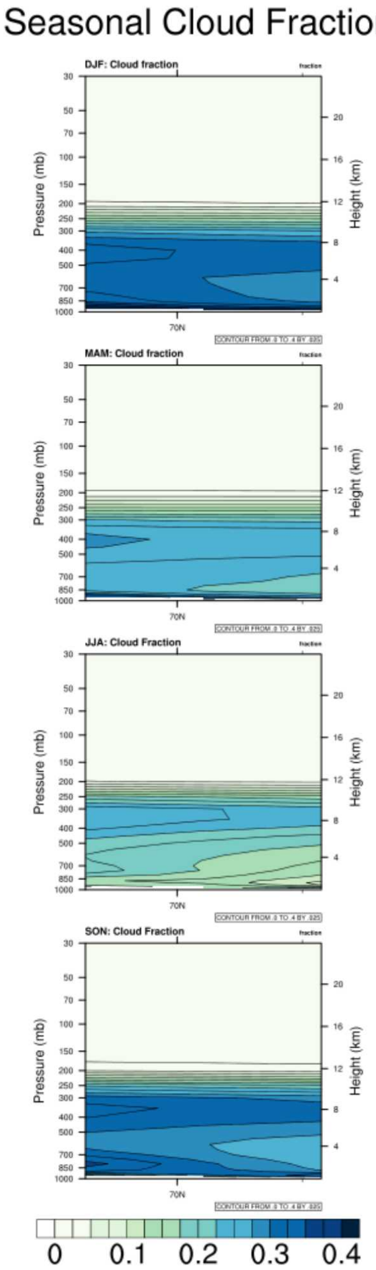

Figure 2.18. Average seasonal cloud fraction by season and height over Barrow.

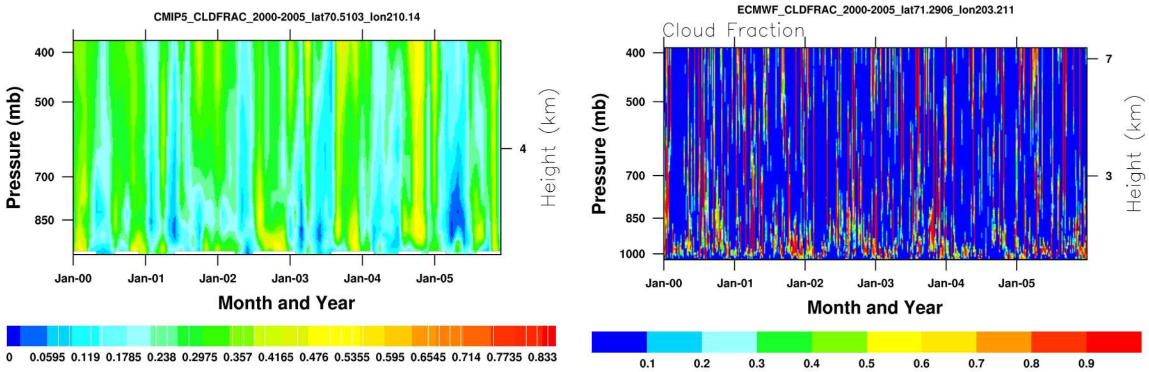

(a) Annual cycle of cloud fraction from CCSM4 over Oliktok.

(b) Annual cycle of cloud fraction from ERA-I Oliktok Barrow.

Figure 2.19. Qualitative pattern of cloud fraction from CMIP5 CCSM4 (left) and ERA-I (right) over Oliktok (left) and Barrow (right) from 2000-2005. Two different sites are plotted to avoid quantitative comparisons between these datasets with this variable.

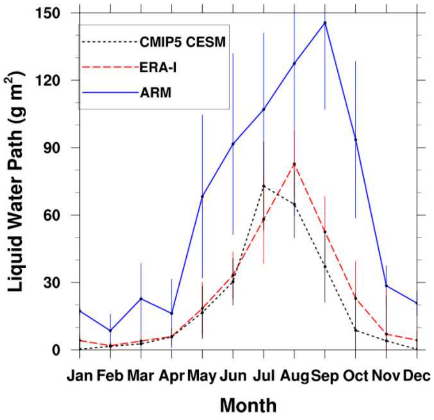

Figure 2.20. Monthly mean of cloud liquid water path at Barrow, Alaska, from ARM instrumentation creating a higher-order data product, the CMIP5 CCSM4 simulation dataset, and the ERA-I reanalysis data product. Error bars represent one standard deviation of the mean.

Figure 2.21 shows the downwelling longwave radiation as a function of liquid water path as measured at the NSA ARM site hourly from 2000-2005. The magnitude of the liquid water path is 5-6 times larger than expected. An absolute area of future work would be to also compare CCSM4 and ERA-I values to this dataset and using an expression to derive heating at the surface.

Suggested areas for follow-on work include creating a better reanalysis product. A study by Xie et al. (2006) examines observational data collected during the Mixed-Phase Arctic Cloud Experiment at the ARM facility at the North Slope of Alaska in comparison with ECMWF analysis. The experiment lasted from 5 thru 22 of October 2004. While the M-PACE sounding network is comprised of four sites (Utqiagvik, Oliktok, Atqasuk, and Toolik), the domain of the analysis was limited to a smaller area, replacing Toolik Lake with a lower elevation site. Instead of comparing ECMWF model output with point measurements from ARM, M-PACE data was processed using an objective variational analysis method developed by Zhang and Lin (1997). M-PACE observations were interpolated onto analysis grid points using an interpolation scheme described by Barnes (1964), and then means were calculated in this domain. It was found the new analysis derived for this period provided a better representation of large-scale systems that affected the NSA dynamically and thermodynamically and that ECMWF underestimated liquid water path in single-layer boundary clouds. Because downwelling longwave radiation is dependent upon liquid water path, the surface downwelling longwave radiation during the occurrence of single-layer boundary clouds was also largely underestimated (Xie et al., 2006). Because of the findings of Xie et al. (2006), similar hypothesis can be made regarding cloud bias in the CCSM4 CMIP5 historical simulation data and the ERA-Interim reanalysis data here.

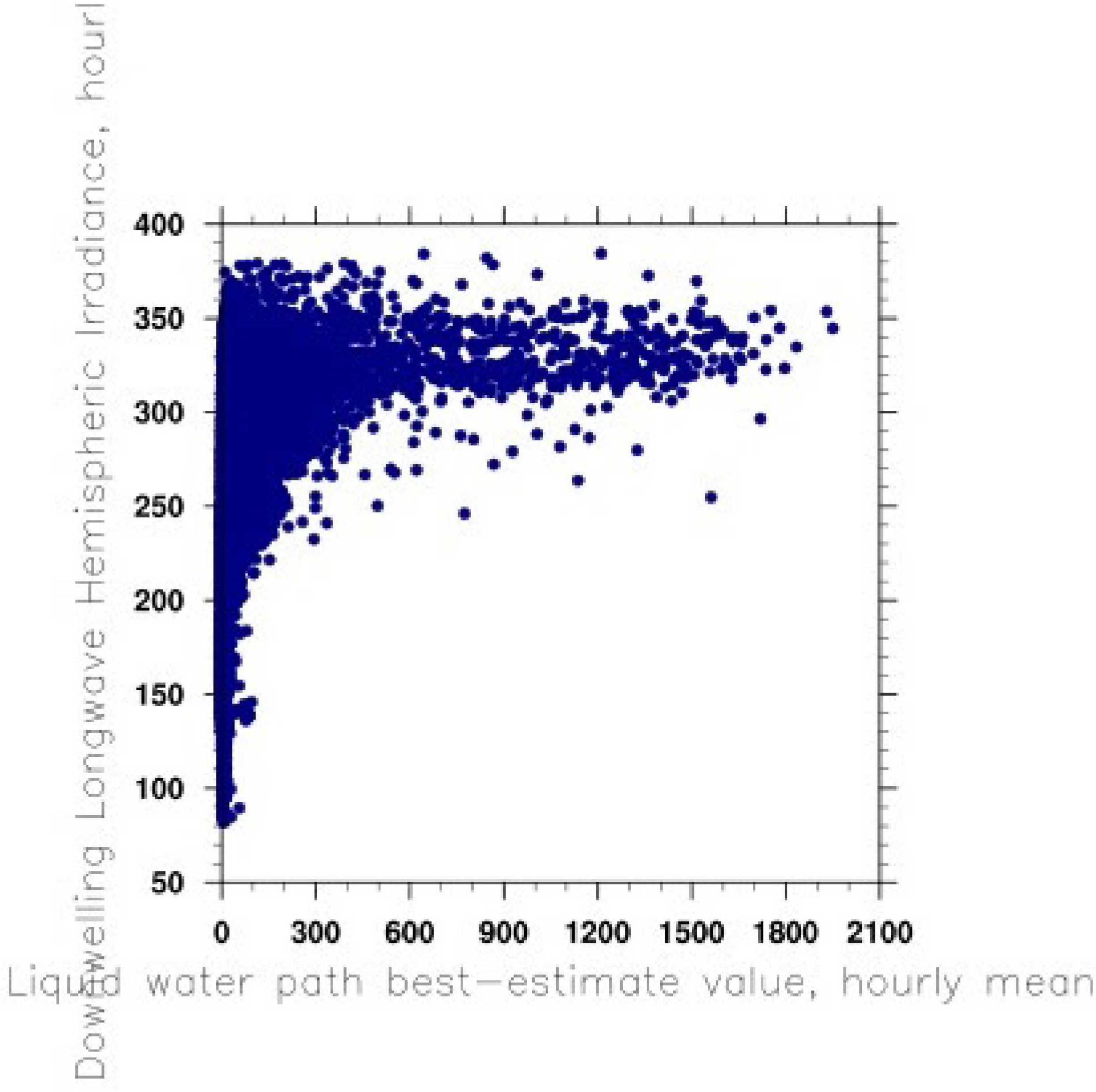

Figure 2.21. Hourly Longwave Downwelling Radiation (W m^{-2}) as a function of Liquid Water Path (g m^{-2}) from the North Slope of Alaska site at Barrow measured from 2000 - 2005.

An additional area for future work would be to include more observational data. The ARM dataset at Oliktok reliably begins in 2014, so it is suggested that two or more years of data would improve comparisons. A similar comparison could be made with Atqasuk, Barrow, and Oliktok when Atqasuk was operational (i.e., 2000-2010). Even though Barrow data collection has been occurring for 20+ years at time of this writing, higher-order data products such as liquid water path are only available for select years. Discretizing and identifying differences in observations, simulations, and global reanalysis for different levels of the atmosphere would be good future work as well as sea ice levels. We would wish to determine from decadal-long cloud data over the North Slope sites how the cloud liquid water path has been changing, how much heating the clouds have been exerting towards the surface.

2.2 Variable Resolution Grid Generation and Preliminary Analysis of Regional Refinement

Global climate models resolve and represent Earth System features with various degrees of fidelity. It is assumed that by increasing resolution of regional features in the climate model, the simulation would improve. Computational resources limit resolution, so globally increasing resolution is not possible. Because this project's goal is to explore ways to reduce model bias of the Arctic low cloud environment in global climate models through increasing resolution, the variable resolution configuration is useful to explore resolution and parameterization limitations without running the computationally expensive high-resolution global climate model. An investigation of the appropriate area and size of refinement is necessary to ensure that weather and climate processes which may affect the NSA site are captured and fully resolved before reaching the North Slope. Using different size patches of high resolution over the NSA could help understand where high resolution could improve the global climate model simulation and where it is not needed. Looking to the future, this analysis might also help inform an NSA megasite developed from a variable resolution AGCM with LES-scale resolution.

Three variable resolution atmospheric general circulation model (AGCM) grid configurations were developed as potential alternatives to stand-alone high-resolution regional models. SquadGen, NCL, and GIMP are used to create the grids. Options in SquadGen for smoothing distance {-1, 2, 3, 5}, smoothing iterations {15, 20, 30} for each grid were produced but not further analyzed as this also remains an area of future work. Grid generation workflow is documented elsewhere.[5] Each configuration is based on a global cubed-sphere grid with an effective resolution of 1 degree, with a refinement in resolution down to 1/8 degree over an area surrounding the ARM megasite. Figure 2.22 shows three prototype grids with about 8,000 (small), 9,000 (medium), and 14,000 (large) elements that could be used to study resolution in improving the climate simulation over NSA. Grids vary based upon the selection of areas of refinement which could capture different climate and weather processes. Optimal size and shape of the area of refinement for a variable resolution model at the NSA will be investigated with future simulations.

---

[5] `https://github.com/E3SM-Project/PreAndPostProcessingScripts`

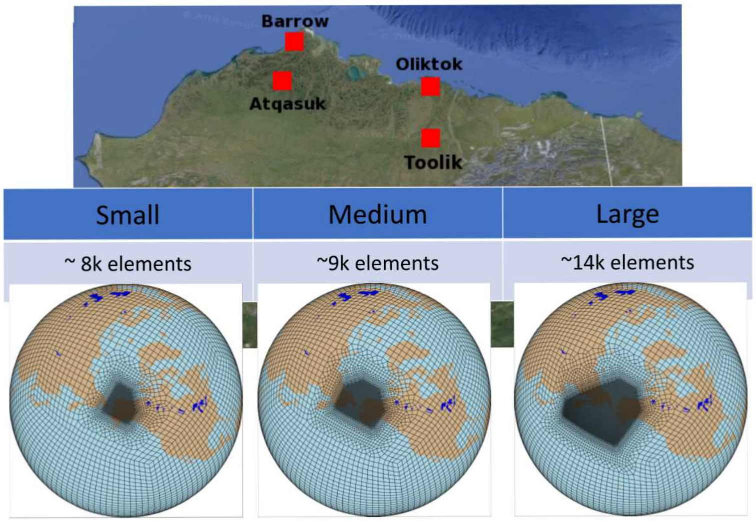

Figure 2.22. Four sites of interest and three prototype variable resolution grids that could be used to probe the climatology of the North Slope of Alaska with higher resolutions. The more elements the variable resolution grid has, the more computationally expensive the simulation is to run. There is motivation, therefore, to minimize the high resolution patch without loosing key features that would significantly affect the climatology of the area of interest.

The large mesh attempts to capture possible cyclogenesis off of the coast of Russia (Crawford and Serreze, 2014) and any other possible moisture transport which may occur in the Bering Sea or off of the Kamchatka Peninsula. The large mesh also captures the Aleutian Islands, which may be an important location of Rossby wave breaking (e.g., (Liu and Barnes, 2015)) and cyclogenesis Vavrus (2013)). The eastern border was drawn in order to capture all of Alaska and the Brooks Range, as well as any polar fronts which may enter the north slope from the east. The topmost boundary is drawn to include any possible cyclonic activity, fluctuations in sea ice, or moisture transport.

The medium mesh varies from the large mesh in that the southwestern side and northwestern sides are minimized to exclude some extent of Russian coasts and the Kamchatka Peninsula. A small part of the Aleutian Islands is included in order to resolve possible moisture transport from that area before it reaches the North Slope. Some Russian coasts are still included to capture possible cyclogenesis (Crawford and Serreze, 2014) and the Bering Strait is still highly refined in order to capture extreme extreme moisture transport (Liu and Barnes, 2015) as well as important fluctuations in sea ice (Carton et al., 2015).

The small mesh varies from the medium mesh in that it excludes more of the Russian coast, which excludes areas of possible cyclogenesis from refinement to test how much space is needed to refine storms before they reach the North Slope. It also excludes slightly more of the North Pacific and Bering Sea to test the distance at which moisture transport must be refined in order to accurately characterize it over the NSA. The entire state of Alaska is still captured in order to ensure the Arctic Frontal Zone is well characterized, since mountain ranges such as the Brooks Range enhance the AFZ by preventing cold air from moving inland as described in Reed and Kunkel (1960) and Serreze et al. (2001).

Some grid diagnostics were performed with the stand-alone dynamical core to gather diagnostic statistics about the elements within the grid. The smallest grid spacing gives an indication of the time step needed for the model run, with a larger grid spacing indicating a larger time step. It is also speculated that the smallest grid spacing may cause noise in the dynamical core if it is too small. Because the three grids will be compared, the same time step should be used for each grid configuration. In the interest of saving time, the larger time step equates to the faster simulation. The large grid had a smallest grid spacing value of 6.68, while the medium and small grids had a smallest grid spacing value of 7.43. These values are related to the eigenvalues of the Laplace operator (Guba et al., 2014). The largest grid with over 13,000 elements and having the smallest grid spacing is more computationally expensive, so effort was made to search for the smallest element(s) in the large grid. Because only the south and west edges were altered in order to create the small and medium grids, the smaller grid spacing in the large grid was most likely located on the south or west edges. Unfortunately, alterations to the shape of the large grid on the south and west edges (smoothing corners, adding elements, removing elements) did not alter the value of the smallest grid spacing from its original value of 6.68.

Because altering the edges of the area of refinement in the large grid did not increase the size of the smallest grid spacing, one other reason was investigated as to why the smallest grid spacing was a smaller value for the large grid than the medium and small grid. Because the edge of the area of refinement in the large grid was close to the edge of the cube face, one hypothesis was that the refinement transition area being close to the edge of the cube face was causing possible distortion. In order to minimize this distortion, three new grids were created on a cube-sphere grid which had been rotated in the negative y-direction by 45 degrees in SquadGen to center a cube face over the area of refinement. Again, the new grids did not have a larger value for the smallest grid spacing, and in fact, had a smaller value of the smallest grid spacing of 6.32. Because rotating the cube faces did not improve the size of the smallest grid spacing, the original grids were used for testing instead of the rotated grids.

The smallest grid spacing of 6.68 in the large grid will not likely cause a problem as another RRM grid named sooberingoax4x8v1 (described in Appendix B) ran without issue for six simulated years. Noise caused by distorted grid elements has improved in the last decade because of the inclusion of hyperviscosity. Guba et al. (2014) has more information regarding variable resolution grid sensitivity and resolution-aware numerical viscosity.

The future work of these grids would be to finish creating all of the necessary input files to be run in an AGCM like the Energy Exascale Earth System Model (E3SM). Output will be compared with simulation and reanalysis data, and a comparison will also be made between output from grids with different sized areas of refinement. After this analysis is performed, it will be determined which processes must be captured in the area of refinement to minimize low cloud model bias in the Arctic, and the optimal size grid would be selected. The small grid would provide an advantage in its reduced computational time if it can accurately capture all of the climate and weather processes important in characterizing the north slope. However, if the area of refinement is not large enough and NSA is not accurately characterized, the medium or large grids may be preferred.

The sooberingoax4x8v1 grid was studied for resolution effects on cloud properties even though its original purpose was to study Arctic Extremes. This grid and the simulations are described in Appendix B and shown in Figure B.1. Figure 2.23 shows the annually-averaged cloud liquid amount over the North Pacific refined area, and Figure 2.24 shows the annually-averaged cloud ice amount. These profiles of cloud liquid and ice generally increase with resolution, supporting the original hypothesis of this work. If the SP-CAM configuration could be considered the highest resolutions (even though later study revealed it to be better classified as a different model entirely with a different parameterization), the cloud liquid is the highest in this configuration. The cloud ice profile has opaque meaning with the SP-CAM average significantly decreasing in magnitude at about 800 hPa. If increased liquid water path is due to increased magnitudes of vertical velocities, then Figure 2.25 plots the PDF of the subgrid vertical velocity. Variable resolution has the most frequent and highest values of vertical velocity, and also at lower elevations.

Although variable resolution was not analyzed to the extent initially proposed in this project, valuable insight was gained in analyzing the profiles of cloud liquid and ice. Also, extreme systems, such as extratropical cyclones and Arctic storms were analyzed given in Appendix B. As with increasing cloud amount with resolution, increasing model resolution increases the number of storms.

Comparing these different model configurations to each other and to reanalysis is time and computationally-resource intensive as the simulations need to be integrated for long durations to produce statistically-significant seasonal averages from multi-year simulation data sets. A

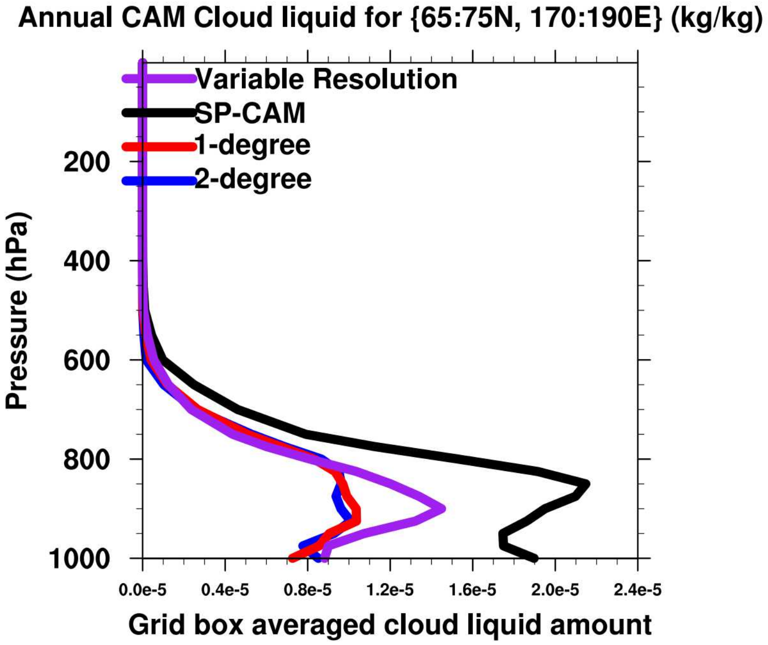

Figure 2.23. Annual average cloud liquid amount as a function of model height for four different resolutions: Variable resolutions (sooberingoa grid), SP-CAM, uniform 1-degree, and uniform 2-degree. The SP- configuration is labeled as a resolution, even though later study revealed it to be better classified as a different model entirely with a different parameterization.

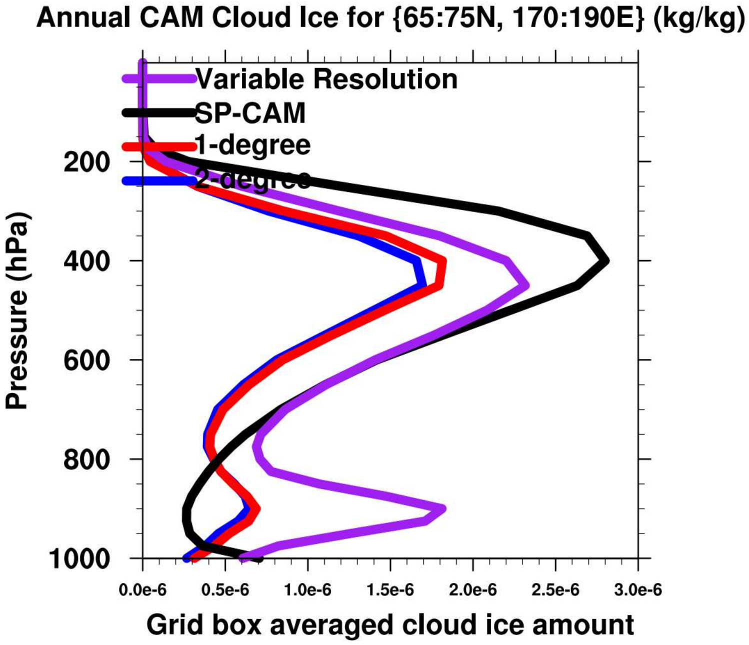

Figure 2.24. Annual average cloud ice amount as a function of model height for four different resolutions: Variable resolutions (sooberingoa grid), SP-CAM, uniform 1-degree, and uniform 2-degree. The SP- configuration is labeled as a resolution, even though later study revealed it to be better classified as a different model entirely with a different parameterization.

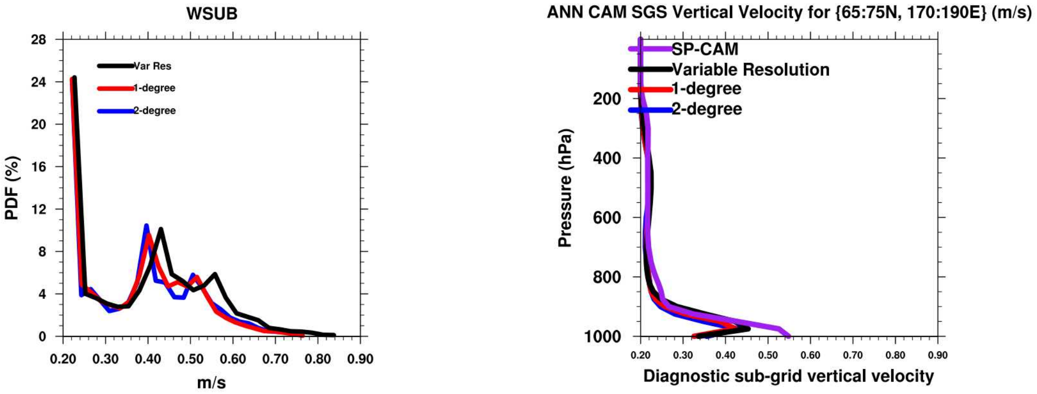

(a) PDF of subgrid vertical velocity.

(b) Annual average of subgrid vertical velocity.

Figure 2.25. The pdf of the annual average subgrid vertical velocity amount (left) and the annual average subgrid vertical velocity amount as a function of model height (right) for four different resolutions: Variable resolutions (sooberingoa grid), SP-CAM, uniform 1-degree, and uniform 2-degree. The SP- configuration is labeled as a resolution, even though later study revealed it to be better classified as a different model entirely with a different parameterization.

computationally-cheaper method of running a full AGCM in any configuration is to constrain the dynamics by nudging the winds, temperature, and moisture variables to reanalysis thereby allowing analysis to be performed over a specific time interval where model biases are shown to be problematic. This nudging effort was performed with reanalysis downloaded, scripts generated for simulation, and some data analysis produced. Figure 2.26 shows an example of the beginnings of this work, where nudged and unnudged wind fields are compared at two different isobaric heights: 200 hPa and 850 hPa. The nudging simulations were envisioned to be performed during the same times as the Tethered Balloon System (TBS) operations described in the Chapter 3. Unfortunately, time and resources were not available to complete this analysis and remains an area of future work.

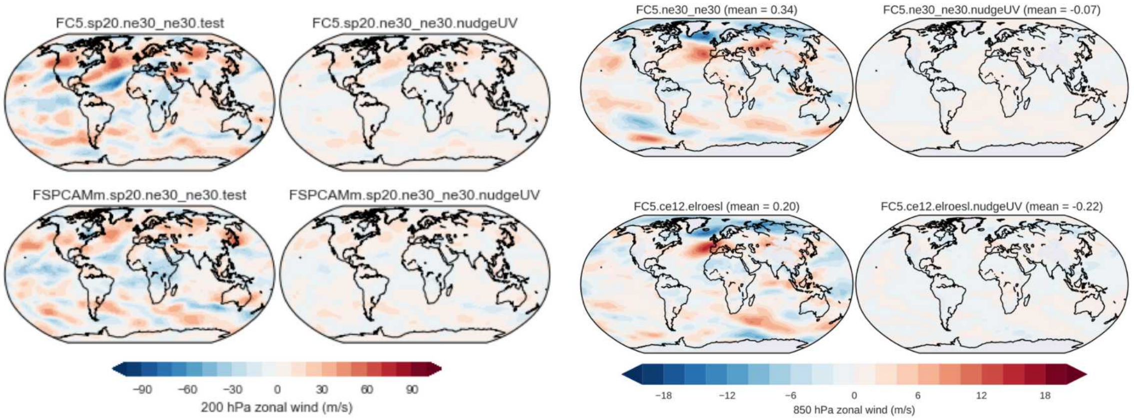

(a) 200 hPa zonal wind flow for nudged and unnudged wind fields.

(b) 850 hPa zonal wind flow for nudged and unnudged wind fields

Figure 2.26. Comparisons of 200 hPa and 850 hPa zonal wind fields for nudging and not nudging the UV wind fields in the CAM model to reanalysis.

Chapter 3

Surface-Based Atmospheric Measurements in the Arctic

In situ cloud measurements for this project were taken at Oliktok Point, Alaska (Figure 3.1). Oliktok Point is located near Deadhorse, Alaska, on the coast of the Beaufort Sea. The Department of Energy's (DOE) Office of Science Biological and Environmental Research (BER) Atmospheric Radiation Measurement (ARM) program operates one of three ARM Mobile Facilities (AMF-3) at Oliktok Point since 2013. The proximity of Deadhorse to Oliktok Point and AMF-3 in North America are shown in Figure 3.2. An unique feature of AMF-3 is the Restricted Airspace, which is managed by Sandia National Laboratories and permits the use of Unmanned Aerial Systems (UAS) such as the Tethered Balloon System (TBS). The footprint of the Restricted Airspace is also shown in Figure 3.2. This restricted airspace, named R-2204, is a necessary capability tool for this project in measuring *in situ* cloud properties. The ability to use small UAS for longer periods of time without interrupting or restricting other air traffic is critical for acquiring the data sets needed for comparison with time-integrated atmospheric models for climate research.

Figure 3.1. Panoramic image of Oliktok point. The AMF3 blue containers are on the right in this picture, and the DEW line is in the distance adjacent to the beach.

To use the facility at AMF-3, a proposal for a small field campaign was submitted to the ARM program office. The Intensive Operation Program (IOP) named Aerial Assessment of Liquid in Clouds at Oliktok (AALCO), was accepted for use between October 2016 and October 2017. Permission for extension was granted, and further campaigns were performed through 2018. A safety review through Sandia National Laboratories was made and approved by the range safety

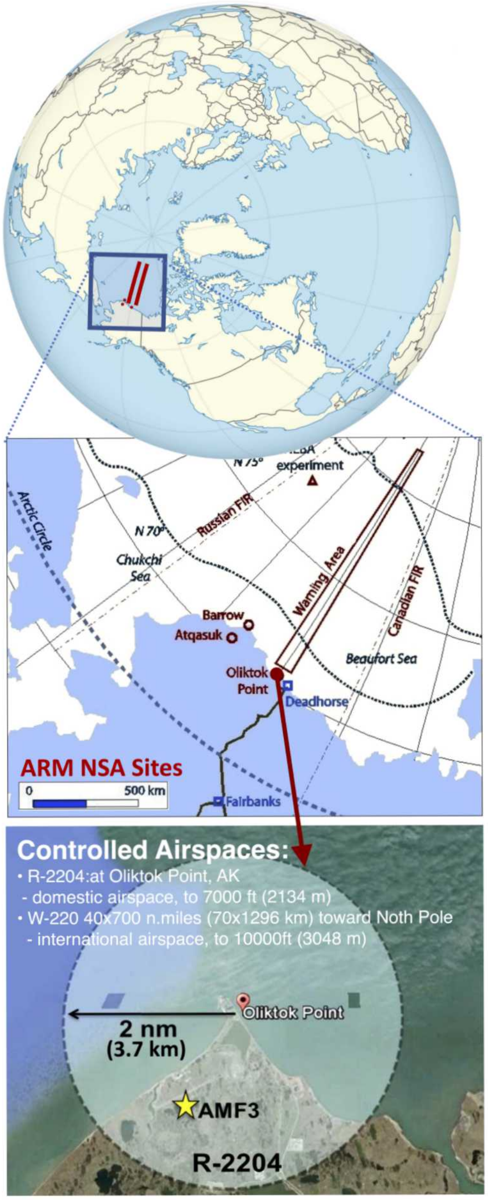

Figure 3.2. (Top to bottom) Location of the AMF3 ARM NSA site at Oliktok Point. The footprints of the airspaces are shown on the globe, from Oliktok, and at Oliktok.

officer, site manager, and line manager stating the field campaign followed the aviation activities for the 16 m^3 helikite and 34 m^3 aerostat Balloon Operations Aviation Safety Plan (AV15-13), so a separate Aviation Safety Plan was not required. Permission was granted to conduct aviation activities with other TBS and UAS operations with emphasis placed on having no conflict between activities. “Plan of the Day” meetings were held and reviewed by all operators.

The operations for AALCO included an aerostat on a winch trailer, a helikite on a winch trailer, and a smaller weather-type balloon on an auto-reeler system (Figure 3.3). All three aerial systems carried a super-cooled liquid water content sensor, a leaf-wetness sensor, a distributed temperature sensor, an InterMet (iMet) data logger, and various other equipment for other IOPs such as ”Evaluation of Routine Atmospheric Sounding Measurements using Unmanned Systems” (ERASMUS) and ”Inaugural Campaigns for ARM Research using Unmanned Systems” (ICARUS) at different times throughout the campaign. All data was transmitted and collected at the ground on a computer using NOAA’s open-source Sky Sonde software in a vehicle (for example, as shown in Figure 3.4). All data was collected on a laptop owned by Sandia National Laboratories. It was processed for quality assurance and control before being released to the ARM Data Repository. More information and how to download the data is given on ARM website’s field campaign summary [1] and in the final report (Roesler et al., 2018).

In this chapter, the major instrumentation is first described in Section 3.1. An overview of the campaigns is then given in Section 3.2 followed by preliminary analysis of the sensors used in this project in Section 3.3.

3.1 Instrumentation Overview

This section describes most of the major instrumentation used during field campaigns at Oliktok Point. Further information can be found in the ARM TBS Instrument Handbook (Dexheimer, 2018).

3.1.1 Aerostat and Helikites

An aerostat Model #26, 9 mil single ply, polyurethane (20.5 foot diameter by 13.3 foot height and 2919 cubic feet helium-filled) balloon has 116 pounds net lift at sea level in calm winds from SkyDoc was purchased in June, 2016 for about $12K. The reason behind this purchase was that weather balloons are not aerodynamically stable, tending to wobble a lot. The aerostat can stabilize the sensors by having enough lift from the volume of helium and tension from the tether to be more stable in boundary layer heights. The balloon can be rigged to the apex carabiner and inspected to ensure correct angle of attack during flight and correct attachment to carabiner. Additionally, the SkyDoc 80 m^3 and 100 m^3 balloons use skirts to maintain orientation and stability in flight. Aerostats are generally used when the desired maximum flight altitude is between 700 m to 1.5 km

---

[1] `https://www.arm.gov/research/campaigns/amf2016aalco`

Figure 3.3. Image of (left to right) helikite, Weather Balloon, aerostat all inflated in the hanger at Oliktok point.

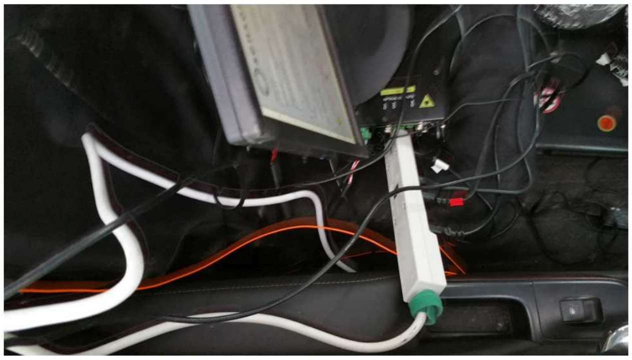

Figure 3.4. Power to the electronics used as data collection points from the instrumentation on the TBS.

Figure 3.5. Image of SLWC and tethersonde below balloon, October 2016.

AGL, the payload is between 10 to 25 kg, and surface wind speeds less than 6 m s^{-1}. It takes up to sixteen bottles of gas to fill these balloons.

Allsops 34 m^3 helikites are a balloon/kite hybrid that use lighter-than-air principles to obtain initial lift, and then a kite to achieve stability and dynamic lift. Helikites are typically used for flights with a desired maximum altitude below 700 m AGL, a maximum payload of less than 9 kg, and in surface wind speeds less than 10 m s^{-1}.

3.1.2 Leaf Wetness Sensor

Leaf Wetness Sensors (LWS) from Campbell Scientific [2] were purchased to be used as a depositional surface to measure supercooled liquid water content during the TBS deployments (Figure 3.6). Problems with communications prevented use during some of the early campaigns. The original LWS RF transmitter used in Fall, 2015 used a radio that accepted the communication. However, two new units had new radios, and they would not transmit to the base station. No data could be collected over the RF link. Customer support (Jacob Davis) reported finding the problem in the operating system, which need to reload on the whole system. The units were fixed and returned. The LWSs transmit on 902 - 928 MHz spread spectrum. The transmit power is less than 1 W. Once in consistent operation, it was then found that a lack-of resolution and overloading on the surface with ice rendered them not useful for analysis and comparison with simulations for the remainder of the campaigns. Each wetness sensor was about $700.

---

[2] `https://www.campbellsci.com/lws`

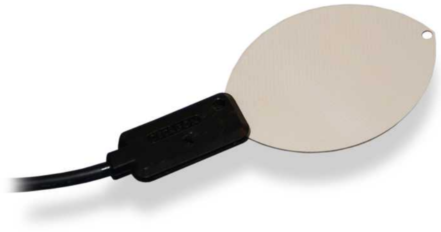

Figure 3.6. Image of Leaf Wetness Sensor from Campbell Scientific.

3.1.3 Supercooled Liquid Water Sensor

Supercooled liquid water measurements within clouds have been collected for several decades using other platforms such as manned aircraft (e.g., Gultepe and Isaac (1997)). Collection of supercooled liquid water in the Arctic is new where operational concerns and the frequent occurrence of these clouds within 2 km of the surface present additional challenges. Vibrating wire-based devices for measuring supercooled liquid water have been in development since the 1980s (e.g., Hill (1994)). In the past decade, vibrating wire-based supercooled liquid water content (SLWC) sonde flights have been conducted using radiosonde balloons concurrently with a collocated microwave radiometer, ceilometer, and Ka-band radar to validate the sonde-measured vertical profile of supercooled liquid water (e.g., King et al. (2016); Serke et al. (2014)). Advancing this approach, supercooled liquid water content sondes were operated on the ARM TBS at multiple altitudes within Arctic clouds simultaneously for several hours, in order to collect comparatively higher spatially and temporally-resolved data than were available from radiosonde balloon flights.

Anasphere's Supercooled Liquid Water Content (SLWC) sensor [3] (Figure 3.7) was used most frequently on the tethered balloon system. Each SLWC sensor was about $300, and about 10 were purchased over the duration of the project. The SLWC sensor collects a measurement of supercooled water by providing a surface on which supercooled liquid water droplets can freeze. The surface is a vibrating wire, and as more ice mass accumulates on the vibrating wire, the vibrational frequency of the vibrational wire changes. The rate of change of frequency is then used to calculate the supercooled liquid water content in the cloud. As explained by the manufacturer, higher airspeeds will cause faster changes in frequency, and assumptions regarding the airspeed and median droplet size are needed to calculate the supercooled liquid water content.

This sensor was intended to be used on sounding balloons and not for more than 30 minutes at time (Bolgnar, 2015). Its application here (i.e., used for an extended period of time at a more stationary height) is a new technology application and required research and design to prove the method. When used longer than intended, it was believed uncertainty would be introduced in the measurement due to drift from the wire vibrating. King et al. (2016) quantified the observed drift in an icing wind tunnel and then developed a method to correct for the drift in the data. When used in the field for this project, it was found the wires shed the ice quickly upon exiting the cloud

---

[3] `http://www.anasphere.com/slwc.php`

or reaching maximum ice loading. This was seen and documented in the timeseries datastream (Figure 3.11(e)).

Much lab and field testing and calibration had to be performed prior to using the sensors on the TBS at Oliktok as some of the vibrating wires were damaged during shipment and needed replacement. It was found that the lab-tested noise range of the SLWC sensors is about 0.03 g m^{-3}. On the TBS in the field, there were many issues with Electromagnetic Interference (EMI). For example in May, 2017, EMI occurred and the signal from the SLWC got dropped. The time series became contaminated, and it was uncertain if the wire had shed much ice or another natural process occurred. Work-arounds from this experience included 3D-printed InterMet enclosures with radio-frequency (RF)-reducing matting. An example of how they were attached to the tether with the 3D-printed InterMet enclosures with radio-frequency (RF)-reducing matting is shown in Figure 3.5.

In all, the SLWCs were deployed over 30 times in a three-year period. Details are given in Table 3.2.

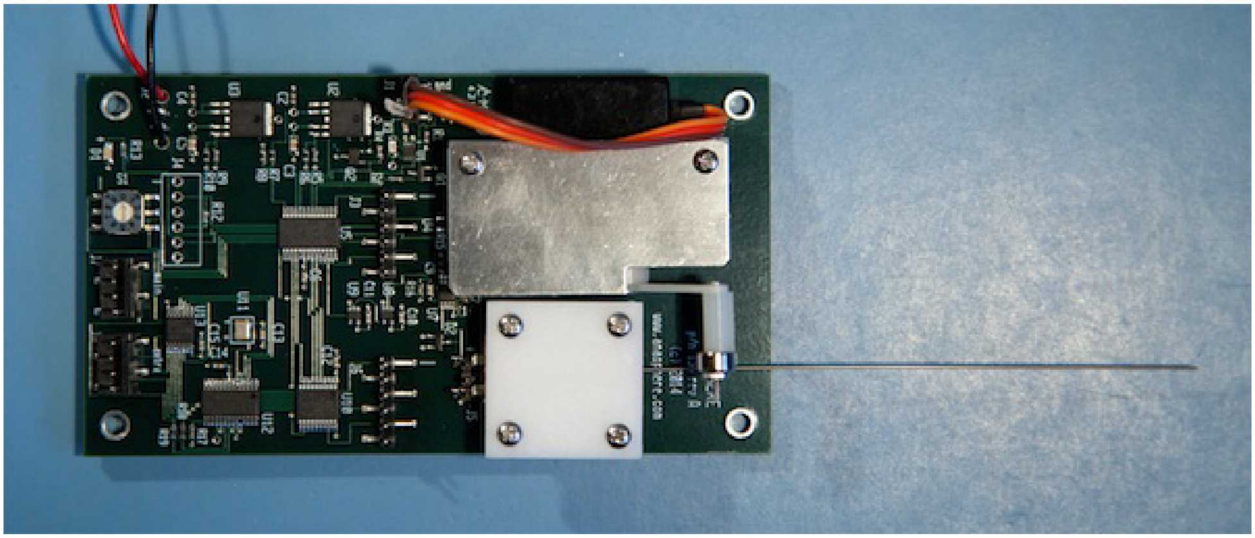

Figure 3.7. Image of Supercooled Liquid Water Content sensor from Anasphere.

3.1.4 Distributed Temperature Sensor

Distributed temperature sensing has been shown to be an effective method of collecting atmospheric temperature measurements (e.g., de Jong et al. (2015); Keller et al. (2011); Thomas et al. (2012)), but has been limited in the duration, altitude, and ambient conditions of measurement. The Distributed Temperature Sensor (DTS) Optical Fiber System system was made at the end of the first year of the project through October 2017. A decision was made to purchase a DTS manufactured by Sensornet, Didsbury Engineering Company LTD in Cheshire, United Kingdom for about \$44K. The DTS has the ability to take measurements of atmospheric temperature up to 1.5 km above ground level (AGL) every 30 seconds and at 1 m sampling resolution intervals with $\leq$ .08°C accuracy and is capable of operating outdoors in temperatures as low as -40 °C. The system was shipped with all required software and a 120 VAC to 12 or 24 VDC converter.

The Sensornet Oryx DTS fires a center wavelength 971 nm laser pulse lasting less than 10 nanoseconds through the attached optical fiber. Up to four fibers may be deployed from the DTS simultaneously. When the balloon is stationary, DTS data may be collected by directly connecting the optical fiber to the DTS system. However, there are some negative aspects of this configuration for the TBS. For example, at least twenty minutes are required to install and remove coils of fiber in calibration baths. Additionally, there is a potential risk of damage to the fiber whenever it is coiled or uncoiled as the TBS is sometimes required to float at a fixed altitude and sometimes required to do vertical profiling. To avoid these constraints, DTS data may be collected when the balloon is in motion by using a fiber optic rotary joint (FORJ) between the optical fiber and DTS. However, the low loss (< 0.5 dB) required for DTS measurements approaches the limits of most currently-available commercial FORJs. Multiple FORJs were tested before successfully collecting DTS measurements through an FORJ by using a fiber optic reel operated with a variable-speed electric motor. The fiber optic reel was spooled and unspooled using foot pedals to match the rate of the TBS winch during ascent and descent (Figure 3.8). It was then found that a method of demarcating the surface as the fiber spooled and unspooled was required.

A heat tray was initially used at the surface to warm a few meters of the fiber, but it warmed the fiber to the extent that the resulting measurements were offset. A glycol bath was tried in May 2017 and found to be generally effective but untidy, and finally a saltwater bath proved to be the most ideal solution. Single-ended DTS measurements were collected after initially attempting double-ended measurements, due to the reduction in datafile size and processing effort related to correlating the deployed fiber length with the balloon altitude, as it is affected by horizontal drag. Approximately 15 m of fiber were coiled into ice water and warm water calibration baths, with 15 m of fiber between each bath. A PT100 temperature sensor was placed in each bath and logged by the DTS. An iMet-1-RSB radiosonde measuring temperature every one second was placed at the balloon-end of the fiber to serve as an independent temperature measurement aloft for calibration. Figure 3.8 shows the set-up of the DTS, its bath, and the TBS system in Oliktok.

In September 2017, a second DTS system, a Silixa XT, was procured. The Silixa XT has a center wavelength of 1064 nm and is capable of 25 cm spatial resolution, largely due to a reduction in pulse duration to 2.5 nanoseconds, which allowed a smaller section of fiber to be used in the surface demarcation portion.

3.1.5 Additional Equipment

To reference some of the additional equipment needed for the field campaigns, such as the radio, antennae, and its accessories. The radio and accessories were products of iCom [4] and are used

---

[4] `www.ICOMAMERICA.com`

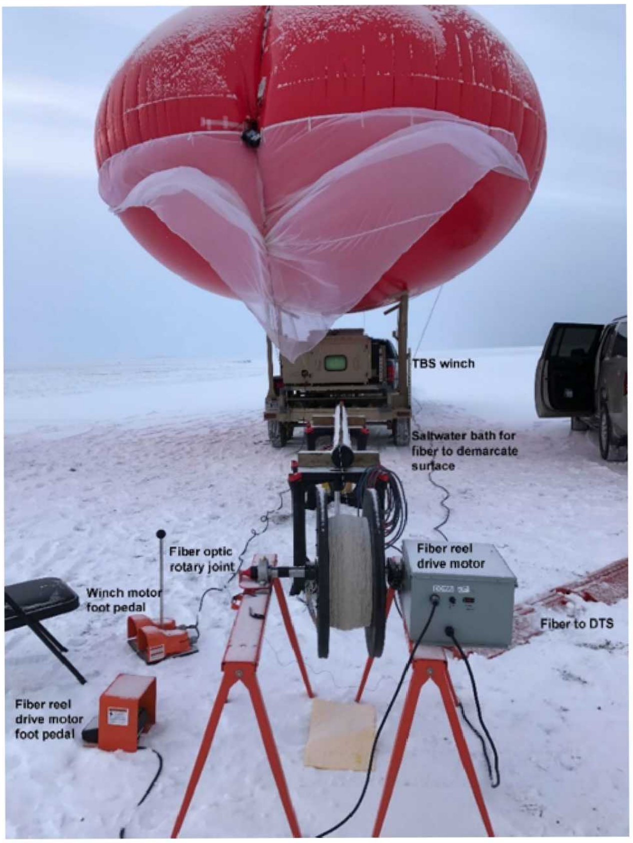

Figure 3.8. Image of TBS with optical fiber operating through rotary joint and saltwater bath.

to remotely retrieve information from the sondes. This is an inexpensive RF ground station that can be used within a vehicle on the runway at the ARM AMF3 site. Cigarette lighter cables were needed for power as the data acquisition stations were in a vehicle, USB audio adapters, and stereo cables were some of the other accessories. Lithium-ion batteries were used. Hard hats, provided by ARM, were worn for all operations. Helium to fill the balloons was purchased and shipped to Oliktok. Six cylinders was about \$400, and one balloon fill was about \$1200. In the early planning stages of this project, air core samples were considered for use. This required a Picarro, Aerodyne, or CALIOPI for analysis, which were deemed out of budget and focus. Ice crystal imaging instrumentation such as the Form Var Replicator was also considered but the VIPS (Video Ice Particle Sensor) instrument was used instead by another PI (Carl Schmidt) under support of the ARM program. The TBS may be driven by a 2 HP DC motor and speed reducer, a hydraulic winch that uses a gasoline-powered hydraulic pump, or smaller electrical winches depending on the mission and balloon in use. The most commonly used winch deploys over 2 km of Plasma® 12 strand synthetic rope with a published minimum breaking strength of 2.5 MT.

3.2 Overview of Tethered-Balloon Deployments

Table 3.2 lists all the TBS deployments associated with AALCO with sensors flown on helikites, weather balloons, or the aerostat. Over 100 hours of flight time was completed in daylight conditions to altitudes of 1.45 km AGL and with durations from one to nine hours in various atmospheric conditions including clear sky, broken to overcast clouds, rain, sleet, snow, and temperatures from -20° C to 25° C.

Figure 3.9. Torn helikite skirt, October 2016.

Table 3.1. AALCO Field Campaign dates with maximum altitude of TBS, SLWC and/or DTS operations

AALCO Field Notes and Simulations Performed			
Month, Year	Dates	Altitude (max kilometers)	Instruments
October, 2015	26	0.250	SLWC
	27	0.205	SLWC
	28	0.250	SLWC
April, 2016	18	0.213	SLWC
	19	0.027	SLWC
May, 2016	14	0.832	DTS, SLWC
	15	0.677	DTS, SLWC
	16		DTS, SLWC
June, 2016	6	0.500	DTS, SLWC
	7		DTS, SLWC
	10	0.680	DTS, SLWC
	11		DTS, SLWC
July, 2016	26	1.702	SLWC
	27	0.433	SLWC
October, 2016	15	0.639	DTS, SLWC
	17	0.760	DTS, SLWC
	19		DTS, SLWC
	20	0.669	DTS, SLWC
November, 2016	15	0.201	SLWC
	16	0.332	SLWC
	17	0.635	SLWC
April, 2017	3	0.188	SLWC
May, 2017	15	0.708	SLWC
	16	0.295	SLWC
	18	0.382	DTS, SLWC
	20	0.849	SLWC
	21	0.451	SLWC
	23	0.625	DTS, SLWC
	24	0.793	SLWC
August, 2017	6	0.295	SLWC
October, 2017	13	0.682	SLWC
	15	1.003	SLWC, DTS
	17		SLWC, DTS
	22	0.284	SLWC
May, 2018	14	0.200	SLWC
	15	0.210	SLWC
	17	0.650	SLCW, DTS

(a) Tethered balloon in a cloud. Picture taken in October 2016 from winch trailer on the runway with AMF3 shelters in the distance.

(b) Tethered helikite balloon in a cloud and sky conditions at 23:06 GMT taken on 13 October 2017. Solid precipitation was observed this day with notable clear and cloudy patches of sky.

Figure 3.10. Tethered balloons in clouds in (a) October 2016 and (b) October 2017.

(a) POPS and iMet configuration.

(b) Sky conditions at 23:55 when altitude record of 1.44 km was achieved.

(c) Icing on tether, iMet, SLWC boxes. Tether is neon green when not covered in ice.

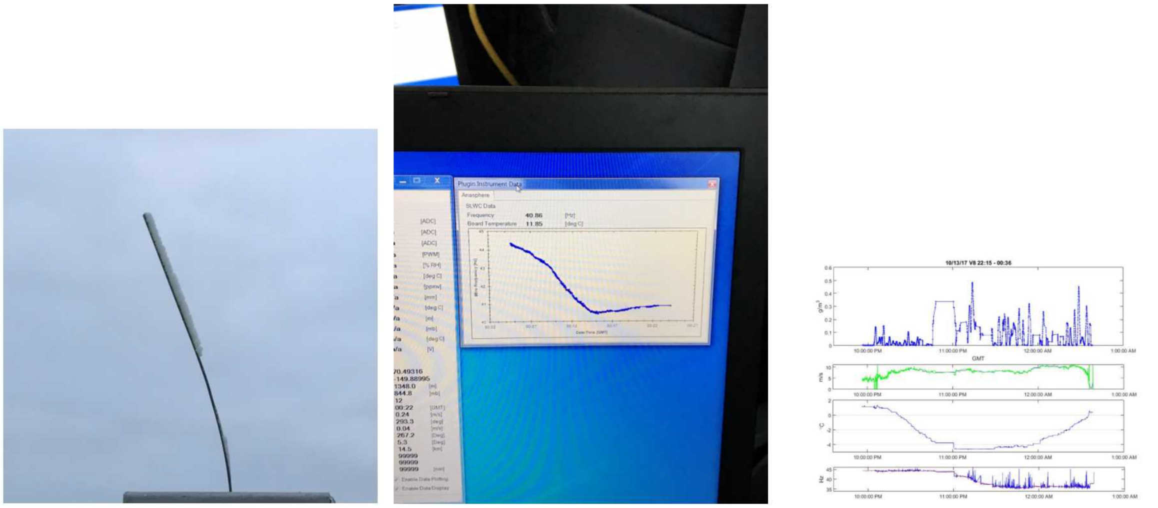

(d) Ice build-up on vibrating wire of SLWC.

(e) Snapshot of computer logging raw frequency data in the vehicle during TBS deployment of SLWCs. Notice the depression of SLWC wire frequency upon entry into cloud, which then begins to increase when the sensor exits the cloud top.

(f) Initial SLWC data and tethersonde SLWC from 13 October 2017. Panel plots from bottoms to top are raw frequency, temperature, wind speed, and calculated concentration of supercooled liquid water content as a function of time.

Figure 3.11. Collection of photos, raw data, and processed data from 13 and 15 of October 2017 TBS flights.

3.2.1 Unique Flights of November 2016 Campaign

This portion of AALCO was humorously dubbed ‘fishing for sky halibut’ as it used a weather balloon on an auto-reeler system, which is very similar to an off-shore fishing reel. The operations for this particular campaign sought to try a smaller balloon that required less equipment and people for operation. Being mid-November, available daylight to work was limited, and temperatures were decreasing such that appendages were becoming cold (Figure 3.12). A larger generator and light source was rented to provide light for operations (Figures 3.13(a) and 3.13(b)). It was found that using the weather balloon had limitations in that it could not carry as much equipment into high altitudes as the helikite and aerostat. Icing on equipment was also a problem (Figure 3.14). The weather balloon was also very dynamic in the cloud, unable to maintain a steady position in the sky. A smaller aerostat was also tried during this deployment (Figure 3.15). Valuable SLWC data was acquired from this time period, which is close to polar winter, when cloud biases in GCMs are largest.

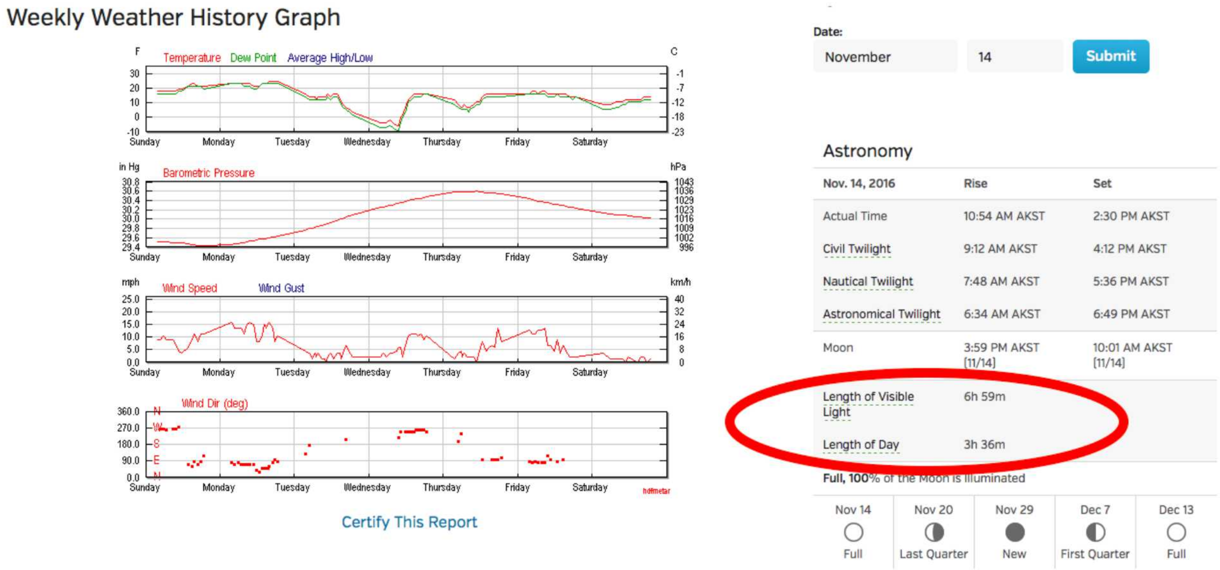

Nov. 14, 2016	Rise	Set
Actual Time	10:54 AM AKST	2:30 PM AKST
Civil Twilight	9:12 AM AKST	4:12 PM AKST
Nautical Twilight	7:48 AM AKST	5:36 PM AKST
Astronomical Twilight	6:34 AM AKST	6:49 PM AKST
Moon	3:59 PM AKST [11/14]	10:01 AM AKST [11/14]
Length of Visible Light	6h 59m	
Length of Day	3h 36m	

Full, 100% of the Moon is Illuminated

Nov 14	Nov 20	Nov 29	Dec 7	Dec 13
○ Full	◑ Last Quarter	● New	◐ First Quarter	○ Full

Figure 3.12. Screenshot of the weather and available daylight at Oliktok Point in mid-November, 2016. From https://www.wunderground.com

3.2.2 Proposed Los Alamos Campaign

Initial plans to test tethered balloon equipment and operations in cold weather included deployment to Los Alamos. Los Alamos National Laboratory has a Restricted Airspace, R-5101, going from the surface to 12,000 feet Mean Sea Level (MSL). This equates to approximately 3500 to 4500 feet AGL. During the winter, mixed-phase and clouds carrying water ice have been observed over Los Alamos, but it is uncertain if the clouds are ever below the top of the R-5101 at 12,000 MSL.

(a) Daylight with light source and balloon on runway. **(b)** Darkness with light source and balloon on runway.

Figure 3.13. Generator and light source to illuminate truck for operations on 15 November 2016 in the daylight (left) and in darkness (right).

Figure 3.14. Deicing the tether going into the auto-reeler from the balloon on 15 November 2016.

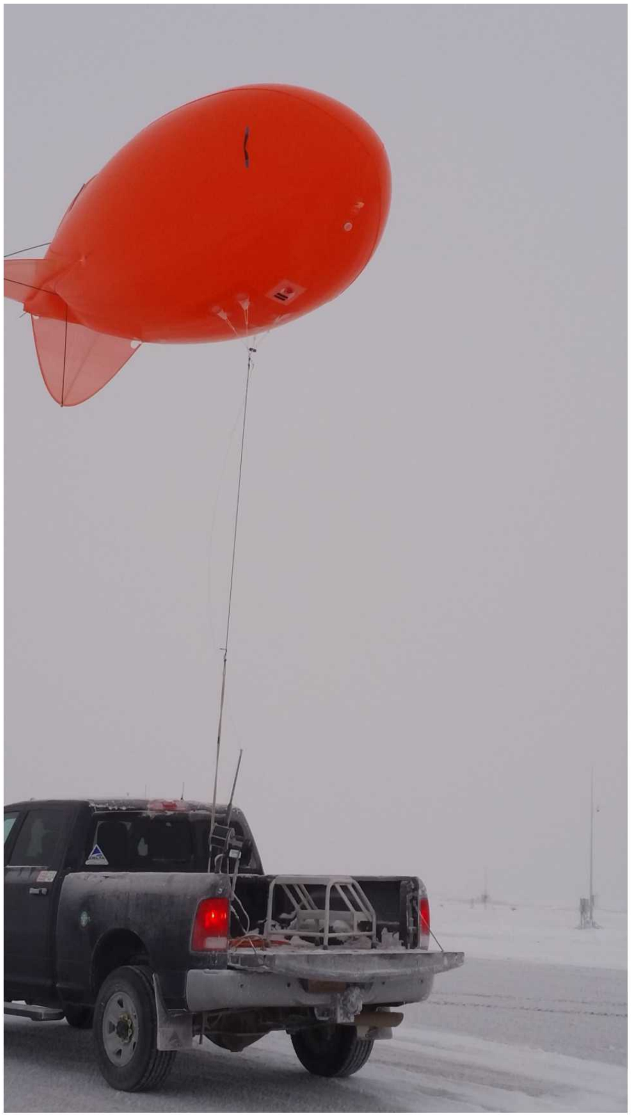

Figure 3.15. Smaller aerostat on 15 November 2016.

By 30 June, 2016, the DOE and LANL NEPA office approved a NEPA For using tethered balloons in the restricted airspace described in NM16-0087. The Sandia National Laboratories NEPA was also needed for this work. Ultimately, the Los Alamos campaign was never performed. Instead, many more desired campaigns at Oliktok Point were performed.

3.3 Analysis of TBS Sensors

Given the new application of the SLWC sensors on the TBS for extended periods of time, supercooled liquid water measurements from adjacent sondes were used to estimate the measurement uncertainty. It was also assumed that liquid water path from the zenith-pointing microwave radiometer at Oliktok Point was adiabatically distributed through the cloud layer(s) using the ceilometer-determined cloud base and Ka-band radar-determined cloud top altitudes for intercomparison. The microwave radiometer does not discriminate between liquid and supercooled liquid, so a high-resolution temperature profile is desirable when conducting comparisons of SLWC sonde and radiometer measurements within Arctic clouds composed of cloud water in both conditions. The near-continuous measurements of temperature collected using a distributed temperature sensing (DTS) system was thus a valuable addition to compare and help interpret the liquid water and supercooled liquid water content of the atmospheric column.

To calculated the SLWC from the TBS, the rate of change of the frequency of the 0.61 mm diameter steel vibrating wire and other atmospheric parameters were used in Equation 3.1,

$$SLWC = -\frac{2b_0 f_0^2}{\varepsilon D \omega f^3}\frac{df}{dt}, \tag{3.1}$$

where b_0 is 2.24 g m-1, f_0 is the un-iced wire frequency, f is the wire frequency at time t, ε is the collection efficiency using the method described in Lozowski et al. (1983), D is the wire diameter, and ω is the velocity of the air relative to the wire. The raw wire frequencies were culled for outliers based on if the frequency deviated over 0.1 Hz from a 30 s moving average of the frequency. The frequencies were then smoothed using the robust LOESS (locally weighted smoothing) model. Wind speeds from the Doppler lidar at the AMF3 were used in the calculation. Pressure, temperature, and relative humidity values from InterMet radiosondes were typically used in the collection efficiency calculation, and if radiosonde measurements were unavailable tethersonde-measured values of these parameters were used. An estimate of median droplet diameter, d_0, was required for the collection efficiency calculation. The SLWC was calculated using median droplet diameters of 11, 16, and 20 μm based on Lozowski et al. (1983) and Bain and Gayet (1982), with results for a median droplet diameter of 16 μm being presented here. The impact of the median droplet diameter used has limited impact on the resulting calculated SLWC, with mean SLWC values for each TBS flight being within $\pm$ 0.01 g m^{-3} for any of the three droplet diameters used. A full discussion of the Anasphere SLWC sonde measurement theory and design is available in Serke et al. (2014) and King et al. (2016).

Uncertainty due to variability of instrumentation design was investigated by operating eight different SLWC sensors side-by-side for over four hours during multiple campaigns. Three such comparison flights were conducted with SLWC sondes on the TBS, while one flight was conducted using a free-flight meteorological balloon. The SLWC values calculated at simultaneous times for each SLWC sonde pair are shown in Figure 3.16. The mean differences between the SLWC values calculated by all sonde pairs operated on the TBS were 0.01 g m^{-3} , and higher for the free-flight balloon pair at 0.06 g m^{-3} . Figure 3.16 shows results of four side-by-side comparison flights of SLWC sondes.

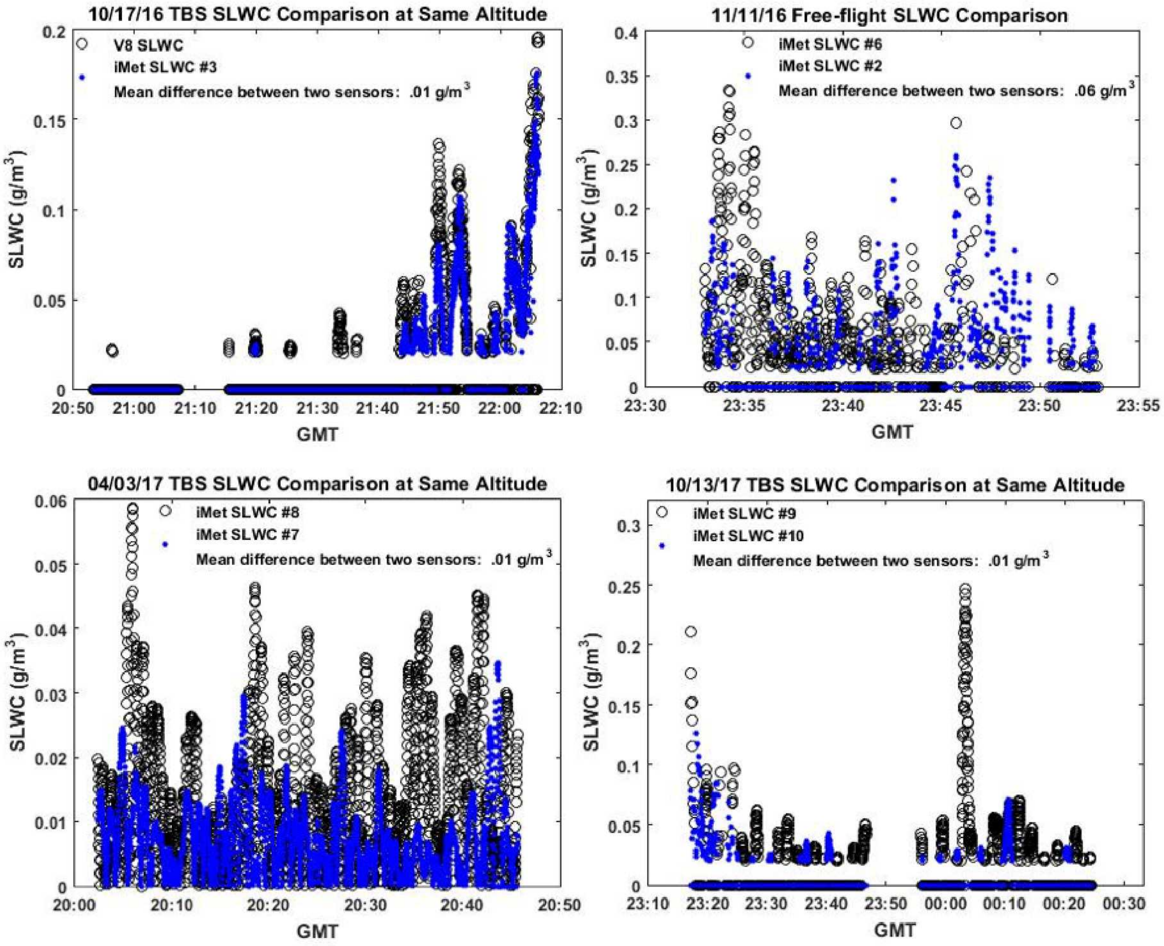

Figure 3.16. Results of four side-by-side comparison flights of SLWC sondes.

A deeper analysis into the 13-14 October 2017 flights between 22:20 Z and 00:20 Z is presented. Two SLWC sondes were operated in the presence of two stratocumulus cloud layers, the lowest with a base at 0.45 to 0.55 km during that time and a second with a base at approximately 0.75 km and a top near 1 km. These cloud layers are representative of the persistent, low-level stratocumulus clouds which commonly occur in the Arctic and are a focus of this project. These cloud layers are part of a larger stratocumulus cloud that persisted at Oliktok Point for 96 hours between

12-16 October 2017. It had a cloud base between 0.1 km m and 1.2 km. During the two hours of 13-14 October 2017 flight, the temperature decreased from -2 °C at the surface to -5.5 °C near 0.6 km. Intermittent frozen precipitation in the form of columns was visually observed beginning at 23:48 Z, converting to flakes at 23:55 Z. An ARM AMF3 sounding occurred at 23:27 Z, and data from that sounding was analyzed using the commercial software RAOB. Liquid water content (LWC) was calculated from the sounding using the enthalpy equation for cloud water (LWC) in RAOB. This equation uses the adiabatic enthalpy (Γ) lapse-rate equation, where LWC is a function of height (z), density (ρ) specific heat at constant pressure (c_p), latent heat of vaporization (L), the dry adiabatic lapse rate (Γ_d), and the moist adiabatic lapse rate (Γ_m) in Equation 3.2:

$$LWC = \frac{c_p}{L} \int \rho(z)(\Gamma_d - \Gamma_m)dz. \tag{3.2}$$

The LWC, calculated by RAOB and shown in Figure 3.17, increased adiabatically through the cloud and reached a maximum of 0.32 g m^{-3} just below cloud top at 0.95 km. Since the entirety of the cloud was below 0 °C, it was assumed that all liquid water in the cloud existed in a supercooled state. Supercooled liquid water content was also calculated from the two SLWC sondes operating on the TBS. The SLWC values calculated from the SLWC sondes at 23:28:54 and 23:29:07 were 0.02 g m^{-3} for the higher sensor sonde at 0.66 km and 0.0 g m^{-3} for the lower sonde at 0.57 km. In comparison, the LWC values calculated by RAOB at the same altitudes were both 0.14 g m^{-3}. A source of this difference might be in the assumed cloud base. The lowest cloud base reported by the AMF3 ceilometer between 23:26 Z and 23:32 Z had a standard deviation of 0.12 km and varied from a minimum of 0.21 km to a maximum of 0.74 km. This variation in the cloud base would be expected to cause significant variation in the SLWC measured by the TBS SLWC sondes. The maximum SLWC observed by the highest altitude TBS SLWC sonde between 23:26 Z and 23:32 Z was 0.14 g $^{-3}$, while the maximum SLWC observed by the lower altitude sonde was 0.05 g m^{-3}. Given the variation in the cloud base during the flight and the spatial variation between the TBS and AMF3 radiosonde measurements, the TBS SLWC sondes and RAOB LWC calculation are concluded to show reasonable agreement.

To compare, the RAOB LWC values calculated from the 23:27 Z AMF3 radiosonde launch, SLWC measured by the two TBS SLWC sensor sondes, the lowest cloud base height measured by the AMF3 ceilometer, and the reflectivity from the AMF3 KAZR are all shown in Figure 3.18. This figure shows nonzero SLWC from the TBS sensors when cloudy mass was present as seen by the ceilometer. The MWR is more difficult to interpret, and any LWC from the microwave radiometer (MWR) makes many assumptions from the retrieval, including the droplet sizes. The MWR have 23.8 and 31.4 GHz derived from radiative measurements with statistical retrieval algorithm that uses monthly derived and location-dependent linear regression coefficients for Brightness Temperature. More information can be sought on `http://www.esrl.noaa.gov/psd/arctic/sheba/notes.html` . Figure 3.19 compares the time profiles of the SLWC sensor and MWR derived values of supercooled liquid water path for two separate flights. Despite the uncertainty in the MWR data product and the new application of the sensor, both data sets show agreement. Future work would to be to apply this to other flights and quantify the bias.

The DTS measurements were compared with the weather balloon sondes (when available) and

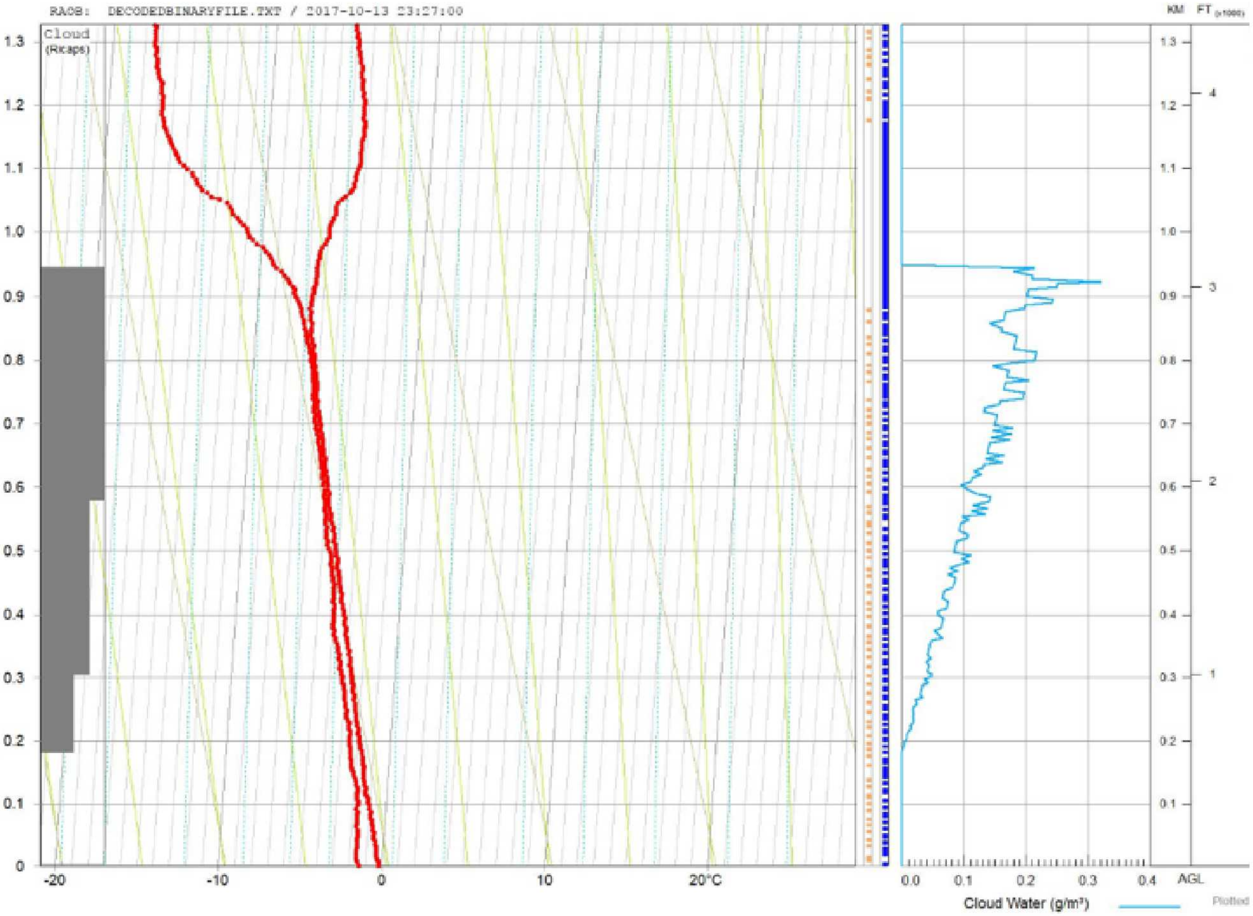

Figure 3.17. Skew-t of 10/13/17 23:30 AMF3 sounding (left) with LWC (right) calculated from RAOB.

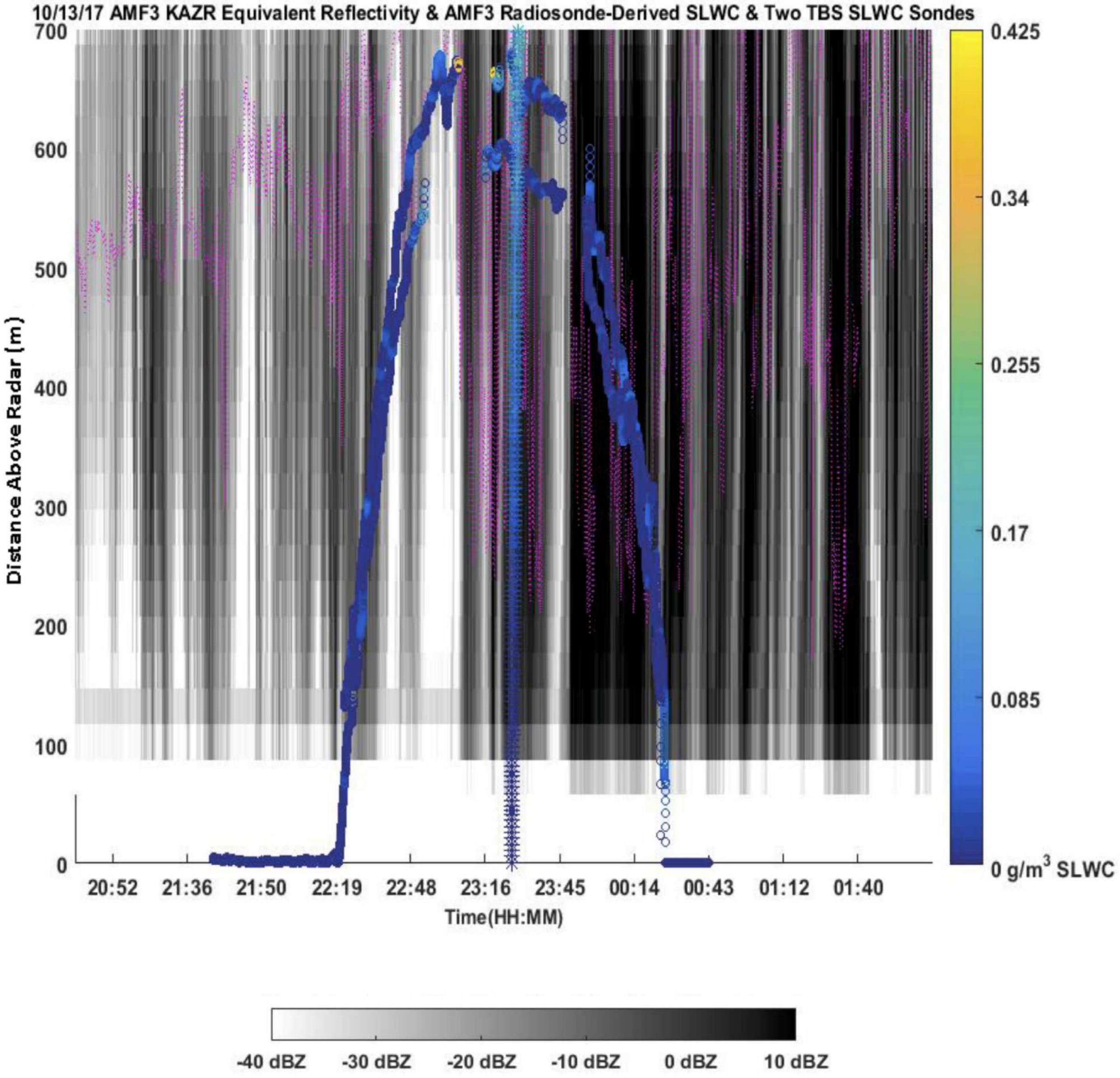

Figure 3.18. TBS Flight of two SLWC sondes with concurrent free balloon radiosonde launch at 23:27 Z on 13-14 October 2017. The stars represent the SLWC values from the radiosonde launch and the circles represent the SLWC values from the TBS sensor sondes. The lowest cloud base height reported by the AMF3 ceilometer is in magenta, and the reflectivity from the AMF3 KAZR is shown in grayscale.

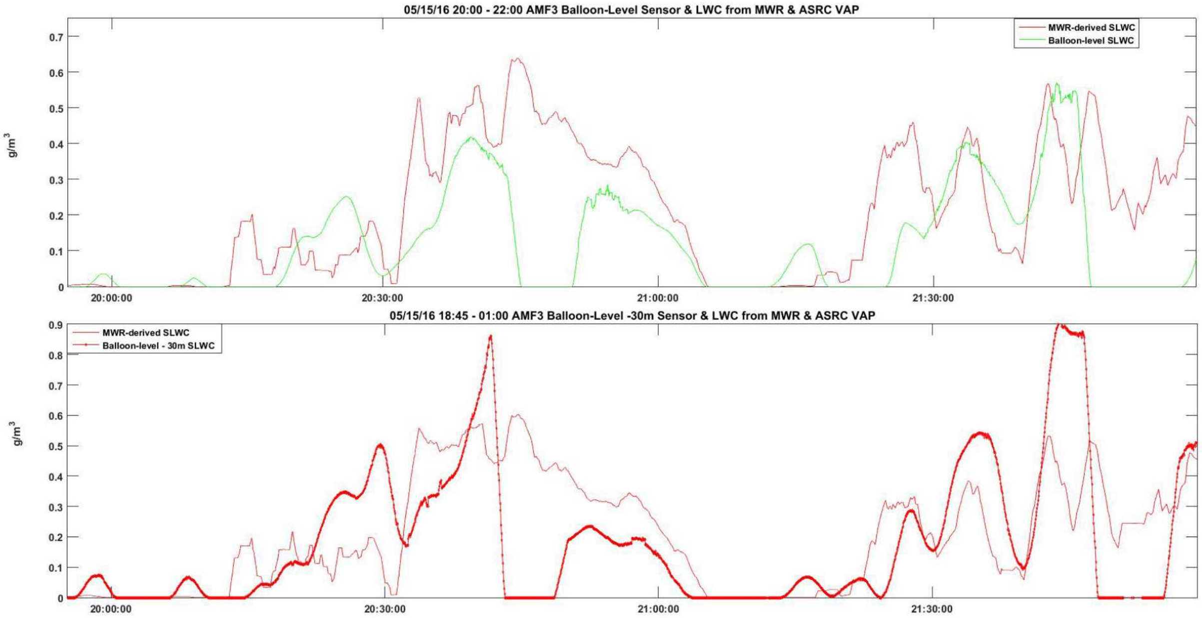

Figure 3.19. MWR-derived supercooled liquid water path and SLWC sensor-derived supercooled liquid water path for two separate flights.

InterMet sondes on the TBS. Figures 3.20 and 3.21 shows the agreement between these sensors and in May 2016 and June 2016. The correlation between these instruments is over 95%, promoting the conclusion that the DTS sensor is viable and valuable for obtaining high temporal and spatial resolution temperature measurements in the boundary layer.

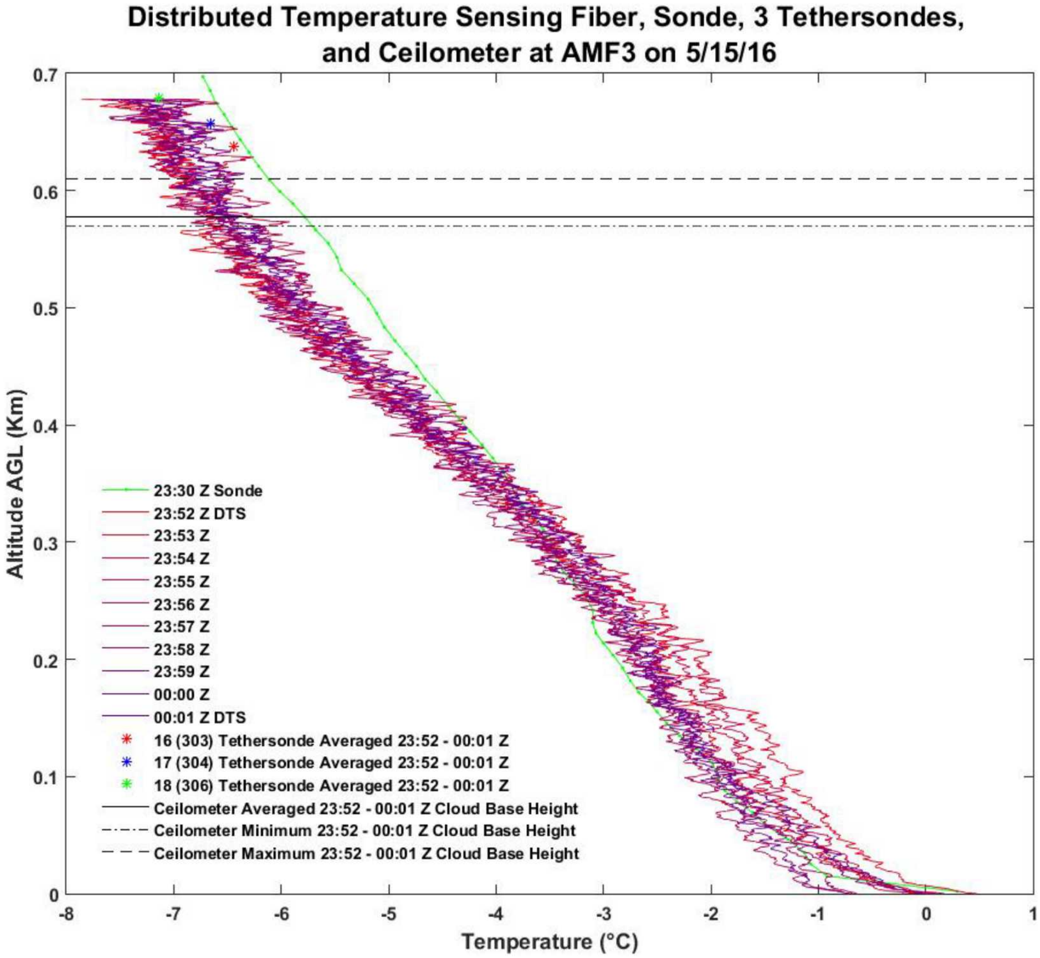

Figure 3.20. DTS temperature with three sondes on the TBS (tethersondes), a weather balloon sonde, and the ceilometer cloud base measured on 5 May 2016.

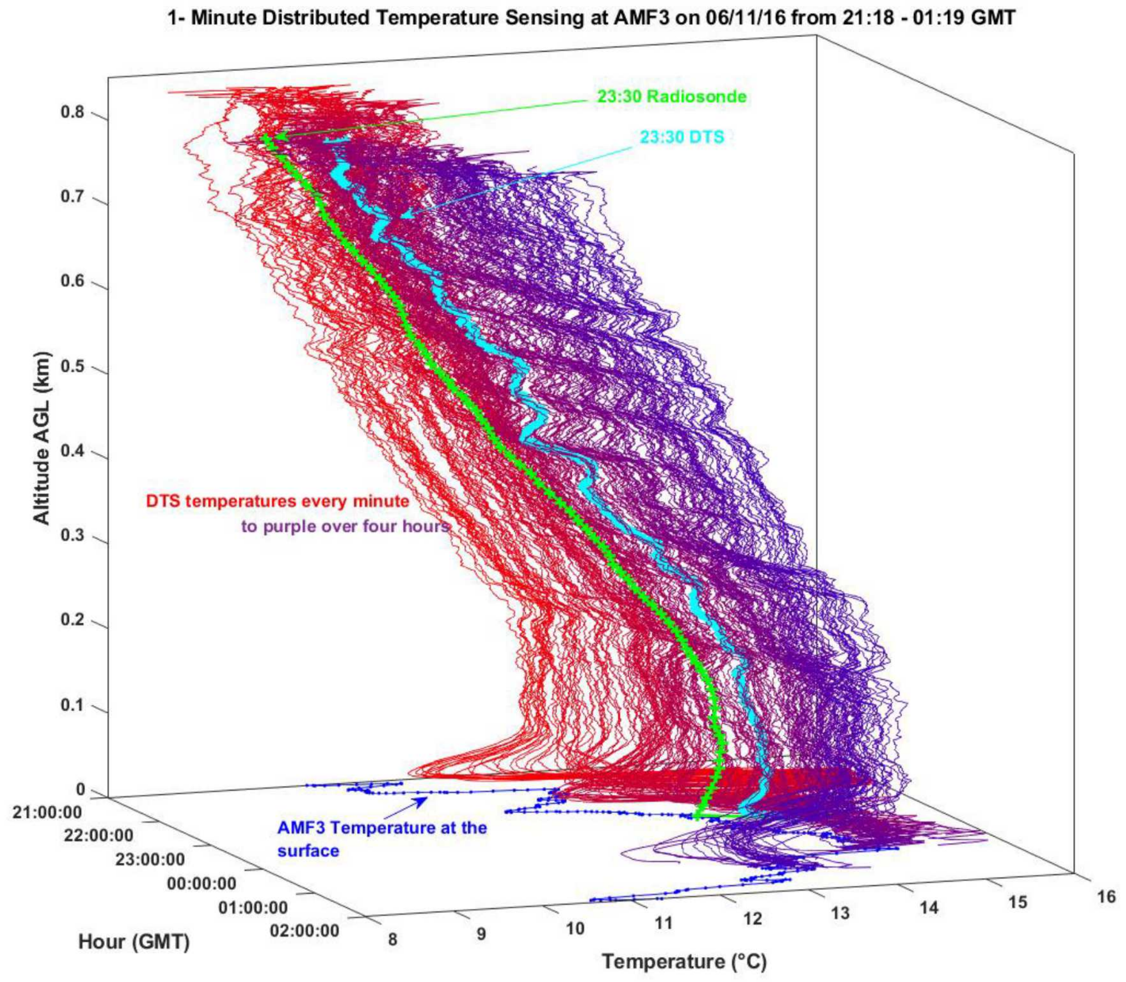

Figure 3.21. TBS DTS measurements collected once per minute with concurrent free balloon radiosonde launch at 23:30 Z on 11 June 2016. The colors show distinction of the DTS measurements in time. The vertical axis is height, one horizontal axis is time, and the other horizontal axis is temperature. The free balloon radiosonde launch is shown in neon green.

Chapter 4

Atmospheric Modeling in the Arctic

4.1 Large Eddy Simulations

Large Eddy Simulations (LES) can provide insight about the three-dimensional structure of a convective cloud field including phase partitioning statistics provided the simulation is validated against measurements. The measurements in this research are from the *in situ* TBS platform, but TBS can collect data only for a limited time and at one coordinate. Radars mostly collect data continuously, but assumptions regarding the phase and content of the environment are needed to convert retrievals into model-meaningful data products. Traditionally, stand-alone LES simulations are performed to reproduce 24 or 48 hours of a idealized or special case study to improve understanding of a process related to cloud macrodynamics, microphysics, or aerosols. Several questions are posed in using the LES model to expand the knowledge-based about boundary layer clouds on the North Slope of Alaska. These questions include:

1. How well do high resolution LES simulations reproduce the point measurements from the TBS?
2. If the LES simulations reproduce the point measurements from the TBS, can they fill-in the gaps for when the TBS is not in operation?
3. What are general properties and macrostructure of boundary layer clouds as learned from the TBS instrumentation and LES simulations?

To answer these questions, the SAM (System for Atmospheric Modeling, version 6.11.1) (Khairoutdinov and Randall, 2003), a model capable of running in large eddy simulation (LES) or cloud resolving model (CRM) configurations, is used for this study. Khairoutdinov and Randall (2003) contains a thorough description of SAM. In SAM, the Morrison two-moment microphysics scheme is used, which predicts the mass and concentration of drops, ice, rain, snow, and graupel (Morrison et al., 2005). The radiation package RRTM is also used. In SAM, anelastic momentum equations are advanced in time for the resolved wind components, the liquid/ice water static energy, and the total non-precipitating and precipitating water mixing ratios in Cartesian coordinates. Higher-order moments resulting from the filtered Navier-Stokes equations are closed by the Deardorff (1980) 1.5-TKE turbulence scheme. Data is downloaded from the ARM data repository, processed for the SAM model, and then used to initialize and/or force SAM.

4.1.1 Preparing Initial Condition and Forcing Files for SAM

SAM has a homogeneous surface boundary layer, meaning either the domain is all-ocean or all-land. The bottom boundary layer has diagnosed moisture and energy fluxes. It was assumed that the best choice for the SAM bottom layer would be all-ocean. The ARM data streams do not produce a measure of sea surface temperature. The International Arctic Buoy Programme has many data tables of buoys near Oliktok and Barrow, and the Buoy numbered 300234061877910 might be closest in latitude and longitude to Oliktok Point. Surface Temperatures (Ts) from the data tables for day 299 of year 2015 show the values to be above freezing and in the teens of degrees. This seems like an odd value given conditions there at the time, given it was freezing just days before the positive jump. The website warns of the data needing some interpretation and QC. It was also found that NOAA produces a global high resolution (0.25x0.25) sea surface temperature reanalysis product (Reynolds et al., 2007). Values for the Oliktok point area, (Latitude: 70.5102778, Longitude: -149.86) were obtained. An example of the NOAA sea surface temperature (SST) reanalysis product is shown in Figure 4.1. Although SAM calls for a SST over an ocean, many times of the year at Oliktok, the surface is covered in ice and temperatures are significantly below freezing. The SST, beneath the ice, is never much below freezing. It was determined, then, that a different data product was needed for the SAM surface temperatures.

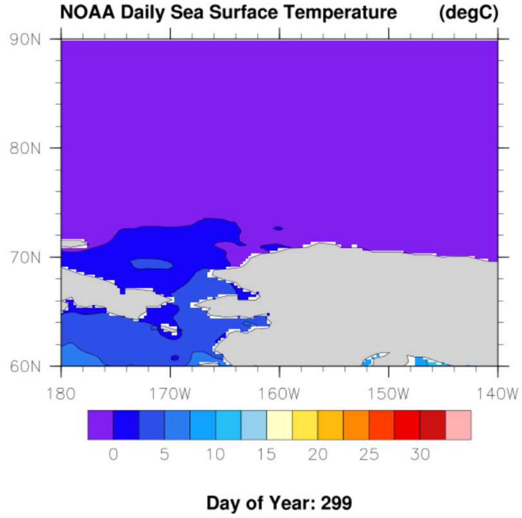

Figure 4.1. NOAA buoy data for DOY 299, 2015.

The first method tried to create initial condition and forcing files for SAM was to use ECMWF column data from the ARM Data Discovery repository. The data from the column nearest Oliktok or Barrow from the ECMWF model is extracted and available for download. See Figure 4.2 for an example of the web interface. Being a model itself, the ECMWF data set has everything SAM needs to get started and stay running: sensible and latent heat flux; surface temperature; tendencies of water vapor, temperature, horizontal winds, and pressure; and water vapor, temperature, horizontal winds, and pressure profiles for initialization.

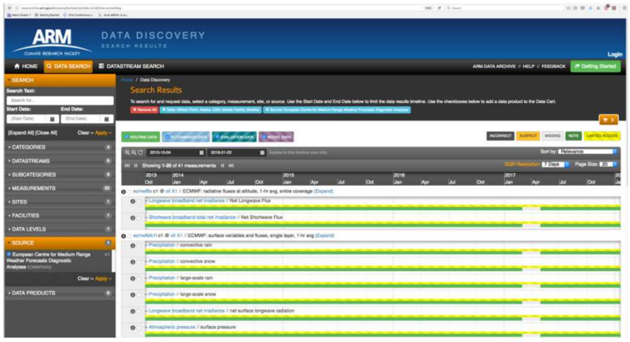

To search for and request data, select a category, measurement, site, or source. Use the Start Date and End Date below to limit the data results timeline. Use the checkboxes below to add a data product to the Data Cart.

ECMWF: radiative fluxes at altitude, 1-hr avg, entire coverage (Expand)
Longwave broadband net irradiance // Net Longwave Flux
Shortwave broadband total net irradiance // Net Shortwave Flux
ECMWF: surface variables and fluxes, single layer, 1-hr avg (Expand)
Precipitation // convective rain
Precipitation // convective snow
Precipitation // large-scale rain
Precipitation // large-scale snow
Longwave broadband net irradiance // net surface longwave radiation
Atmospheric pressure // surface pressure

Figure 4.2. Screenshot of the ARM Data Discovery web interface as seen in February 2018.

The ECMWF reanalysis was set-up for October 16, 2016, when TBS operations and the SLWCs measured non-zero SLWC in a boundary layer cloud. SAM simulated the conditions given from ECMWF for 24 hours with horizontal resolutions of $dx = dy = 100$ m, vertical resolution of $dz = 40$ m, and a total domain size of $Lx = Ly = 12.8$ km and $Lz = 5.1$ km. As seen in Figure 4.3, ECWMF does not have the right atmospheric conditions to produce a cloud when a cloud was observed and when the TBS was in operation. The occurrence of SLWC in the time-height contour plot of Figure 4.3 misses the sub-kilometer SLWC measured from the TBS. Although there is a non-zero presence of SLWC from SAM, the timing of that occurrence called into question the use of ECMWF. This is reiterated from knowledge gained regarding its bias in cloud climatologies as discussed in Chapter 2, so daily differences might affect how and when a cloud is produced in SAM, and it was questioned how this would look for future TBS days when needing to compare with SAM.

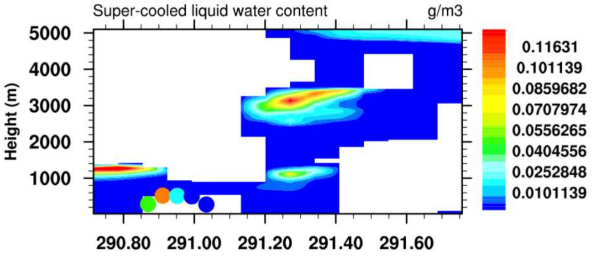

Figure 4.3. SAM simulation and TBS measurements of SLWC in g m^{-3} for 16 October 2016, or about day 290 of the year 2016. SAM is initialized with ECMWF reanalysis. The measurements of SLWC from the TBS are shown as the colored-contour circles.

To determine how different the ECMWF profiles and the daily profiles were, ARM radiosondes from weather balloons were compared with the ECMWF column profiles for days of the year 296.72 and 286.97. Figure 4.1.1 shows this comparison. The lack of the inversion in the potential temperature (TP) at about 600 m in the ECMWF column profiles on DOY 286.72 and 1000 m on DOY 286.97 are the main drivers for not producing a cloud from using the ECMWF. Additionally, the different magnitudes of available water vapor at different heights are also responsible for the formation and maintenance of the cloud. Through a series of tests with SAM, it was determined the primary driver for the timing and magnitude of the cloud are the potential temperature and water vapor profiles. The horizontal winds did not affect the cloud the in simulation as much. These small differences led to abandoning the use of ECMWF data, despite its ease for use in SAM, and the move to use the balloon sondes and other instrument-based measurements at the AMF3 Oliktok site.

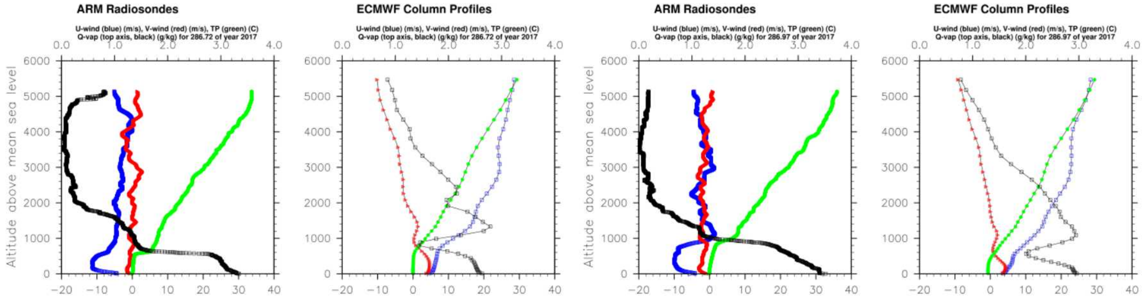

(a) Ballon soundings (left) and ECMWF column profiles (right) for DOY 286.72.

(b) Ballon soundings (left) and ECMWF column profiles (right) for DOY 286.97.

Figure 4.4. ARM Radiosondes from weather balloons compared to ECMWF column profiles taken from approximately 12 October 2016, or days of year (DOY) 286.72 and 286.97, respectively. Horizontal winds, u and v, are in blue and red. Potential temperature (TP) is in green. Water vapor (Q-vap) is in black and with its magnitudes in height along the top horizontal axis.

Using the ARM data to initialize SAM has the benefit of being meteorologically consistent with what was observed and measured during TBS operations, but has the disadvantage of not being straightforward to incorporate into a numerical model. Some of the issues that plagued running SAM with ARM data were numerical instabilities associated with assumptions in developing the tendencies. Tracking down the source of this instability took considerable time, and it was eventually found that the derived tendencies were introducing too much heat into the model. The temperature in SAM would start to extremely cold temperatures of less than 300 ° K to 900 ° K before crashing after simulating 4 hours. The temperature tendencies were reduced iteratively in their production steps until the simulation was stable with temperatures that were appropriate for October 2016 at Oliktok. Deriving a way to determine tendencies based more on ARM data, and not on objective criteria of having SAM not crash, would be an area of future work.

At AMF3, the balloon sondes are hand launched and dependent on if the operator can launch at a specific time. Sonde launches, consequentially, are sometimes missing or at irregular intervals compared to auto-launches and launches within the lower 48 United States. The ARM data server, however, has a data product called Interpolated Sonde where sounding data is linearly interpolated into daily files with 60 second temporal resolution up to 40 km on a fixed time-height grid (Jensen and Toto, 2016). The data product has 332 levels with a 20 m resolution from 0 to 3.5 km above ground level, then 50 m from 3.5 to 5 km, and then 100 m from 5 to 7 km. It is unknown how accurate the interpolated sonde is for AMF3, so a correlation was found between the DTS and the Interpolated Sonde data product. Figure 4.5 shows this relationship with a 0.77 °C difference assuming the heights are within 5 m of each other. Given the demonstrated accuracy and precision of the DTS when compared with tethersondes and balloon sondes and that the Interpolated Sonde does not deviate too much from the DTS temperature profile, confidence was placed in the ability to the use the Interpolated Sonde data product as being close to the real environmental temperature to initialize SAM.

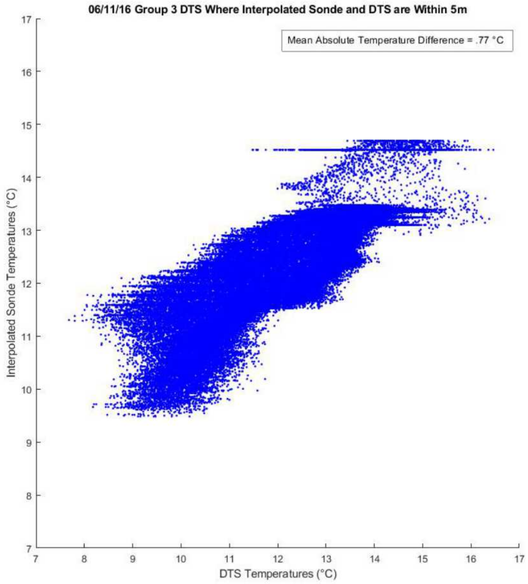

Figure 4.5. Testing the correlation of DTS Temperatures and Interpolated Sonde Temperatures for 11 June 2016, assuming the DTS and Interpolated Sonde Heights are within 5 m of each other.

Using the interpolated sonde product, ecor, and meteorological data streams from Oliktok, a cloud containing super cooled liquid water was simulated by SAM the same time one was measured by the instrumentation on the TBS for October 13, 2016. Figure 4.6 shows the model and measurement output as a function of time. Sensitivity tests were conducted to see how the comparison of the model and sensor measurements could be improved. Starting 0.35 days earlier and allowing for more spin-up allowed

4.1.2 SAM LES simulations compared with Oliktok Point Observations

During TBS Oliktok Point AALCO campaign, the ARM data streams on the archive has no instrument-based data about liquid water content or ice water content. The measurements from the Tethered Balloon's SLWC sensor is, so far, the only data stream that can be compared to the model.

Ka-band ARM zenith radar (KAZR) is an ”evolutionary follow-on to millimeter-wavelength cloud radar”. It provides vertical profiles of clouds with reflectivity, radial Doppler velocity, and spectra width. It operates at 35 GHz, the millimeter wavelengths (between 30 and 300 GHz and 10 to 1 mm wavelengths). The Ka-band designation is between 26.5 and 40 GHz.

4.2 Superparameterization

Cloud and convective parameterizations are needed in large-scale, whole-earth atmospheric and earth system models due to limitations placed on horizontal and vertical resolutions based on computational resources, which are much more coarse than the resolutions needed to explicitly resolve these important processes with known physics. The Multi-scale Modeling Framework (MMF; Grabowski, 2001; Khairoutdinov and Randall, 2001; Randall et al., 2003) or “superparameterization” approach was developed to explicitly resolve convection and remove dependence on convection and cloud parameterizations in large-scale models by embedding a low-resolution cloud resolving model (CRM) into each column of a traditional global climate model (GCM). This replaces the convective parameterization and large-scale cloud condensation parameterizations altogether. This approach attempts to balance physical realism with computational efficiency by using a relatively coarse resolution, two-dimensional CRM for the embedded model. This makes the MMF approach much more computationally tractable than running a global cloud system resolving model. This framework has been implemented using different host GCMs (Khairoutdinov and Randall, 2001; Tao et al., 2009) and with different schemes for handling turbulence, clouds, and aerosols (Cheng and Xu, 2011, 2013).

Even at coarse resolution (1 to 4 km horizontal grid spacing for the embedded CRM), the MMF has been demonstrated to significantly improve a number of long-standing model shortcomings. The list of improvements include an improved simulation of the Madden Julian Oscillation (Khairoutdinov et al., 2008; Benedict and Randall, 2009; Randall, 2013), improved diurnal cycle of precipitation (Khairoutdinov et al., 2005; Pritchard and Somerville, 2009b,a; Pritchard et al., 2011), and improved intensity of precipitation (DeMott et al., 2007; Kooperman et al., 2016). However, many biases remain, including low-level (boundary layer) clouds (Marchand and Ackerman,

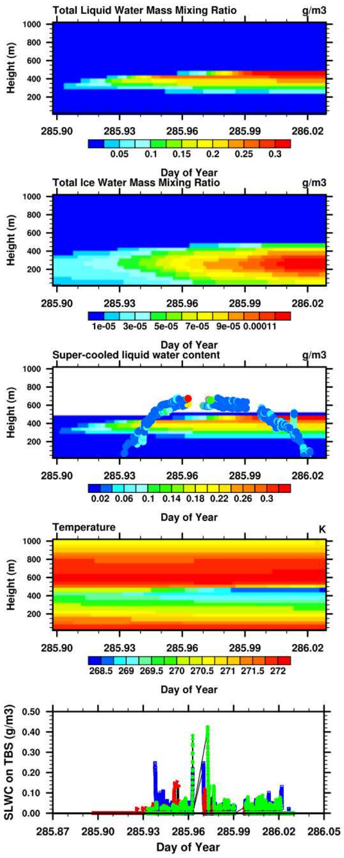

Figure 4.6. Simulation output from SAM of 13 October 2016 comparing with SLWC sensors on TBS. The middle plot shows the time-height evolution of the domain-averaged supercooled liquid water content as a colored contour with the colored circles the SLWC sensor values at the same time height. The bottom most line plot is the magnitude of the SLWC from all three sensors on the balloon in time.

2010). Many of the remaining shortcomings are linked to scales smaller than those resolvable by the coarse-resolution of the embedded CRM in existing formulations of the MMF, such as shallow convection and boundary layer turbulence. Parishani et al. (2017) show promising improvement in the simulation of these processes by pushing the embedded CRM to much higher resolution, stepping into large-eddy-resolving scales. Higher order turbulence closure methods have also shown improvement (Cheng and Xu, 2011, 2013).

The goal of this study is to understand whether or not super-parameterization can improve simulation of Arctic clouds, with a particular emphasis on the phase partitioning of those clouds. In order to answer that question, we compare simulations of present-day climate from both super-parameterized (with the MMF) and traditionally-parameterized (without the MMF) configurations of a large-scale model with retrievals of cloud amount partitioned by cloud phase from CALIPSO satellite retrievals, and of liquid water path and cloud fraction derived from microwave radiometer retrievals at the ARM north slope of Alaska (NSA) research site at Barrow, Alaska. To further understand the limitations of the framework and gain insight into the physical processes responsible for the identified differences in the simulations, we perform additional simulations with the stand-alone embedded CRM in various configurations. These sensitivity studies provide additional insight into the physical controls on Arctic clouds.

4.2.1 Model configurations

The version of the MMF used here is the Super-parameterized Community Atmosphere Model (SP-CAM), version 2.[1] This version of the MMF has been implemented using the National Center for Atmospheric Research (NCAR) Community Atmosphere Model Version 5 (CAM5; Neale et al., 2012) as the host GCM and the System for Atmospheric Modeling (SAM) as the embedded CRM. Because the embedded CRM is built as a compile-time option within the Community Earth System Model (CESM) build framework, we can run either the super-parameterization or the traditional CAM5 physics using the same host model codebase. We perform two multi-year simulations using the SP-CAM codebase. First, we perform a control simulation with the default CAM5 (non-superparameterized) configuration, which uses the finite volume dynamical core at 2 degree horizontal resolution with 30 vertical levels. The second is a SP-CAM simulation, using the same finite volume dynamical core at 2 degree resolution in the outer model, but with an embedded cloud resolving model running with a 2-dimensional, 32x1 column domain with 4 km horizontal grid spacing, and the 2-moment cloud microphysics parameterization described in Morrison et al. (2005). The embedded CRM in each GCM column shared the bottom 28 levels with the outer model. Both simulations were run using present day conditions, forced with monthly-evolving sea surface temperatures and sea ice extent from present day observations, and climatologies were created from the monthly-mean outputs for analysis.

---

[1] `https://wiki.ucar.edu/pages/viewpage.action?pageId=205489281`

4.2.2 Comparisons of cloud amount with CALIPSO

Obtaining robust observations of cloud properties is often difficult, but this is an even more difficult task in the Arctic. Sparsely populated and incredibly harsh terrain make obtaining *in situ* observations and ground-based retrievals difficult, and in fact a major contribution of this project, and of the ARM program as a whole, has been the wealth of data that has been collected over the ARM NSA site. Nonetheless, ground-based observations provide only a limited sample. For a broader picture of clouds, satellite retrievals of cloud properties often provide an attractive baseline for model evaluation due to their comprehensive spatial coverage. For example, Mioche et al. (2015) reported the vertical, spatial, and seasonal ubiquity of mixed-phased clouds over the Eastern and Western Arctic using a combined radar/lidar retrieval algorithm from CALIPSO and CLOUDSAT retrievals. Uncertainties in their approach include radar reflections from the ground and attenuation leading to misclassification.

In this study, we use retrievals from the Global Climate Model (GCM)-Oriented CALIPSO Cloud Product (CALIPSO-GOCCP; Chepfer et al., 2010) to provide a broad picture of cloud properties throughout the Arctic. CALIPSO uses a vertically-pointing lidar to actively probe the vertical structure of clouds in a 2-dimension curtain along its orbit. The CALIPSO-GOCCP cloud phase product (Cesana and Chepfer, 2013) additionally partitions cloud fraction into categories of liquid or ice (or undefined in cases in which the retrieval cannot determine phase, typically in conditions in which the backscatter from the lidar is primarily aerosol or very thin clouds). The CALIPSO cloud phase product used here aggregates data onto a 2 x 2 degree grid and includes both the profiles of liquid, ice, and undefined-phase cloud fraction, as well as the vertically-project cloud cover (the fraction of the horizontal area of each grid box with cloud overhead) separated by phase and by height category (low, middle, high, and total).

While satellite retrievals of cloud properties such as those from CALIPSO can provide good spatial and temporal coverage for model evaluation, actually comparisons between models and satellite retrievals require a good deal of care and can often be misleading if performed naively. This is due to fundamental differences between what models can simulate and what can be observed from space, due primarily to limitations and assumptions in satellite retrievals, but also due to a scale mis-match between the resolution of typical global climate models and the scales at which satellite perform retrievals (e.g., Hillman et al., 2018). A framework for model evaluation of cloud properties has emerged in recent years in which a so-called “satellite simulator” is used to simulate from fundamental model fields a specific satellite retrieval, in effect providing a description of what a particular satellite instrument would see, given the model simulated world. This approach turns the problem of comparing cloud properties from models with satellite retrievals into a forward-modeling problem (modeling the satellite-view of the clouds) as opposed to an inverse problem (inferring model-relevant fields from retrievals), and in doing so attempts to account for limitations and assumptions in the retrievals. This framework has been proven useful in a number of model evaluation studies (Klein and Jakob, 1999; Webb et al., 2001; Lin and Zhang, 2004; Zhang et al., 2005; Wyant et al., 2006; Marchand and Ackerman, 2010; Pincus et al., 2012; Kay et al., 2012; Klein et al., 2013; Bodas-Salcedo et al., 2011; Kay et al., 2016). Simulators have been developed for a variety of satellite platforms, many of which have been collected and packaged together with a common interface into the Cloud Feedback Model Intercomparison

Project (CFMIP; Webb et al., 2017) Observation Simulator Package (COSP; Bodas-Salcedo et al., 2011). COSP includes simulators for the International Satellite Cloud Climatology Project (Klein and Jakob, 1999; Webb et al., 2001), the Multi-angle Imaging Spectro-radiomter (Marchand and Ackerman, 2010), the Moderate Resolution Imaging Spectroradiomter (Pincus et al., 2012), the CloudSat cloud radar (Haynes et al., 2007), and the Cloud-Aerosol Lidar and Infrared Pathfinder Satellite Observation (CALIPSO) lidar (Chepfer et al., 2008), which will be used in this study.

Kay et al. (2016) demonstrate the utility of this framework relevant to Arctic clouds in an evaluation of cloud phase in a simulation using the Community Atmosphere Model Neale et al. (2012), in which it is revealed that CAM5 underestimates the occurrence of liquid cloud relative to CALIPSO retrievals, resulting in an underestimate of total cloud both Arctic-wide and globally. Additionally, cloud phase biases appeared to be too closely tied to the seasonal cycle of temperature, suggesting that the representation of cloud phase in the model is overly dependent on temperature. Kay et al. (2016) were able to reduce the biases in cloud phase with a simple adjustment to a parameter in the shallow convection scheme. While much of the error in cloud phase likely arises due to poor representation of ice formation processes in current cloud microphysics parameterizations, the improvement obtained through a simple adjustment to the convective parameterization suggests that further improvement might be obtained using a more realistic (or physically-based) treatment of cloud and convective processes altogether, such as the superparameterized approach used here.

In order to use the satellite simulator approach to evaluate cloud properties in SP-CAM for this study, a major effort was undertaken to port COSP to work inline with the SP-CAM code. While COSP has been fully ported to CAM5 in the CESM (Kay et al., 2012, 2016), the implementation in SP-CAM is unique in that because SP-CAM explicitly simulates clouds on a 1-4 km scale, it is important to use the fully-resolved CRM fields as input to COSP rather than the domain averages assumed in the CAM5 implementation to avoid introducing artificial errors in using the subcolumn sampling in COSP (e.g., Hillman et al., 2018).

Using the simulator here is relevant because it includes the effect of attenuation of the lidar signal by hydrometeors between the volume and the detector, so that the cloud fraction reported here may differ from the actual low-level cloud fraction reported by the model (as previously found in Liu et al., 2017). For example, low-level cloud fraction can be much larger in the model than the simulator reports due to the fact that much low-level cloud is missed by the lidar retrieval as the signal is attenuated by mid and high-level cloud layers that exist above the low-level cloud in the model. This illustrates the importance of accounting for these effects one way or another when making comparisons between models and remote sensing retrievals. The simulator also mimics the CALIPSO cloud phase discrimination, which is important for comparisons of separate liquid and cloud ice fraction.

Figure 4.7 shows the climatological seasonal mean vertically-projected cloud cover from CALIPSO retrievals and CALIPSO-simulated retrievals from CAM5 and SP-CAM model simulations for the entire Arctic (60N to 90N). Area-weighted means are indicated in the titles of each plot. The seasonal cycle in cloud cover is evident by comparing the area averages in the CALIPSO retrievals, with cloud cover reaching a maximum value of 77% in the fall (SON) season and then reaching a minimum of 61% in the winter (DJF) season. Both model simulations underestimate the total cloud cover in all seasons. The underestimate in total cloud cover in CAM5 is consistent with the Kay et al. (2016) results. The SP-CAM simulation tends to produce more total cloud cover than CAM5, however, reducing the bias relative to CALIPSO retrievals in all seasons *except* the summer (JJA). However, the seasonal cycle in cloud cover is much smaller in magnitude in the SP-CAM simulation, with seasonal cloud cover reaching a wintertime minimum of 60% and a fall maximum of only 68%. This is a difference from minimum to maximum of only 8% cloud area, compared to the 16% cloud area difference between minimum and maximum in the CALIPSO retrievals, and the 24% cloud area difference in the CAM5 simulation.

While the biases in total cloud cover are somewhat reduced in the SP-CAM simulation, it appears that this occurs due to an unfortunate combination of compensating errors. Figure 4.8 and Figure 4.9 show the climatological seasonal mean liquid and ice cloud cover, respectively. The plots of liquid cloud cover shown in Figure 4.8 reveal the familiar underestimate in liquid cloud in CAM5 shown in Kay et al. (2016). However, while total cloud amount was generally increased in the SP-CAM simulation relative to the CAM5 simulation, Figure 4.8 shows that we get no such improvement in the amount of liquid cloud in the SP-CAM simulation, and in fact the liquid cloud amount is systematically even lower than that in CAM5, leading to an even larger negative bias relative to the CALIPSO retrievals. Figure 4.9 shows that the apparent improvement in total cloud in SP-CAM is due to a systematic *overestimation* of ice cloud, with ice cloud cover overestimated by as much as 12% cloud area in the SP-CAM simulation relative to CALIPSO retrievals. Ice cloud amounts in CAM5, on the other hand, are actually quite similar to those in the CALIPSO retrievals.

To further understand these biases, analysis is focused on the location of the ARM north slope of Alaska (Barrow) site, where we have additional instrumentation to measure cloud properties and obtain a “ground-up” view to complement the “top-down” comparison of clouds offered by the satellite retrieval comparison. The CALIPSO cloud lidar is able to profile the vertical column of cloud and thus provide a picture of cloud fraction by height, separated by phase. Figure 4.10 shows profiles of liquid, and ice cloud fraction by height over the ARM NSA site from CALIPSO retrievals and CALIPSO-simulated retrievals from CAM5 and SP-CAM. The SP-CAM simulation has much more high-level cloud throughout the seasonal cycle than both CAM5 and CALIPSO, but less low-level cloud in the fall and winter seasons. The overestimate in high-level cloud is due to an overestimate of upper-level ice cloud (bottom panel), and the underestimate in low-level cloud in the fall and winter seasons is due to an underestimate in low-level liquid cloud (middle panel). The overestimate in high-level ice cloud is persistent throughout the seasonal cycle, suggesting that there is something fundamental about the SP-CAM configuration that is over-producing ice cloud. The CAM5 profiles are actually much more consistent with the CALIPSO retrievals, with the exception of the summer season in which both low-level liquid and high-level ice are overestimated relative to CALIPSO.

The primary finding in this analysis thus far is that SP-CAM produces much more high-level ice cloud in the Arctic than CAM5, and the simulator comparison suggests that this is in fact an overestimation of cloud. While the satellite simulator framework provides an easy way to make robust comparisons with satellite retrievals, it is difficult to back out the source of identified biases using the simulator comparisons alone. This is because both the satellite retrievals and the

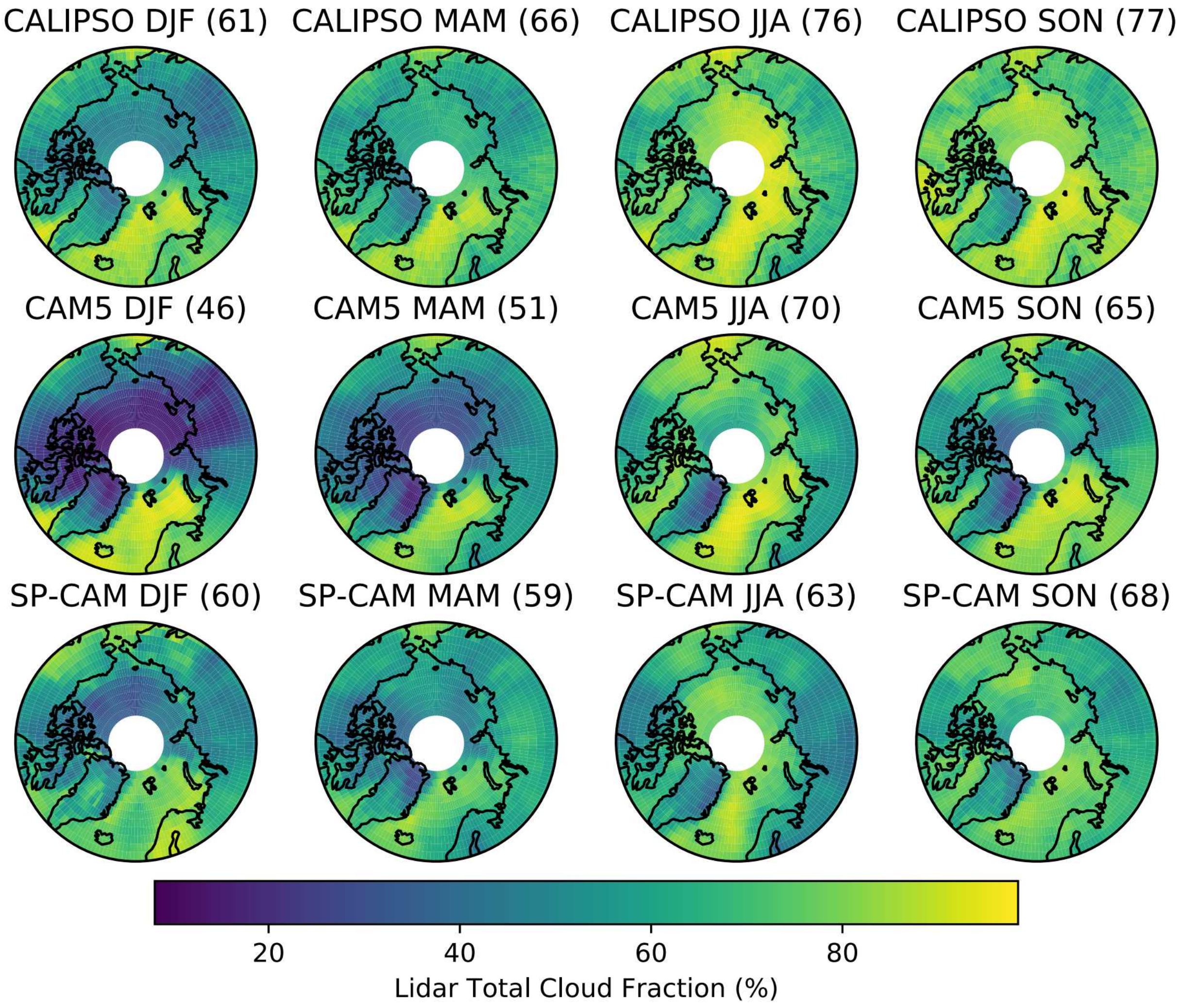

Figure 4.7. Seasonal mean total cloud area from CALIPSO retrievals (top) and CALIPSO-simulated retrievals from CAM5 (middle) and SP-CAM (bottom) model fields.

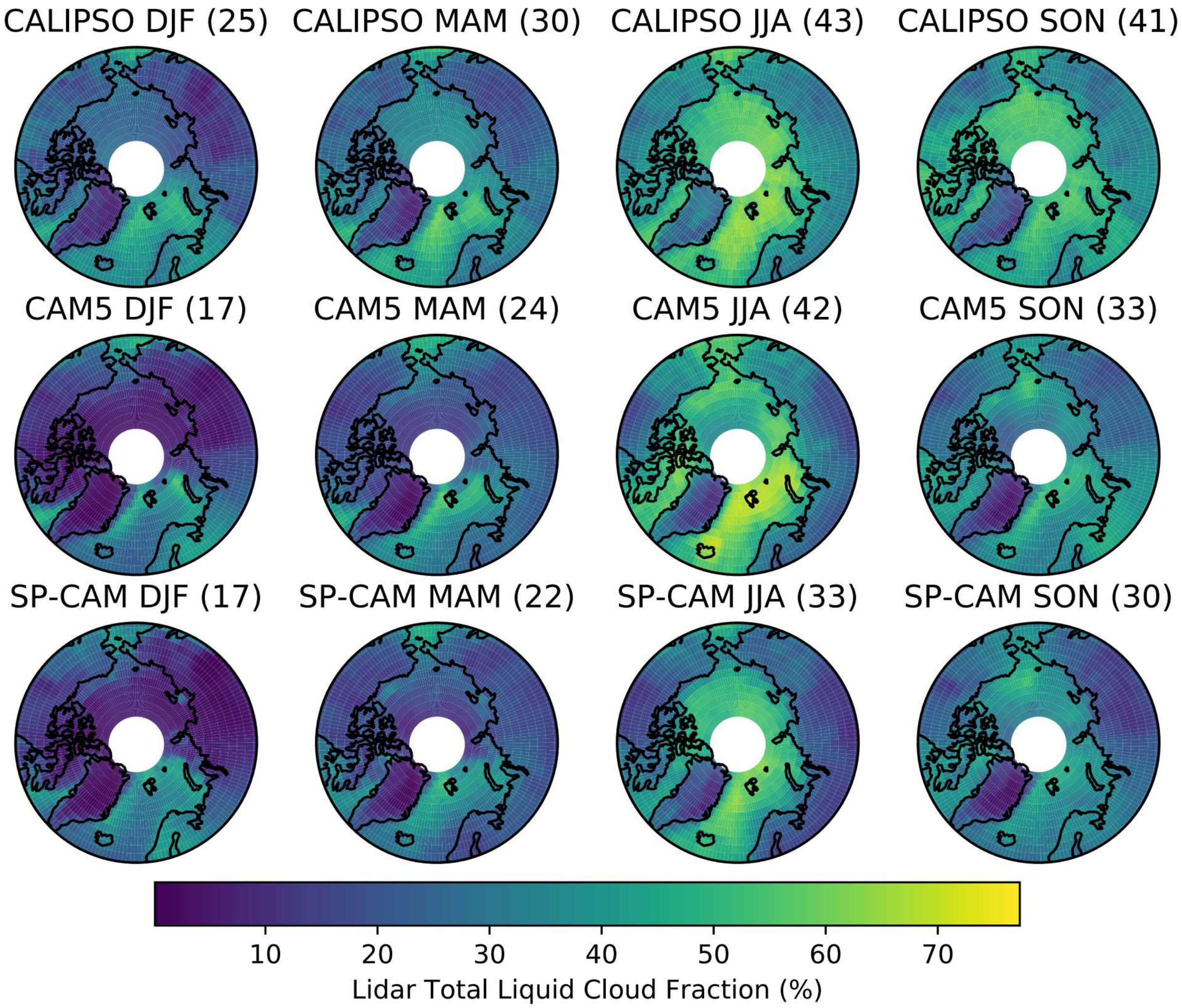

Figure 4.8. Seasonal mean liquid cloud area from CALIPSO retrievals (top) and CALIPSO-simulated retrievals from CAM5 (middle) and SP-CAM (bottom) model fields.

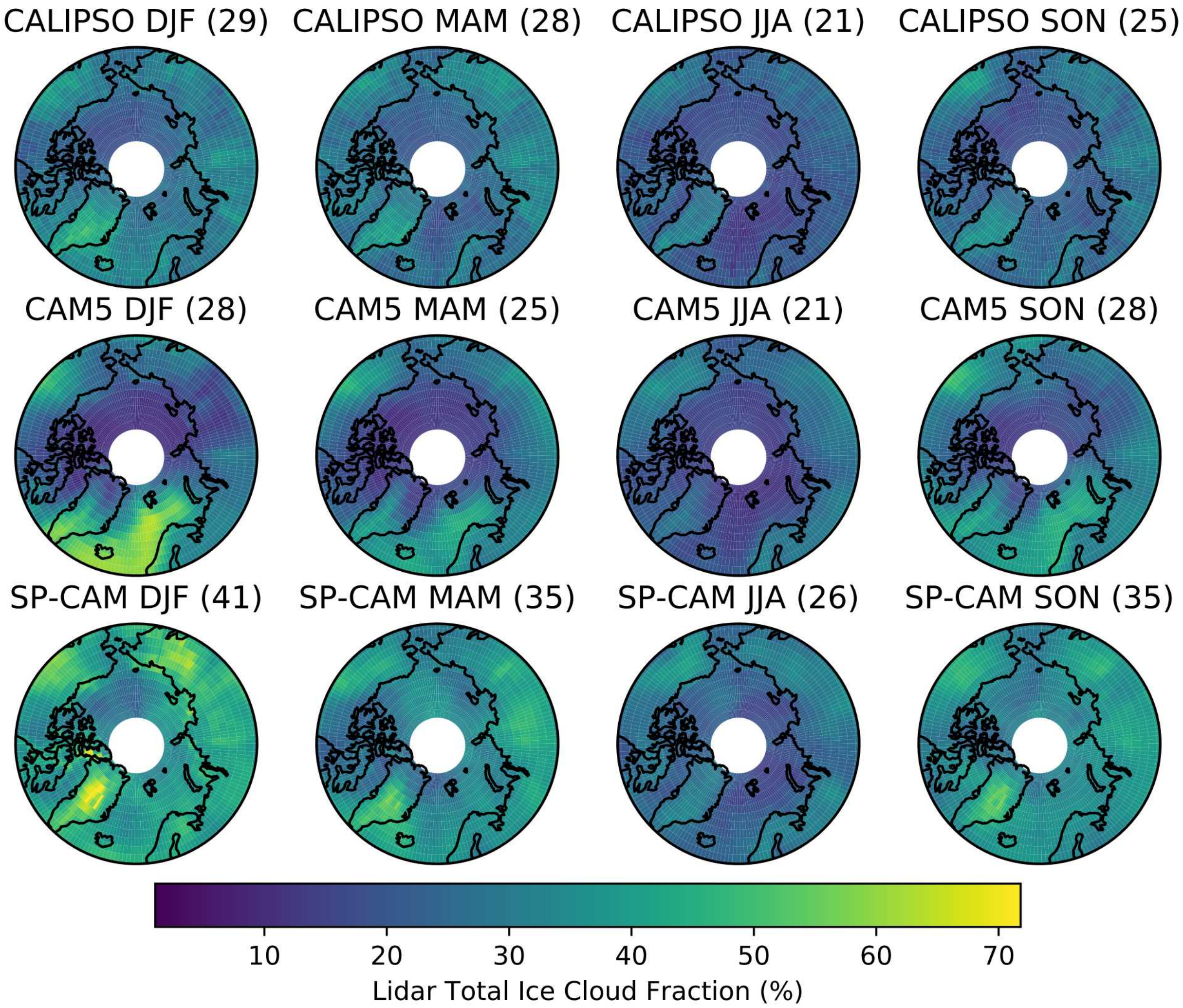

Figure 4.9. Seasonal mean ice cloud area from CALIPSO retrievals (top) and CALIPSO-simulated retrievals from CAM5 (middle) and SP-CAM (bottom) model fields.

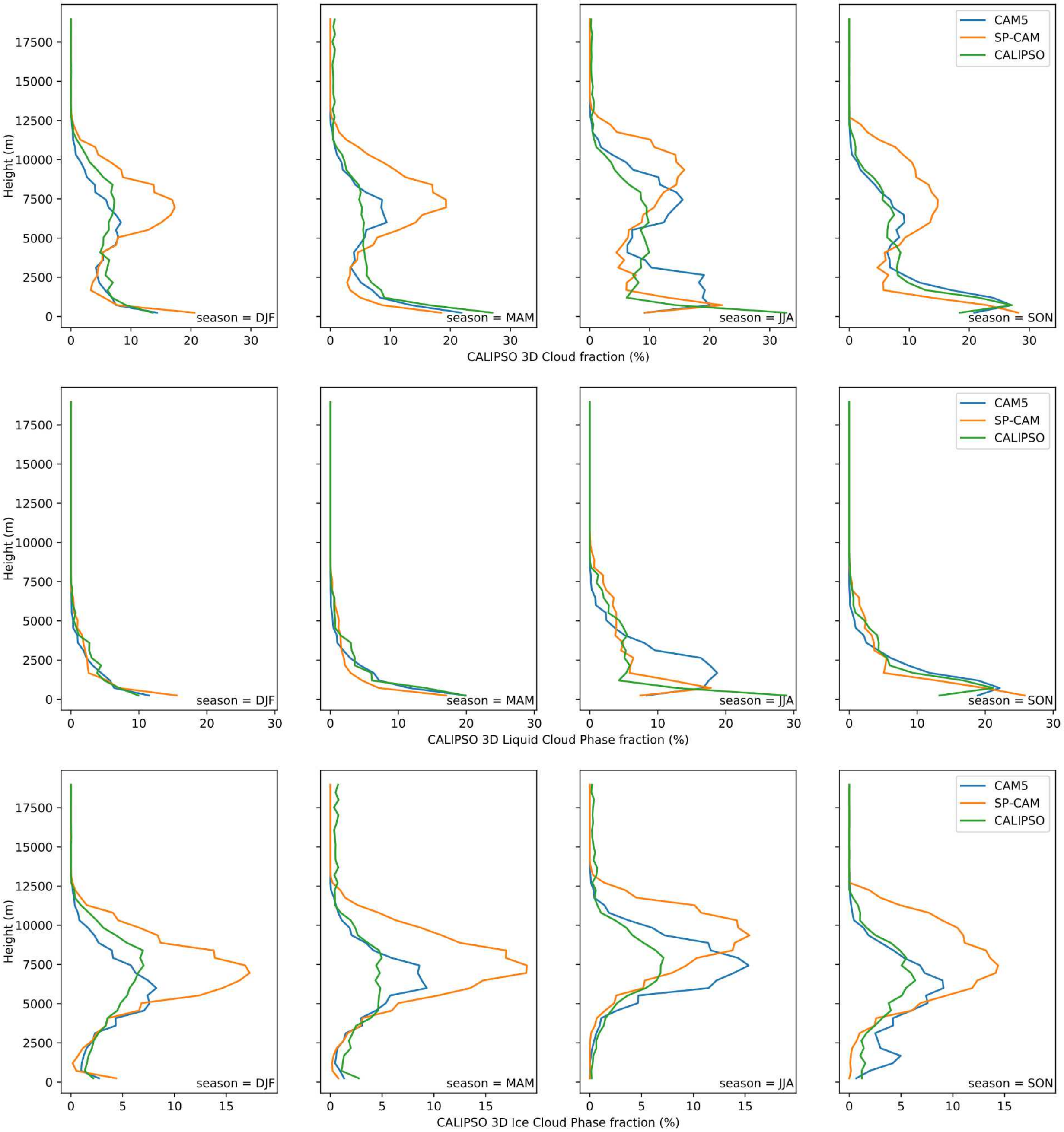

Figure 4.10. Profiles of total (top), liquid (middle) and ice (bottom) cloud fraction by height over the ARM NSA site.

simulated-retrievals by design include the effects of multiple physical properties. In the case of the CALIPSO-simulated cloud fraction profiles, hydrometeors of all types can affect the diagnosis of “cloud”, including cloud liquid, cloud ice, rain, snow, and graupel (which are all predicted microphysical quantities in the SP-CAM microphysics scheme). The simulator comparison has told us that CAM5 and SP-CAM are behaving quite different in the Arctic, but we have not confirmed that the identified biases in “ice cloud” are actually consistent with how the model is treating cloud ice. Focus is now turned to fundamental model variables from these simulations to understand the source of these biases.

Figure 4.11 shows profiles of gridbox mean cloud liquid and cloud ice amount (as a mixing ratio) over the ARM NSA site. The profiles of cloud ice show a persistent upper-level peak in cloud ice water content, consistent with the peak in upper-level ice cloud fraction shown in the comparison against CALIPSO retrievals using the satellite simulator. Gridbox mean cloud ice water content is consistently higher in magnitude in the SP-CAM simulation than in the CAM5 simulation, consistent with the larger amount of ice cloud fraction identified in Figure 4.10. In the fall (SON) season, there is an anomalous peak in low-level cloud ice in the CAM5 simulation that does not appear in the SP-CAM simulation. Comparing Figure 4.11 with Figure 4.10, the low-level peak in cloud ice does appear to correspond to a small peak in low-level ice cloud in the CAM5 simulation, but this feature is much less obvious when comparing the CALIPSO-simulated ice cloud. However, there is no corresponding peak in low-level ice cloud in the CALIPSO retrievals, suggesting that this peak in low-level ice cloud amount in CAM5 is inconsistent with what is actually happening in the fall season at the NSA site.

Cloud liquid is substantially lower in the SP-CAM simulation in the summer (JJA) season where cloud liquid is largest in CAM5, but in the other seasons SP-CAM actually produces *more* cloud liquid than CAM5. The difference in cloud liquid in the summer season is consistent with a much larger amount of liquid cloud identified in CAM5 from the simulator comparison (Figure 4.10). However, the larger amount of cloud liquid in SP-CAM in the other seasons appears to be at odds with a *lower* CALIPSO-simulated liquid cloud fraction in these seasons in Figure 4.10. This result is puzzling, but it is important to recognize that the CALIPSO-simulator comparison does include affects from other hydrometeors, so it is possible that contributions from frozen hydrometeors (snow or graupel) or mis-diagnosis of cloud phase in supercooled conditions could be contributing to this result.

4.2.3 Comparisons of cloud liquid with ARM observations

While the satellite retrievals provide wide spatial coverage, additional retrievals of cloud properties are available from the datastreams collected at the ARM NSA site. These include estimates of liquid water path LWP (the vertically integrated amount of liquid water in the column) obtained from a retrieval using microwave radiometer measurements (MWRRET; Turner et al., 2007). From the microwave radiometer retrieval of liquid water path, we can also calculate an estimated liquid cloud fraction (the fraction of the time in which liquid cloud is present) by calculating the fraction of the time the liquid water path exceeds some threshold value. In this case, we use a threshold value of $LWP_{\text{min}} = 5\ \text{g/m}^2$ to try to exclude some of the measurement noise. The cloud fraction

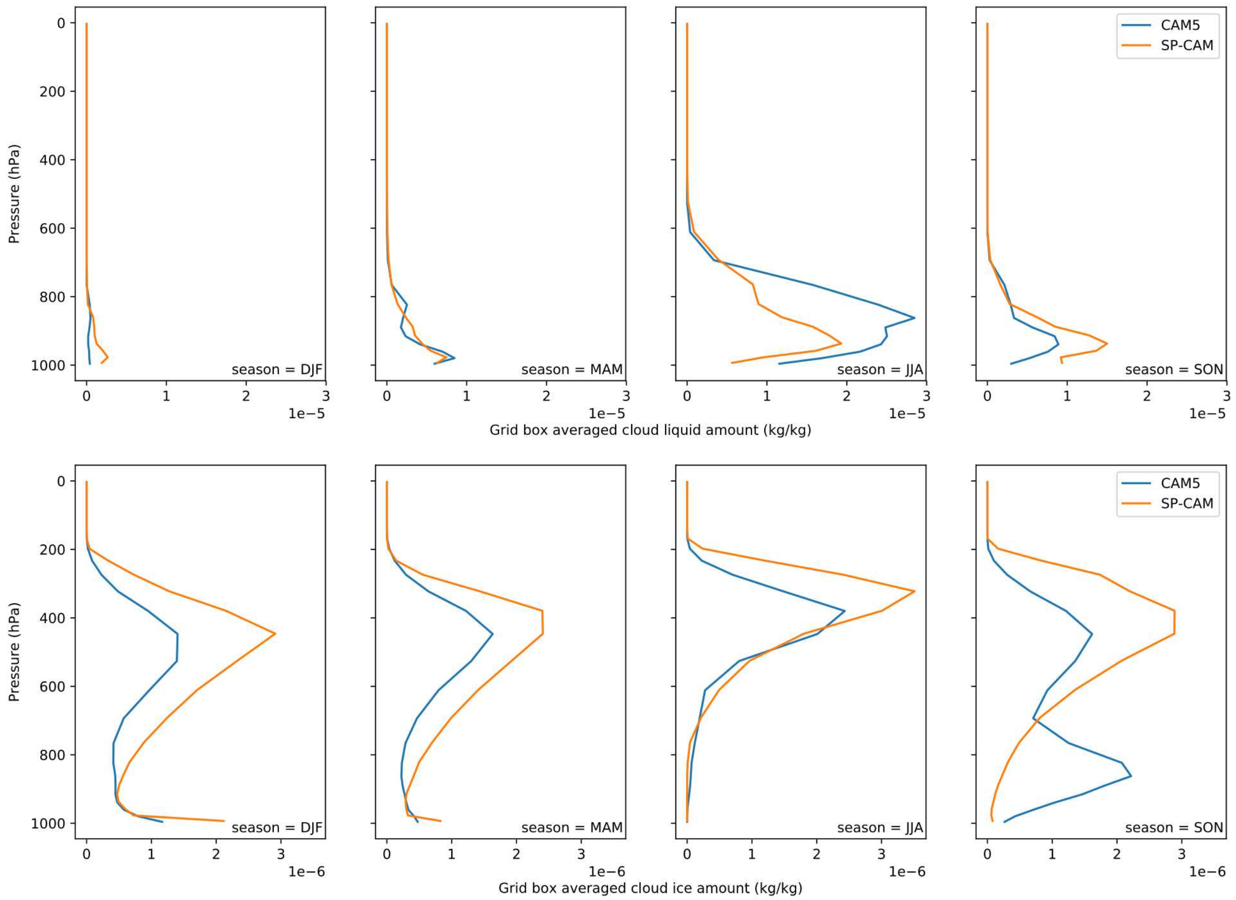

Figure 4.11. Profiles of cloud liquid (top) and cloud ice (bottom) amount over the ARM NSA site.

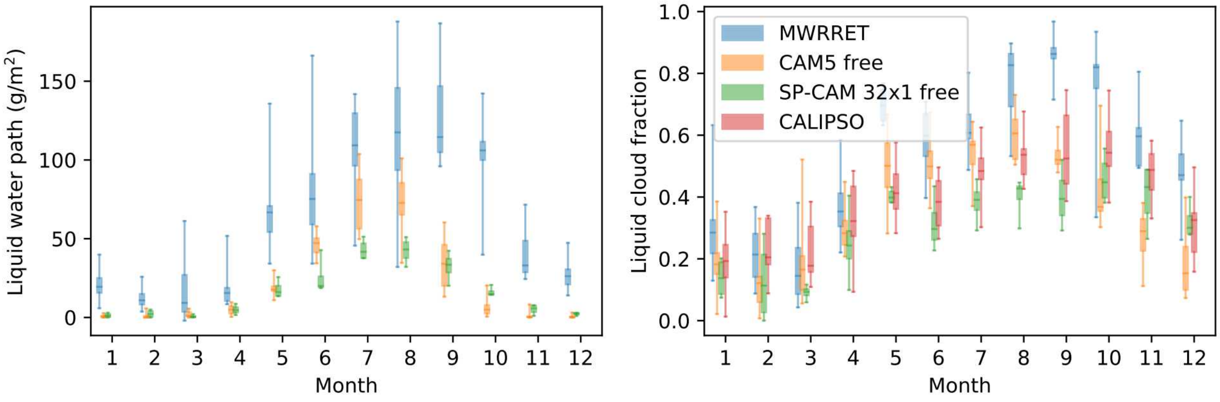

Figure 4.12. Comparisons of climatological mean liquid water path (left) over the ARM NSA site from MWRRET and from CAM5 and SP-CAM simulations, and comparisons of cloud fraction (right) derived from the MWRRET retrieval of liquid water path, CALIPSO-simulated cloud fraction from CAM5 and SP-CAM, and CALIPSO-retrieved cloud fraction over the ARM NSA site. The extent of the whiskers show the range of the monthly means from which the climatologies are calculated, and the extent of the boxes show the interquartile range in the monthly means.

derived from the microwave radiometer data C_{MWR} at each time sample is then set as

$$C_{\mathrm{MWR}} = \begin{cases} 1, \; LWP > LWP_{\mathrm{min}} \\ 0, \; LWP < LWP_{\mathrm{min}} \end{cases}$$

The instantaneous liquid water path and cloud fraction are both re-sampled to monthly-means, and then climatologies are calculated from the monthly means for direct comparison with the model climatologies.

Figure 4.12 shows comparisons of liquid water path and cloud fraction from the MWRRET retrieval of liquid water path with gridbox-mean liquid water path taken from the model gridbox closest to the ARM NSA site from both the CAM5 and SP-CAM simulations (left), and comparisons of (liquid) cloud fraction derived from the MWRRET using the above equation with cloud fraction derived using the CALIPSO simulator within the model simulations. The CALIPSO simulator cloud fraction is used in this case because comparisons using the model-derived cloud fraction is problematic, due to fundamental differences in how this quantity is derived between the CAM5 and SP-CAM simulations. The CALIPSO-retrieved cloud fraction is also shown for comparison.

While the variability in the monthly mean liquid water path from the observations appears large (indicated by the large extent of the boxes and whiskers in the plot, showing a large range in monthly mean values), it is clear that both the CAM5 and SP-CAM simulations consistently underestimate the liquid water path at the NSA site. This is less obvious in the summer season, where the range of the data overlap, but liquid water path is very clearly underestimated from September to January in the model simulations. The liquid water path in the model simulations are similar, except in the summer when CAM5 seems to produce more liquid water than SP-CAM. This is consistent with the Arctic-wide comparison of liquid cloud fraction against CALIPSO-retrievals shown in Figure 4.8, which shows that CAM5 produces more liquid cloud than SP-CAM throughout the Arctic in the summer (JJA) season. The radar/lidar cloud algorithm used in Mioche et al. (2015) had good agreement between CLOUDSAT/CALIPSO and ground-based observations, and future work could investigate these differences.

The comparison of liquid cloud fraction in Figure 4.12 shows that the liquid cloud fraction derived from the MWR retrieval is somewhat larger in the summer months than the CALIPSO retrieval and both of the model simulations. This inconsistency in the two different observed data products suggests that perhaps the threshold of liquid water used to diagnose ‘cloud’ from the MWR retrieval needs further tuning. Liquid cloud fraction estimates are similar between the observations and models from January to April.

The comparison of ice cloud between the model simulations and the CALIPSO retrievals reveals large biases in upper-level ice cloud in the SP-CAM simulation that are not present in the CAM5 simulation, and modest biases in low-level liquid cloud that are seasonally-dependent. In order to investigate the source of these biases, we use two simplified modeling frameworks to explore sensitivities in a more computationally efficient manner than running full global simulations.

4.2.4 Sensitivity of liquid and ice water path to resolution in embedded CRM

The embedded cloud resolving model in the SP-CAM, the System for Atmospheric Modeling (SAM) is able to run as a standalone model if provided with an external forcing (see also Section 4.1). We use this model setup to test the sensitivity of the cloud liquid and cloud ice water paths to model resolution. Because the superparameterization is incredibly expensive to run (approximately 100 times more expensive than CAM5), the embedded CRM is run at very coarse resolution with few columns (32 columns with 4 km grid spacing in the configuration used here). Due to the coarse resolution of the embedded model, we might expect biases due to resolution sensitivities. In order to evaluate this, we perform a series of sensitivity tests with the standalone SAM forced with conditions from observations at the ARM NSA site. We varied three parameters in these sensitivity tests: the number of columns, the grid spacing, and the vertical resolution.

Figure 4.13 shows the result of simultaneously varying the number of columns and the grid spacing so as to keep the domain size of the simulation constant. The vertical grid was kept at 16 levels, sharing the 16 levels below the tropopause from the CAM5 and SP-CAM simulations for consistency. Figure 4.13 shows that the liquid water path actually *decreases* with increasing resolution, which would suggest that increasing the horizontal resolution would only tend to increase the negative bias in cloud liquid shown in the above analysis of SP-CAM. The ice water path appears to be insensitive to changes in horizontal resolution. A similar experiment was also performed in which the number of columns was held fixed while grid spacing was varied from 1

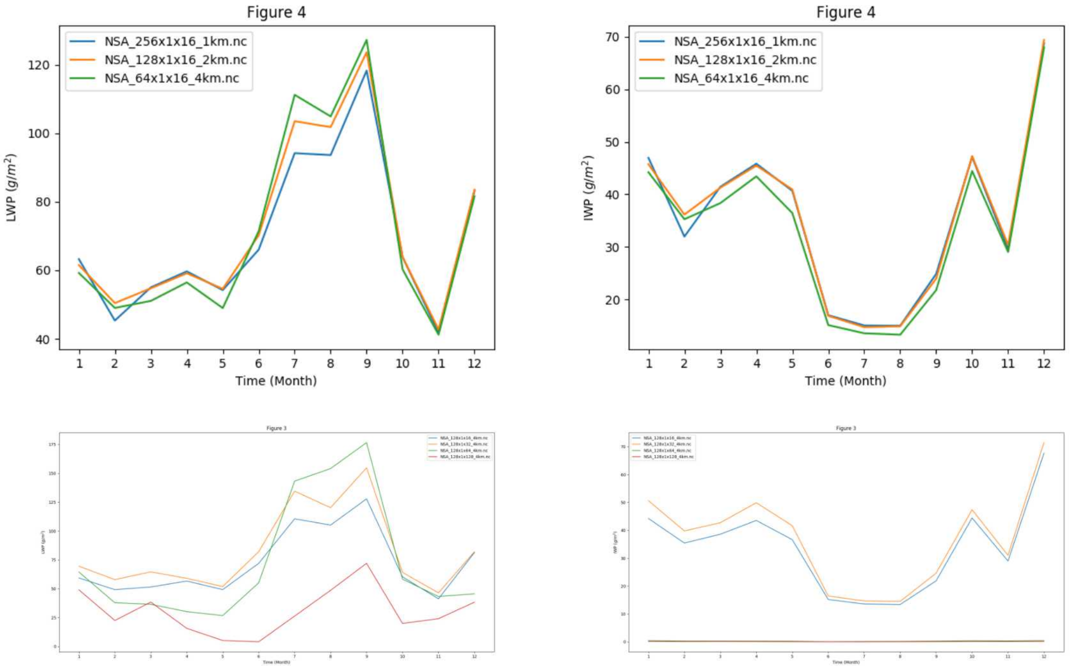

Figure 4.13. Sensitivity of SAM-simulated liquid water path (left) and ice water path (right) to changes in horizontal (top) and vertical resolution (bottom).

km to 4 km. The results of this experiment are nearly identical to those shown in the top row of 4.13 (not shown). Changing the number of columns while holding the grid spacing fixed had no affect, suggesting that the dominant sensitivity to horizontal grid configuration is simply the grid spacing.

The second row of Figure 4.13 shows the impact of varying the vertical resolution. Four different simulations were performed that differed only in the number of vertical levels used. The vertical grids were generated by interpolating between the 16 levels below the tropopause in the CAM5/SP-CAM vertical grid. This created vertical grids with 16 levels (identical to CAM5/SP-CAM), 32 levels, 64 levels, and 128 levels. The data files with the heights are housed in the gitlab repository with names `cam_height_nsa_1x.nc` and `cam_height_nsa_2x.nc`. These simulations were performed with 4 km grid spacing, which was determined to produce the largest liquid water path (from the experiment summarized in the top row of Figure 4.13). The results of varying the vertical resolution are strange. Increasing the vertical resolution tends to increase the liquid water path up to the 64 level simulation, but then liquid water path crashes at 128 levels. Similarly, ice water path increases with the increase in vertical levels from 16 to 32 levels, but then ice water path crashes to nearly zero in the simulations with 64 and 128 vertical levels. The reason for this remains a mystery.

4.2.5 Testing mechanisms for ice overestimation in SP-CAM

Another simplified framework used to understand model biases at a process level is “single-column model” (SCM) experiments. The SCM framework uses the global model code, but only for a single point. This is done by specifying large-scale dynamical forcing for a specific location and time (usually from field experiment campaigns) and then using the full model framework to allow the atmospheric physics (i.e., clouds and convection) to respond to the forced realistic dynamical conditions (winds, relative humidity, temperature). This framework allows isolating the response of the physics from the dynamics. This is an ideal framework for understanding the differences observed between the CAM5 and SP-CAM simulations here, because we want to understand the impact of changing the physics alone (from CAM5 traditionally-parameterized physics to superparameterized), and it allows for testing sensitivity to different parameters at negligible computational cost: these experiments can be run even on a basic Linux desktop, or using a single node on an HPC cluster, even with the superparameterized configuration with a respectable number of columns.

The SCM experiments were performed with the new Super-Parameterized Energy Exascale Earth System Model (SP-E3SM). The Energy Exascale Earth System Model (E3SM) is the Department of Energy’s new earth system model, which was forked from the Community Earth System Model (CESM) and has undergone heavy development since. SP-E3SM was chosen for these experiments as opposed to the SP-CAM codebase used in the global simulations because SCM functionality needed updates only present in the E3SM code, and because analysis and involvement has shifted to E3SM/SP-E3SM. However, the SP-E3SM code still allows running with the CAM5 physics package from CESM, and the SP-E3SM configuration is similar enough to the SP-CAM configuration used in the global experiments that we do not expect this difference to affect the conclusions. The main difference between the SP-CAM and SP-E3SM formulations are a greater number of vertical levels in SP-E3SM (72 vs 30), and a change from a finite volume dynamical core to a spectral element dynamical core.

SCM cases require input forcing derived from field experiments. The Mixed-Phase Arctic Cloud Experiment (MPACE; Verlinde et al., 2007) collected data over the ARM NSA site in Barrow, Alaska. The goal of the experiment was to collect data to study the interactions between microphysics, dynamics, and radiative transfer in mixed-phase clouds (clouds with liquid water at temperatures below freezing). Mixed-phase clouds are notoriously difficult for models to simulate, and we might expect many of the biases we observe in both CAM5 and SP-CAM/SP-E3SM to result from poor representation of the processes important for simulating cloud properties in cold (sub-freezing) conditions. A set of forcing have been derived for an E3SM SCM experiment following Klein et al. (2009). The MPACE forcing recreate conditions that resulted in a persistent single-layer mixed-phase (liquid and ice containing) stratocumulus cloud near Barrow, Alaska.

Three SCM experiments were performed using the MPACE forcing: one with CAM5 (non-superparameterized) physics as a baseline, one with SP-E3SM using the two-moment microphysics scheme (similar to the global experiments), and another SP-E3SM experiment in which the threshold particle size for ice autoconversion is artificially decreased to promote more ice precipitation. Figure 4.15 shows the timeseries of cloud liquid and cloud ice amount over the duration of the ex-

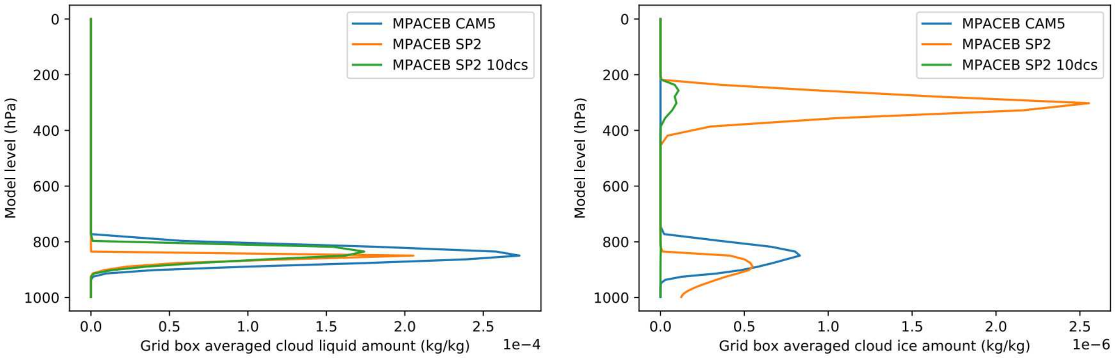

Figure 4.14. Time-averaged cloud liquid (left) and cloud ice (right) concentrations averaged over the duration of MPACE single column model experiments using CAM5, SP-E3SM, and SP-E3SM with adjusted ice autoconversion rate.

periment from each of these three cases, and Figure 4.14 shows time-averages of these quantities.

The time averages shown in Figure 4.14 show that the SP-E3SM simulation is actually producing an upper-level ice cloud layer, while the CAM5 simulation is not. Recall that the MPACE forcing is for an idealized *single*-layer mixed phase stratocumulus cloud, so these conditions should *not* produce an extra upper-level ice cloud layer. Along with the extraneous upper-level ice cloud layer that forms, low-level cloud liquid (and cloud ice) amounts are smaller in the SP-E3SM simulation than in the CAM5 simulation. The excessive cloud ice and the lower amount of low-level cloud liquid are consistent with the Arctic-wide climatological mean results reported above, suggesting that we can learn about the physical mechanisms responsible for this identified model bias in SP-CAM/SP-E3SM from this experiment.

The time-series in Figure 4.15 show that the cloud ice layer forms towards the end of the simulation, and that the low-level mixed-phase layer is generally thinner throughout the simulation in SP-E3SM than in CAM5. We expect the thinner liquid layer to be problematic in general, because CAM5 already tends to underestimate liquid cloud amount in mixed-phase conditions, but the more troubling feature is the upper-level ice cloud that forms in the SP-E3SM simulation.

Figure 4.16 shows the timeseries of relative humidity. The upper-level relative humidity increases throughout the simulation, but relative humidities in the SP-E3SM simulations stop increasing at 100%, while the relative humidity in the CAM5 simulation is able to increase above 100%. The truncation at 100% relative humidity more clear in Figure 4.17, which shows the relative humidity at the end each each simulation. Relative humidity above 100% is called "supersaturation", and these conditions are well-known to occur in the real world. The CAM5 simulation produces supersaturations up to 140% at the end of the simulation, but the SP-E3SM simulations are clearly truncated at 100%. What appears to be happening then, is relative humidity is increasing over the course of the simulation in both the CAM5 and SP-E3SM configurations, but while

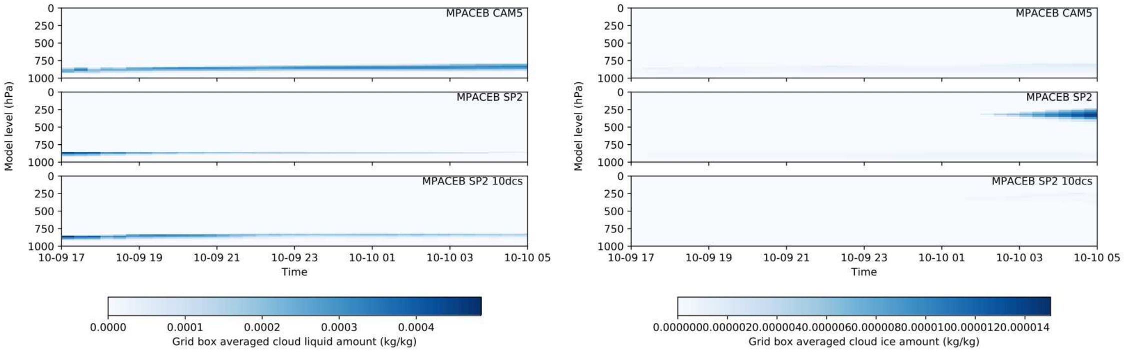

Figure 4.15. Time-series of cloud liquid (left) and cloud ice (right) concentrations for the MPACE single column model experiments using CAM5, SP-E3SM, and SP-E3SM with adjusted ice autoconversion rate.

CAM5 is allowing supersaturation to occur when the relative humidity reaches 100%, SP-E3SM immediately converts any additional water vapor into cloud ice once saturation is reached.

As an initial test to the tuning of the ice microphysics in the SP-E3SM configuration, we adjusted the threshold particle size DCS for autoconversion of ice crystals to form precipitating ice (snow). This forces the model to precipitate more ice. In the experiment shown here, we cut DCS from a value of 125 μm to 10 μm. This is a large change, and other authors have shown that the value of DCS should actually be *increased* to be physically consistent with observations (Zhang et al., 2013, 2014). Nonetheless, decreasing DCS appears to have the desired affect of decreasing the upper-level cloud ice in the SP-E3SM simulation. Figure 4.14 shows that decreasing DCS nearly eliminates the upper-level ice cloud layer, but this also eliminates the lower-level ice concentration associated with the mixed-layer stratocumulus cloud. In fact, most all of the ice ends up precipitating out. Figure 4.16 and Figure 4.17 show that relative humidity is still truncated at 100% in this sensitivity experiment, so supersaturation of ice is still prohibited. Thus, increasing the ice autoconversion (by decreasing the threshold size for autoconversion) decreases the extraneous upper-level ice layer, but for the wrong reason. Interestingly, decreasing DCS has the side benefit of improving the specific humidity and the total water mixing ratio, however, bringing these quantities into better agreement with the CAM5 simulation (Figure 4.17).

4.2.6 Summary of Superparameterization results

The primary goal of this work with the super-parameterized model in the context of this work was to understand whether or not using super-parameterization to explicitly resolve smaller-scale motions than can be resolved in the traditional coarse-resolution GCM would improve the simulation of Arctic clouds. While this project is specifically focused on low-level, liquid-containing clouds, a comprehensive evaluation of cloud properties was performed using both satellite and ground-based

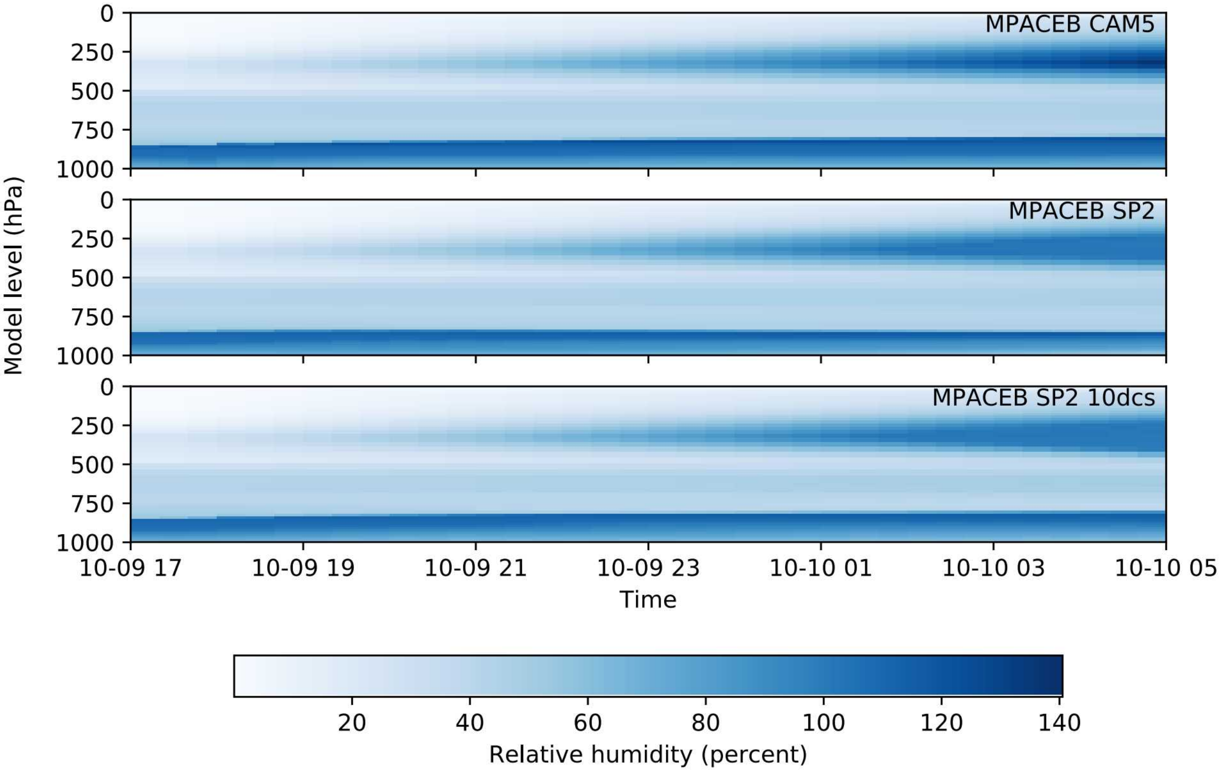

Figure 4.16. Time-series of relative humidity for the MPACE single column model experiments using CAM5, SP-E3SM, and SP-E3SM with adjusted ice autoconversion rate.

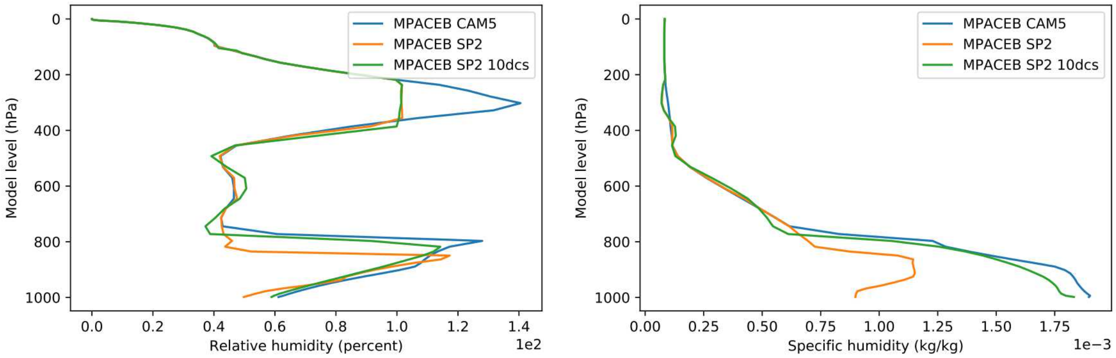

Figure 4.17. Relative and specific humidity at the last time step for the MPACE single column model experiments using CAM5, SP-E3SM, and SP-E3SM with adjusted ice autoconversion rate.

retrievals of cloud properties.

Comparison of CAM5 and SP-CAM simulations with satellite retrievals of cloud properties from CALIPSO revealed unrealistically large amounts of upper-level ice cloud throughout the Arctic in SP-CAM, and an underestimate of low-level liquid cloud in both CAM5 and SP-CAM. A more detailed analysis was performed using data obtained from the ARM North Slope of Alaska facility in Barrow, Alaska, with both ground-based retrievals of liquid water path and subset satellite retrievals from CALIPSO to perform a top-down and bottom-up evaluation of clouds in the two model configurations. The comparison at the ARM NSA revealed similar biases in liquid and ice cloud consistent with those identified Arctic-wide using the satellite retrievals, with a general underestimation of liquid water path, and an overestimation of high-level ice in especially the SP-CAM simulation. From these results, it appears that biases in Arctic clouds simulated by SP-CAM are actually larger than in CAM5.

To understand why biases in Arctic clouds are larger in SP-CAM than in CAM5, sensitivity tests were performed to understand the dependence of the model solution on the resolution of the embedded cloud resolving model, and single column model experiments were performed to understand physical mechanisms for the biases. While the liquid cloud amount did appear somewhat sensitive to both horizontal and vertical resolution, the simulated cloud ice amount was not. The results of the single-column model experiments suggest that SP-CAM/SP-E3SM is unable to produce supersaturated conditions with respect to ice, so that any additional moisture in the atmosphere immediately condenses and freezes into ice once relative humidities of 100% are reached (in below-freezing conditions). Supersaturation does occur in the CAM5 simulation, however, so relative humidities can exceed 100% without the extra moisture being converted immediately into liquid or ice. Artificially modifying the autoconversion of ice crystals to snow tends to mitigate the cloud ice overestimate, but this requires an unphysical value for the threshold size for ice autoconversion, and appears to help for the wrong reason. The larger issue seems to be how the microphysics in SP-E3SM nucleate cloud ice. While the microphysical parameterizations are similar between CAM5 and SP-CAM/SP-E3SM, both being two-moment microphysical schemes, one important difference between the two is the ice nucleation parameterization (which can be thought of as a sub-parameterization of the scheme). Zhang et al. (2014) demonstrate the impact on cirrus clouds of incorporating a different ice nucleation scheme into the Pacific Northwest National Laboratory Multi-scale Modeling Framework (PNNL MMF), which is closely related to the SP-E3SM used here. Zhang et al. (2014) show that cloud ice water path and ice water content are in good agreement with satellite-retrieved estimates of these quantities using the new aerosol-dependent ice nucleation scheme. While incorporating a new ice nucleation scheme in SP-E3SM was well beyond the scope of this work, the biases shown here and the results shown in Zhang et al. (2014) suggest that exploring more realistic ice nucleation schemes would be a fruitful area of further study.

One aspect of the superparameterization project that was abandoned due to lack of resources and confidence with the entire SP-configuration was the use of a Limited Area Superparameterized model. Instead of using the superparameterization over the entire global, it would be only used over an area of interest. Computationally, it was envisioned to be called only in selected ‘ncols’ on the cubed sphere with the SP-region being larger than needed to avoid bad transitions (via M. Taylor).

This was built upon the assumption that superparameterization would provide a better simulation of clouds in the Arctic, but analysis has suggested that is really not the case. Thus, it made little sense to spend the effort to enable turning on and off the superparameterization locally, since even the global configuration does not significantly improve the simulation.

Chapter 5

Conclusions of Project Impact and Accomplishments

This project worked to close the gap between atmospheric in situ measurements of Arctic boundary-layer clouds via sensors on tethered balloon systems and atmospheric models' representation of these clouds by testing four unique model configurations over multiple resolutions. These prevalent clouds play an important role in the Arctic climate, and improving their representation in climate models will inevitably reduce uncertainty in the Arctic?s climate projections which benefits DOE's energy security missions. As predicted, spatial resolution was a key factor in improving simulated cloud amount. Future work in model physics and retrieval algorithms will reduce model bias of cloud phase partitioning.

This research asked the science question, "How is the maintenance of Arctic boundary layer clouds dependent on vertical velocities profiles?" To answer this science question, comprehensive measurements of a realistic Arctic boundary layer cloud system was needed, which is more than the currently implemented radiometric retrievals (yielding uncertainties near 100%). A tethered balloon system was deployed over multiple seasons and years to gather a comprehensive, publicly available data set. The new measurements were compared with existing sources, and high correlation was found between the new and old measurements (i.e., balloon-borne sondes and fiber-optic distributed temperature sensor). The measurements also revealed deficiencies in the existing techniques (i.e., microwave radiometer and ceilometer) as they lacked sensitivity of the newer sensors (i.e., supercooled liquid water sensors); in other words, they failed to detect clouds when clouds were clearly present.

For the first time, atmospheric general circulation model output was compared with more temporally- and spatially-comprehensive CALIPSO satellite space-based and ground-based radiometric measurements (microwave radiometer) over the North Slope of Alaska. A lack of agreement between those two measurements and the model shows much future work is needed to determine what the actual Arctic cloud amount is as no one measurement or model is likely correct. Additionally, the superparameterization model configuration had problematic biases that deemed it not a viable bridge between hydrostatic and non-hydrostatic model resolutions. For the first time, near-continuous Large Eddy Simulations (LES) were performed to simulate in-cloud dynamics during the tethered balloon measurement campaigns. It was found global reanalysis is not viable for model initialization in the Arctic and is unable to reproduce the observed environment if used. Other means to initialize the LES were then used. Work was also begun in testing the robustness of these findings extrapolated to other Arctic sights by comparing climatologies between Barrow and Oliktok.

Research results include enhancement and development of capabilities in the acquisition of atmospheric measurements in harsh environments via unmanned systems and Arctic-domain multiscale modeling abilities. The science community also gains a valid multi-year dataset. Beyond the increased knowledge and insight of how to reduce global model bias of Arctic clouds through complex measurements and numerical modeling, entities using weather forecasting to quantify icing-build-up on aircraft will benefit from this research in the future. By calibrating and understanding high-resolution models from tethered-balloon measurements, future metrics can be derived of supercooled liquid water content that could adversely affect aircraft through contact freezing. The future application of the simulation and measurement datasets are valuable and will be shared with a broader science community through the ARM data repository. New collaborations between the University of Alaska Fairbanks, NOAA/CIRES faculty, and the global modeling community were also made during this project. Finally, this LDRD suceeded in career development for early career and student employees. Eight participants were positively impacted in ways that resulted in securing better positions or promotions. In summary, the project had accomplishments on many levels.

References

Ahrens, C. D., 2006: *Meteorology Today: An Introduction to Weather, Climate, and the Environment*. 8th ed., Brooks Cole.

ARM Decadal Vision Report, 2014: Atmospheric radiation measurement climate research facility decadal vision. Tech. Rep. DOE/SC-ARM-14-029, Department of Energy's Office of Science Atmospheric Radiation Measurement Program.

Bain, M., and J. F. Gayet, 1982: Aircraft measurements of icing in supercooled and water droplet/ice crystal clouds. *Journal of Applied Meteorology*, **21 (5)**, 631–641, URL https://doi.org/10.1175/1520-0450(1982)021⟨0631:AMOIIS⟩2.0.CO;2.

Barnes, S. L., 1964: A technique for maximizing details in numerical weather map analysis. *Journal of Applied Meteorology*, **3 (4)**, 396–409, doi:10.1175/1520-0450(1964)003⟨0396:ATFMDI⟩2.0.CO;2, URL https://doi.org/10.1175/1520-0450(1964)003⟨0396:ATFMDI⟩2.0.CO;2, https://doi.org/10.1175/1520-0450(1964)003⟨0396:ATFMDI⟩2.0.CO;2.

Benedict, J. J., and D. A. Randall, 2009: Structure of the madden–julian oscillation in the superparameterized cam. *Journal of the Atmospheric Sciences*, **66 (11)**, 3277–3296.

Bodas-Salcedo, A., and Coauthors, 2011: COSP: Satellite simulation software for model assessment. *Bull. Amer. Meteor. Soc.*, **92 (8)**, doi:10.1175/2011BAMS2856.1.

Bolgnar, D., 2015: Personal communication.

Bosler, P. A., E. L. Roesler, M. A. Taylor, and M. R. Mundt, 2016: Stride search: a general algorithm for storm detection in high-resolution climate data. *Geoscientific Model Development*, **9 (4)**, 1383–1398, doi:10.5194/gmd-9-1383-2016, URL https://www.geosci-model-dev.net/9/1383/2016/.

Brient, F., and T. Schneider, 2016: Constraints on climate sensitivity from space-based measurements of low-cloud reflection. *Journal of Climate*, **29 (16)**, 5821–5835, doi:10.1175/JCLI-D-15-0897.1, URL http://dx.doi.org/10.1175/JCLI-D-15-0897.1, http://dx.doi.org/10.1175/JCLI-D-15-0897.1.

Bromwich, D. H., A. B. Wilson, L.-S. Bai, G. W. K. Moore, and P. Bauer, 2016: A comparison of the regional arctic system reanalysis and the global era-interim reanalysis for the arctic. *Quarterly Journal of the Royal Meteorological Society*, **142 (695)**, 644–658, doi:10.1002/qj.2527, URL http://dx.doi.org/10.1002/qj.2527.

Carton, J. A., Y. Ding, and K. R. Arrigo, 2015: The seasonal cycle of the arctic ocean under climate change. *Geophysical Research Letters*, **42 (18)**, 7681–7686, doi:10.1002/2015GL064514, URL https://agupubs.onlinelibrary.wiley.com/doi/abs/10.1002/2015GL064514, https://agupubs.onlinelibrary.wiley.com/doi/pdf/10.1002/2015GL064514.

Cesana, G., and H. Chepfer, 2013: Evaluation of the cloud thermodynamic phase in a climate model using calipso-goccp. *Journal of Geophysical Research: Atmospheres*, **118 (14)**, 7922–7937, doi:10.1002/jgrd.50376, URL https://agupubs.onlinelibrary.wiley.com/doi/abs/10.1002/jgrd.50376, https://agupubs.onlinelibrary.wiley.com/doi/pdf/10.1002/jgrd.50376.

Cheng, A., and K.-M. Xu, 2011: Improved low-cloud simulation from a multiscale modeling framework with a third-order turbulence closure in its cloud-resolving model component. *Journal of Geophysical Research: Atmospheres*, **116 (D14)**, doi:10.1029/2010JD015362.

Cheng, A., and K.-M. Xu, 2013: Evaluating low-cloud simulation from an upgraded multiscale modeling framework model. part iii: Tropical and subtropical cloud transitions over the northern pacific. *Journal of Climate*, **26 (16)**, 5761–5781, doi:10.1175/JCLI-D-12-00650.1.

Chepfer, H., S. Bony, D. Winker, G. Cesana, J. L. Dufresne, P. Minnis, C. J. Stubenrauch, and S. Zeng, 2010: The gcm-oriented calipso cloud product (calipso-goccp). *Journal of Geophysical Research: Atmospheres*, **115 (D4)**, doi:10.1029/2009JD012251, URL https://agupubs.onlinelibrary.wiley.com/doi/abs/10.1029/2009JD012251, https://agupubs.onlinelibrary.wiley.com/doi/pdf/10.1029/2009JD012251.

Chepfer, H., S. Bony, D. Winker, M. Chiriaco, J.-L. Dufresne, and G. Sèze, 2008: Use of CALIPSO lidar observations to evaluate the cloudiness simulated by a climate model. *Geophysical Research Letters*, **35 (15)**, doi:10.1029/2008GL034207.

Crawford, A., and M. Serreze, 2014: A new look at the summer arctic frontal zone. *Journal of Climate*, **28 (2)**, 737–754, URL https://doi.org/10.1175/JCLI-D-14-00447.1.

de Jong, S. A. P., J. D. Slingerland, and N. C. van de Giesen, 2015: Fiber optic distributed temperature sensing for the determination of air temperature. *Atmospheric Measurement Techniques*, **8 (1)**, 335–339, doi:10.5194/amt-8-335-2015, URL https://www.atmos-meas-tech.net/8/335/2015/.

Deardorff, J. W., 1980: Stratocumulus-capped mixed layers derived from a 3-Dimensional model. *Boundary-Layer Meteorology*, **18 (4)**, 495–527.

Dee, D. P., and Coauthors, 2011: The era-interim reanalysis: configuration and performance of the data assimilation system. *Quarterly Journal of the Royal Meteorological Society*, **137 (656)**, 553–597, URL https://doi.org/10.1002/qj.828.

DeMott, C. A., D. A. Randall, and M. Khairoutdinov, 2007: Convective precipitation variability as a tool for general circulation model analysis. *Journal of climate*, **20 (1)**, 91–112, doi:10.1175/JCLI3991.1.

Deser, C., J. Walsh, and M. Timlin, 2000: Arctic sea ice variability in the context of recent atmospheric circulation trends. *Journal of Climate*, **13 (3)**, 617–633.

Dexheimer, D., 2018: Tethered balloon system (tbs) instrument handbook. Tech. rep.

Fang, Z., and J. M. Wallace, 1994: Arctic sea ice variability on a timescale of weeks and its relation to atmospheric forcing. *Journal of Climate*, **7 (12)**, 1897–1914, URL https://doi.org/10.1175/1520-0442(1994)007⟨1897:ASIVOA⟩2.0.CO;2.

Forster, P., and Coauthors, 2007: Changes in atmospheric constituents and in radiative forcing. *Climate Change 2007: The Physical Science Basis. Contribution of Working Group I to the Fourth Assessment Report of the Intergovernmental Panel on Climate Change*, S. Solomon, D. Qin, M. Manning, Z. Chen, M. Marquis, K. Averyt, M. Tignor, and H. Miller, Eds., Cambridge University, Cambridge, United Kingdom and New York, NY, USA, viii, 996 p.

Gent, P. R., and Coauthors, 2011: The community climate system model version 4. *Journal of Climate*, **24 (19)**, 4973–4991, URL https://doi.org/10.1175/2011JCLI4083.1.

Grabowski, W. W., 2001: Coupling cloud processes with the large-scale dynamics using the cloud-resolving convection parameterization (crcp). *Journal of the Atmospheric Sciences*, **58 (9)**, 978–997.

Guba, O., M. A. Taylor, P. A. Ullrich, J. R. Overfelt, and M. N. Levy, 2014: The spectral element method (sem) on variable-resolution grids: evaluating grid sensitivity and resolution-aware numerical viscosity. *Geoscientific Model Development*, **7 (6)**, 2803–2816.

Gultepe, I., and G. A. Isaac, 1997: Liquid water content and temperature relationship from aircraft observations and its applicability to gcms. *Journal of Climate*, **10 (3)**, 446–452, URL https://doi.org/10.1175/1520-0442(1997)010⟨0446:LWCATR⟩2.0.CO;2.

Haynes, J. M., R. T. Marchand, Z. Luo, A. Bodas-Salcedo, and G. L. Stephens, 2007: A multipurpose radar simulation package: Quickbeam. *Bulletin of the American Meteorological Society*, **88 (11)**, 1723–1727, doi:10.1175/BAMS-88-11-1723.

Hill, G. E., 1994: Analysis of supercooled liquid water measurements using microwave radiometer and vibrating wire devices. *Journal of Atmospheric and Oceanic Technology*, **11 (5)**, 1242–1252, URL https://doi.org/10.1175/1520-0426(1994)011⟨1242:AOSLWM⟩2.0.CO;2.

Hillman, B. R., R. T. Marchand, and T. P. Ackerman, 2018: Sensitivities of simulated satellite views of clouds to subgrid-scale overlap and condensate heterogeneity. *Journal of Geophysical Research: Atmospheres*, **123 (14)**, 7506–7529, doi:10.1029/2017JD027680, URL https://agupubs.onlinelibrary.wiley.com/doi/abs/10.1029/2017JD027680, https://agupubs.onlinelibrary.wiley.com/doi/pdf/10.1029/2017JD027680.

Hughes, M., and J. J. Cassano, 2015: The climatological distribution of extreme arctic winds and implications for ocean and sea ice processes. *Journal of Geophysical Research: Atmospheres*, **120 (15)**, 7358–7377, doi:10.1002/2015JD023189, URL https://agupubs.onlinelibrary.wiley.com/doi/abs/10.1002/2015JD023189, https://agupubs.onlinelibrary.wiley.com/doi/pdf/10.1002/2015JD023189.

Hurrell, J. W., 1995: Decadal trends in the north atlantic oscillation: Regional temperatures and precipitation. *Science*, **269 (5224)**, 676–679, URL http://www.jstor.org/stable/2888966.

Hurrell, J. W., 1996: Influence of variations in extratropical wintertime teleconnections on northern hemisphere temperature. *Geophysical Research Letters*, **23 (6)**, 665–668, URL https://doi.org/10.1029/96GL00459.

Jensen, M. P., and T. Toto, 2016: Interpolated sounding and gridded sounding value-added products. Tech. Rep. BNL-112644-2016, Brookhave National Laboratory.

Jin-Qing, Z., L. Wei-Jing, and R. Hong-Li, 2013: Representation of the arctic oscillation in the cmip5 models. *Advances in Climate Change Research*, **4 (4)**, 242 – 249, doi:https://doi.org/10.3724/SP.J.1248.2013.242, URL http://www.sciencedirect.com/science/article/pii/S1674927813500360.

Kalnay, E., and Coauthors, 1996: The NCEP/NCAR 40-year reanalysis project. *Bulletin of the American Meteorological Society*, **77 (3)**, 437–471.

Kay, J. E., L. Bourdages, N. B. Miller, A. Morrison, V. Yettella, H. Chepfer, and B. Eaton, 2016: Evaluating and improving cloud phase in the community atmosphere model version 5 using spaceborne lidar observations. *Journal of Geophysical Research: Atmospheres*, **121 (8)**, 4162–4176.

Kay, J. E., T. L'Ecuyer, A. Gettelman, G. Stephens, and C. O'Dell, 2008: The contribution of cloud and radiation anomalies to the 2007 Arctic sea ice extent minimum. *Geophysical Research Letters*, **35 (8)**.

Kay, J. E., and Coauthors, 2012: Exposing global cloud biases in the Community Atmosphere Model (CAM) using satellite observations and their corresponding instrument simulators. *J. Climate*, **25**, 5190–5207, doi:{10.1175/JCLI-D-11-00469.1}.

Keller, C. A., H. Huwald, M. K. Vollmer, A. Wenger, M. Hill, M. B. Parlange, and S. Reimann, 2011: Fiber optic distributed temperature sensing for the determination of the nocturnal atmospheric boundary layer height. *Atmospheric Measurement Techniques*, **4 (2)**, 143–149, doi:10.5194/amt-4-143-2011, URL https://www.atmos-meas-tech.net/4/143/2011/.

Khairoutdinov, M., C. DeMott, and D. Randall, 2008: Evaluation of the simulated interannual and subseasonal variability in an amip-style simulation using the csu multiscale modeling framework. *Journal of Climate*, **21 (3)**, 413–431, doi:10.1175/2007JCLI1630.1.

Khairoutdinov, M., D. Randall, and C. DeMott, 2005: Simulations of the atmospheric general circulation using a cloud-resolving model as a superparameterization of physical processes. *Journal of the Atmospheric Sciences*, **62 (7)**, 2136–2154, doi:10.1175/JAS3453.1.

Khairoutdinov, M. F., and D. A. Randall, 2001: A cloud-resolving model as a cloud parameterization in the NCAR Community Climate System Model: Preliminary results. *Geophys. Res. Lett.*, **28**, 3617–3620.

Khairoutdinov, M. F., and D. A. Randall, 2003: Cloud resolving modeling of the ARM summer 1997 IOP: Model formulation, results, uncertainties, and sensitivities. *Journal of the Atmospheric Sciences*, **60 (4)**, 607–625.

King, M. C., J. Bognar, and D. Guest, 2016: *Vibrating-Wire, Supercooled Liquid Water Content Sensor Calibration and Characterization Progress*. American Institute of Aeronautics and Astronautics, URL https://doi.org/10.2514/6.2016-4055.

Klein, S. A., and C. Jakob, 1999: Validation and sensitivities of frontal clouds simulated by the ECMWF model. *Monthly Weather Review*, **127 (10)**, 2514–2531, doi:10.1175/1520-0493(1999) 127$\langle$2514:VASOFC$\rangle$2.0.CO;2.

Klein, S. A., Y. Zhang, M. D. Zelinka, R. Pincus, J. Boyle, and P. J. Gleckler, 2013: Are climate model simulations of clouds improving? an evaluation using the ISCCP simulator. *Journal of Geophysical Research*, **118 (3)**, 1329–1342, doi:doi:10.1002/jgrd.50141.

Klein, S. A., and Coauthors, 2009: Intercomparison of model simulations of mixed-phase clouds observed during the ARM Mixed-Phase Arctic Cloud Experiment I: Single-layer cloud. *Quarterly Journal of the Royal Meteorological Society*, **135 (641)**, 979–1002.

Kooperman, G. J., M. S. Pritchard, M. A. Burt, M. D. Branson, and D. A. Randall, 2016: Robust effects of cloud superparameterization on simulated daily rainfall intensity statistics across multiple versions of the community earth system model. *Journal of Advances in Modeling Earth Systems*, **8 (1)**, 140–165, doi:10.1002/2015MS000574.

Lin, W. Y., and M. H. Zhang, 2004: Evaluation of clouds and their radiative effects simulated by the NCAR Community Atmospheric Model against satellite observations. *Journal of Climate*, **17 (17)**, 3302–3318, doi:10.1175/1520-0442(2004)017$\langle$3302:EOCATR$\rangle$2.0.CO;2.

Lindsay, R., M. Wensnahan, A. Schweiger, and J. Zhang, 2014: Evaluation of seven different atmospheric reanalysis products in the arctic. *Journal of Climate*, **27 (7)**, 2588–2606, doi:10.1175/JCLI-D-13-00014.1, URL https://doi.org/10.1175/JCLI-D-13-00014.1, https://doi.org/10.1175/JCLI-D-13-00014.1.

Liu, C., and E. A. Barnes, 2015: Extreme moisture transport into the arctic linked to rossby wave breaking. *Journal of Geophysical Research: Atmospheres*, **120 (9)**, 3774–3788, doi:10.1002/2014JD022796, URL https://agupubs.onlinelibrary.wiley.com/doi/abs/10.1002/2014JD022796, https://agupubs.onlinelibrary.wiley.com/doi/pdf/10.1002/2014JD022796.

Liu, Y., M. D. Shupe, Z. Wang, and G. Mace, 2017: Cloud vertical distribution from combined surface and space radar–lidar observations at two arctic atmospheric observatories. *Atmospheric Chemistry and Physics*, **17 (9)**, 5973–5989, doi:10.5194/acp-17-5973-2017, URL https://www.atmos-chem-phys.net/17/5973/2017/.

Lozowski, E. P., J. R. Stallabrass, and P. F. Hearty, 1983: The icing of an unheated, nonrotating cylinder. part i: A simulation model. *Journal of Climate and Applied Meteorology*, **22 (12)**, 2053–2062, URL https://doi.org/10.1175/1520-0450(1983)022$\langle$2053:TIOAUN$\rangle$2.0.CO;2.

Marchand, R., and T. Ackerman, 2010: An analysis of cloud cover in multiscale modeling framework global climate model simulations using 4 and 1 km horizontal grids. *Journal of Geophysical Research*, **115**, doi:10.1029/2009JD013423.

Mesquita, M. D. S., D. E. Atkinson, and K. I. Hodges, 2010: Characteristics and variability of storm tracks in the north pacific, bering sea, and alaska. *Journal of Climate*, **23 (2)**, 294–311.

Mioche, G., O. Jourdan, M. Ceccaldi, and J. Delanoë, 2015: Variability of mixed-phase clouds in the arctic with a focus on the svalbard region: a study based on spaceborne active remote sensing. *Atmospheric Chemistry and Physics*, **15 (5)**, 2445–2461, doi:10.5194/acp-15-2445-2015, URL https://www.atmos-chem-phys.net/15/2445/2015/.

Morrison, H., J. A. Curry, and V. I. Khvorostyanov, 2005: A new double-moment microphysics parameterization for application in cloud and climate models. Part I: Description. *Journal of the Atmospheric Sciences*, **62 (6)**, 1665–1677.

Morrison, H., G. de Boer, G. Feingold, J. Harrington, M. D. Shupe, and K. Sulia, 2012: Resilience of persistent arctic mixed-phase clouds. *Nature Geoscience*, **5 (1)**, 11–17.

Neale, R., and Coauthors, 2012: Description of the NCAR Community Atmosphere Model (CAM 5.0). Tech. Rep. NCAR/TN-486+STR, NCAR.

Parishani, H., M. S. Pritchard, C. S. Bretherton, M. C. Wyant, and M. Khairoutdinov, 2017: Toward low cloud-permitting cloud superparameterization with explicit boundary layer turbulence. *Journal of Advances in Modeling Earth Systems*, doi:10.1002/2017MS000968.

Pincus, R., S. Platnick, S. A. Ackerman, R. S. Hemler, and R. J. P. Hofmann, 2012: Reconciling simulated and observed views of clouds: MODIS, ISCCP, and and the limits of instrument simulators. *Journal of Climate*, **25**, 4699–4720, doi:10.1175/JCLI-D-11-00267.1.

Pritchard, M. S., M. W. Moncrieff, and R. C. Somerville, 2011: Orogenic propagating precipitation systems over the united states in a global climate model with embedded explicit convection. *Journal of the Atmospheric Sciences*, **68 (8)**, 1821–1840, doi:10.1175/2011JAS3699.1.

Pritchard, M. S., and R. C. Somerville, 2009a: Assessing the diurnal cycle of precipitation in a multi-scale climate model. *Journal of Advances in Modeling Earth Systems*, **1 (4)**, doi:10.3894/JAMES.2009.1.12.

Pritchard, M. S., and R. C. Somerville, 2009b: Empirical orthogonal function analysis of the diurnal cycle of precipitation in a multi-scale climate model. *Geophysical Research Letters*, **36 (5)**, doi:10.1029/2008GL036964.

Randall, D., M. Khairoutdinov, A. Arakawa, and W. Grabowski, 2003: Breaking the cloud parameterization deadlock. *Bull. Amer. Meteor. Soc.*, **84 (11)**, 1547–1564, doi:10.1175/BAMS-84-11-1547.

Randall, D. A., 2013: Beyond deadlock. *Geophysical Research Letters*, **40 (22)**, 5970–5976.

Reed, R. J., and B. A. Kunkel, 1960: The arctic circulation in summer. *Journal of Meteorology*, **17 (5)**, 489–506, URL https://doi.org/10.1175/1520-0469(1960)017⟨0489:TACIS⟩2.0.CO;2.

Reynolds, R. W., T. M. Smith, C. Liu, D. B. Chelton, K. S. Casey, and M. G. Schlax, 2007: Daily high-resolution-blended analyses for sea surface temperature. *Journal of Climate*, **20 (22)**, 5473–5496, URL ⟨GotoISI⟩://WOS:000251236900001.

Roesler, E. L., D. Dexheimer, C. Longbottom, F. Helsel, M. Apple, B. Hillman, J. Hardesty, and M. Ivey, 2018: Aerial assessment of liquid in clouds at oliktok field campaign report. Tech. rep.

Schneider, T., J. Teixeira, C. S. Bretherton, F. Brient, K. G. Pressel, C. Schar, and A. P. Siebesma, 2017: Climate goals and computing the future of clouds. *Nature Clim. Change*, **7 (1)**, 3–5, URL http://dx.doi.org/10.1038/nclimate3190.

Serke, D., and Coauthors, 2014: Supercooled liquid water content profiling case studies with a new vibrating wire sonde compared to a ground-based microwave radiometer. *Atmospheric Research*, **149**, 77 – 87, doi:https://doi.org/10.1016/j.atmosres.2014.05.026, URL http://www.sciencedirect.com/science/article/pii/S016980951400235X.

Serreze, M. C., A. H. Lynch, and M. P. Clark, 2001: The arctic frontal zone as seen in the NCEP–NCAR reanalysis. *Journal of Climate*, **14 (7)**, 1550–1567, URL https://doi.org/10.1175/1520-0442(2001)014⟨1550:TAFZAS⟩2.0.CO;2.

Tao, W. K., and Coauthors, 2009: A multiscale modeling system developments, applications, and critical issues. *Bulletin of the American Meteorological Society*, **90 (4)**.

Thomas, C. K., A. M. Kennedy, J. S. Selker, A. Moretti, M. H. Schroth, A. R. Smoot, N. B. Tufillaro, and M. J. Zeeman, 2012: High-resolution fibre-optic temperature sensing: A new tool to study the two-dimensional structure of atmospheric surface-layer flow. *Boundary-Layer Meteorology*, **142 (2)**, 177–192, URL https://doi.org/10.1007/s10546-011-9672-7.

Thompson, D. W. J., and J. M. Wallace, 1998: The arctic oscillation signature in the wintertime geopotential height and temperature fields. *Geophysical Research Letters*, **25 (9)**, 1297–1300, URL https://doi.org/10.1029/98GL00950.

Tompkins, A. M., K. Gierens, and G. Rädel, 2017: Ice supersaturation in the ECMWF integrated forecast system. *Quarterly Journal of the Royal Meteorological Society*, **133 (622)**, 53–63, doi:10.1002/qj.14, URL https://rmets.onlinelibrary.wiley.com/doi/abs/10.1002/qj.14, https://rmets.onlinelibrary.wiley.com/doi/pdf/10.1002/qj.14.

Trenberth, K., and Coauthors, 2007: Observations: Surface and atmospheric climate change. *Climate Change 2007: The Physical Science Basis. Contribution of Working Group I to the Fourth Assessment Report of the Intergovernmental Panel on Climate Change*, S. Solomon, D. Qin, M. Manning, Z. Chen, M. Marquis, K. Averyt, M. Tignor, and H. Miller, Eds., Cambridge University Press, Cambridge, United Kingdom and New York, NY, USA.

Turner, D. D., S. A. Clough, J. C. Liljegren, E. E. Clothiaux, K. E. Cady-Pereira, and K. L. Gaustad, 2007: Retrieving liquid wat0er path and precipitable water vapor from the atmospheric radiation measurement (arm) microwave radiometers. *IEEE Transactions on Geoscience and Remote Sensing*, **45 (11)**, 3680–3690, doi:10.1109/TGRS.2007.903703.

Vavrus, S. J., 2013: Extreme arctic cyclones in cmip5 historical simulations. *Geophysical Research Letters*, **40 (23)**, 6208–6212, URL https://doi.org/10.1002/2013GL058161.

Verlinde, J., and Coauthors, 2007: The mixed-phase arctic cloud experiment. *Bulletin of the American Meteorological Society*, **88 (2)**, 205–222, doi:10.1175/BAMS-88-2-205, URL https://doi.org/10.1175/BAMS-88-2-205, https://doi.org/10.1175/BAMS-88-2-205.

Walsh, J. E., and J. E. Sater, 1981: Monthly and seasonal variability in the ocean-ice-atmosphere systems of the north pacific and the north atlantic. *Journal of Geophysical Research: Oceans*, **86 (C8)**, 7425–7445, URL https://doi.org/10.1029/JC086iC08p07425.

Wang, M., J. E. Overland, D. B. Percival, and H. O. Mofjeld, 2006: Change in the arctic influence on bering sea climate during the twentieth century. *International Journal of Climatology*, **26 (4)**, 531–539, doi:10.1002/joc.1278, URL https://rmets.onlinelibrary.wiley.com/doi/abs/10.1002/joc.1278, https://rmets.onlinelibrary.wiley.com/doi/pdf/10.1002/joc.1278.

Webb, M., C. Senior, S. Bony, and J.-J. Morcrette, 2001: Combining ERBE and ISCCP data to assess clouds in the Hadley Centre, ECMWF and LMD atmospheric climate models. *Climate Dynamics*, **17 (12)**, 905–922, doi:10.1007/s003820100157.

Webb, M. J., and Coauthors, 2017: The Cloud Feedback Model Intercomparison Project (CFMIP) contribution to CMIP6. *Geoscientific Model Development*, **10 (1)**, 359–384, doi:10.5194/gmd-10-359-2017, URL https://www.geosci-model-dev.net/10/359/2017/.

Wyant, M. C., C. S. Bretherton, J. T. Bacmeister, J. T. Kiehl, I. M. Held, M. Zhao, S. A. Klein, and B. J. Soden, 2006: A comparison of low-latitude cloud properties and their response to climate change in three agcms sorted into regimes using mid-tropospheric vertical velocity. *Climate Dynamics*, **27 (2-3)**, 261–279.

Xie, S., S. A. Klein, J. J. Yio, A. C. M. Beljaars, C. N. Long, and M. Zhang, 2006: An assessment of ecmwf analyses and model forecasts over the north slope of alaska using observations from the arm mixed-phase arctic cloud experiment. *Journal of Geophysical Research: Atmospheres*, **111 (D5)**, n/a–n/a, doi:10.1029/2005JD006509, URL http://dx.doi.org/10.1029/2005JD006509, d05107.

Zarzycki, C. M., and C. Jablonowski, 2014: A multidecadal simulation of atlantic tropical cyclones using a variable-resolution global atmospheric general circulation model. *Journal of Advances in Modeling Earth Systems*, **6 (3)**, 805–828.

Zhang, C., M. Wang, H. Morrison, R. C. J. Somerville, K. Zhang, X. Liu, and J.-L. F. Li, 2014: Investigating ice nucleation in cirrus clouds with an aerosol-enabled multiscale modeling framework. *Journal of Advances in Modeling Earth Systems*, **6 (4)**, 998–1015, doi:10.1002/2014MS000343, URL https://agupubs.onlinelibrary.wiley.com/doi/abs/10.1002/2014MS000343, https://agupubs.onlinelibrary.wiley.com/doi/pdf/10.1002/2014MS000343.

Zhang, K., X. Liu, M. Wang, J. M. Comstock, D. L. Mitchell, S. Mishra, and G. G. Mace, 2013: Evaluating and constraining ice cloud parameterizations in cam5 using aircraft measurements from the sparticus campaign. *Atmospheric Chemistry and Physics*, **13 (9)**, 4963–4982, doi:10.5194/acp-13-4963-2013, URL https://www.atmos-chem-phys.net/13/4963/2013/.

Zhang, M., and Coauthors, 2005: Comparing clouds and their seasonal variations in 10 atmospheric general circulation models with satellite measurements. *Journal of Geophysical Research*, **110 (D15)**, doi:10.1029/2004JD005021.

Zhang, M. H., and J. L. Lin, 1997: Constrained variational analysis of sounding data based on column-integrated budgets of mass, heat, moisture, and momentum: Approach and application to ARM measurements. *Journal of the Atmospheric Sciences*, **54 (11)**, 1503–1524.

Appendix A

Improving the Workflow with Large Eddy Simulations over Barrow and Oliktok (North Slope of Alaska)

A summary of work performed during undergraduate and graduate research of Matthew McChesney

A.1 Appendix Overview

This project involved using a Large Eddy Simulation with data from the ARM data repository on the North Slope of Alaska to be used as input. Work involved simplifying the steps in running the Large Eddy Simulation, creating a way to automatically obtain data from the ARM data repository, compare changes in the simulation that arose from using different processor layouts on a high-performance computer, and compare how different domain sizes can effect the resolution of the cloud. This work supported the project goals of understanding how different resolutions in numerical models can affect clouds.

A.2 Effects of Using Different Compilers

The large eddy simulation program used for this work is named SAM (System for Atmospheric Modeling). More information about SAM is given in Chapter 4.1. An earlier version was first used (SAM6.10.8), but the project updated to SAM6.10.10. Permission was received from Marat Khairoutdinov to use SAM. On the High Performance Computing machines, much was learned on loading modules, making paths visible to the computer, and editing makefiles. Table A.1 lists the machine names, compiler versions, and processes per node on the two high performance computers used for this work. Compiling with different compilers would sometimes give different cloud field amounts, so the decision was made to use SAM6.10.10 and the same Intel compiler. For example, in using the Intel 1.6 compiler, a confusing and non-graceful exit error was given (Figure A.1). Switching to Intel 1.8 compiler gave more details about the error, and it was determined that SAM exits in a way to help understand what happened during run time. In the situation in Figure A.1, exiting with 9 avoid resubmission of the simulation. This was not very obvious until looking at some of the source code.

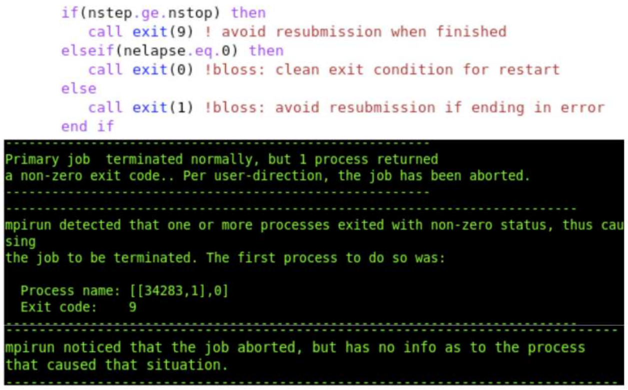

```
if(nstep.ge.nstop) then
   call exit(9) ! avoid resubmission when finished
elseif(nelapse.eq.0) then
   call exit(0) !bloss: clean exit condition for restart
else
   call exit(1) !bloss: avoid resubmission if ending in error
end if
```

```
-------------------------------------------------------
Primary job  terminated normally, but 1 process returned
a non-zero exit code.. Per user-direction, the job has been aborted.
-------------------------------------------------------
--------------------------------------------------------------------------
mpirun detected that one or more processes exited with non-zero status, thus cau
sing
the job to be terminated. The first process to do so was:

  Process name: [[34283,1],0]
  Exit code:    9
--------------------------------------------------------------------------
--------------------------------------------------------------------------------
mpirun noticed that the job aborted, but has no info as to the process
that caused that situation.
--------------------------------------------------------------------------------
```

Figure A.1. SAM Exit Handling and error messages after a successful SAM simulation. New exit options were created to stop confusing ending error messages. These messages were created from openmpi-intel/1.8 and openmpi-intel/1.6. Information from `https://gcc.gnu.org/onlinedocs/gfortran/EXECUTE_005fCOMMAND_005fLINE.htm` was used to create a work-around.

Table A.1. Compilers and cores on HPC machines

Machine	Cores per Node	Compiler
Linux Box		
Skybridge	16	Intel 1.8
Redsky	8	Intel 1.8

The SAM output consists of binary files which require a separate executable to convert to netCDF format. NetCDF format is commonly used in atmospheric sciences. A script was written to convert the output files to netCDF format immediately after the run. SAM also has issues with the case directories, in that by default each new submission will overwrite the case in the current directory. A python script was created to submit many jobs simultaneously and use different case directories for each submission. Variables such as number of subdomains, processors, and processes per node could then be changed and submitted to the queue without conflict with one another.

A.3 Automatic Data Downloads

Data from the Northern Slope of Alaska is collected at the ARM sites (Figure 2.2), which has to be reformatted for SAM to read. Regular simulations of NSA by SAM were desired, so a standing order was placed where data was grabbed from an FTP site. Options to grab include daily, weekly, or monthly. A python script was written. Python has a built-in ftp library function. A call was put into a bashrc file so anytime a terminal opens, new data is downloaded. The files requested were from the ECMWF reanalysis: oliecmwfvarX1.c1, oliecmwfflxX1.c1, oliecmwfsfc1lX1.c1, oliecmwfsfceX1.c1, oliecmwfsfcmlX1.c1, oliecmwftenX1.c1, and oliecmwfvarX1.c1 with timestamps. Figure A.2 shows an example of the the auto-email that was sent checking for new data on the ARM repository and how to download it. Knowledge was gained to create the automatic downloads scripts included information from the following websites: ARM automatic download information: `http://www.archive.arm.gov/docs/mirror.html` , automatic download (python resources): `http://stackoverflow.com/questions/22676/how-do-i-download-a-file-over-http-using-python` scheduling for running every hour:`http://stackoverflow.com/questions/15088037/python-script-to-do-somethin` `http://stackoverflow.com/questions/4543971/python-how-to-run-a-function-on-last-day-of-every-month` `http://stackoverflow.com/questions/15744781/bash-check-if-today-is-1st-day-of-month` , ftp site instructions: `http://www.archive.arm.gov/docs/standing-orders.html` , ftp download file: `http://stackoverflow.com/questions/11768214/python-download-a-file-over-an-ftp-server` `http://www.informit.com/articles/article.aspx?p=686162&seqNum=7` , `http://www.java2s.com/Tutorial/Python/0420__Network/UsingPythontoFetchFilesfromanFTPServer.htm` , and ARM standing order overview: `http://www.archive.arm.gov/docs/standing-orders.html#Overview` .

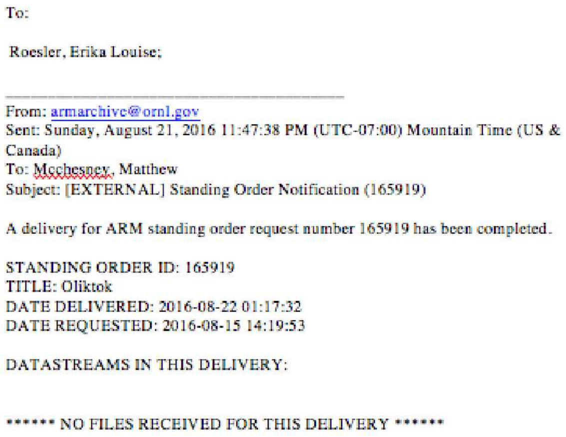

To:

Roesler, Erika Louise;

From: armarchive@ornl.gov
Sent: Sunday, August 21, 2016 11:47:38 PM (UTC-07:00) Mountain Time (US & Canada)
To: Mcchesney, Matthew
Subject: [EXTERNAL] Standing Order Notification (165919)

A delivery for ARM standing order request number 165919 has been completed.

STANDING ORDER ID: 165919
TITLE: Oliktok
DATE DELIVERED: 2016-08-22 01:17:32
DATE REQUESTED: 2016-08-15 14:19:53

DATASTREAMS IN THIS DELIVERY:

****** NO FILES RECEIVED FOR THIS DELIVERY ******

Figure A.2. Snapshot of ARM standing order email information. In this example, no new data was available for download. About once per month, new files from ECMWF were available for download.

A.4 Create GUI to View Results

To run these simulations it is not always a quick processes, and needs several steps from the user to compile, run, and convert the results to the desired format. Work was performed to make fewer user steps and more automatic steps, increasing efficiency. One idea of increasing efficiency was to create a graphical user interface (GUI) to select different buttons to give information about the results from the simulation. Creating a GUI combined several of these simulation viewing features into one place. The GUI has sever buttons that can be pressed to pull up graphs, look at run times, and view a python plot graph. The GUI is very flexible, and adding new features just takes a few modifications to the source code.

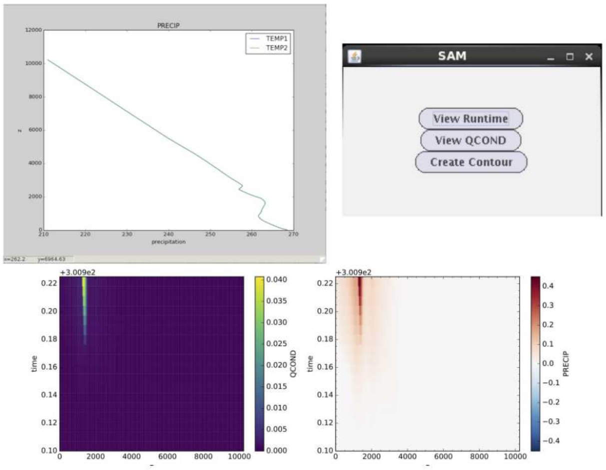

Figure A.3. SAM GUI idea with buttons, and profile for variable output. (top) Contour profiles showing converted output to netCDF format. (bottom)

A.5 Optimizing layout for Runtime

SAM gives the user flexibility for partitioning its computed domain over processors. Given this flexibility, there is ideally an optimal way to set-up and compile the model on a high-performance computer. Figures A.5 and A.5 shows a comparison of the different run times broken up on number of processes. Increasing the number of processes gave expected speed ups. It was found that when more square areas (i.e., where x and y are almost equal), noticeable speed ups occurred. With very large number of processes, speed-up was not seen indefinitely. This could be due to increasing the amount of communication between nodes slowing overall model speed down.

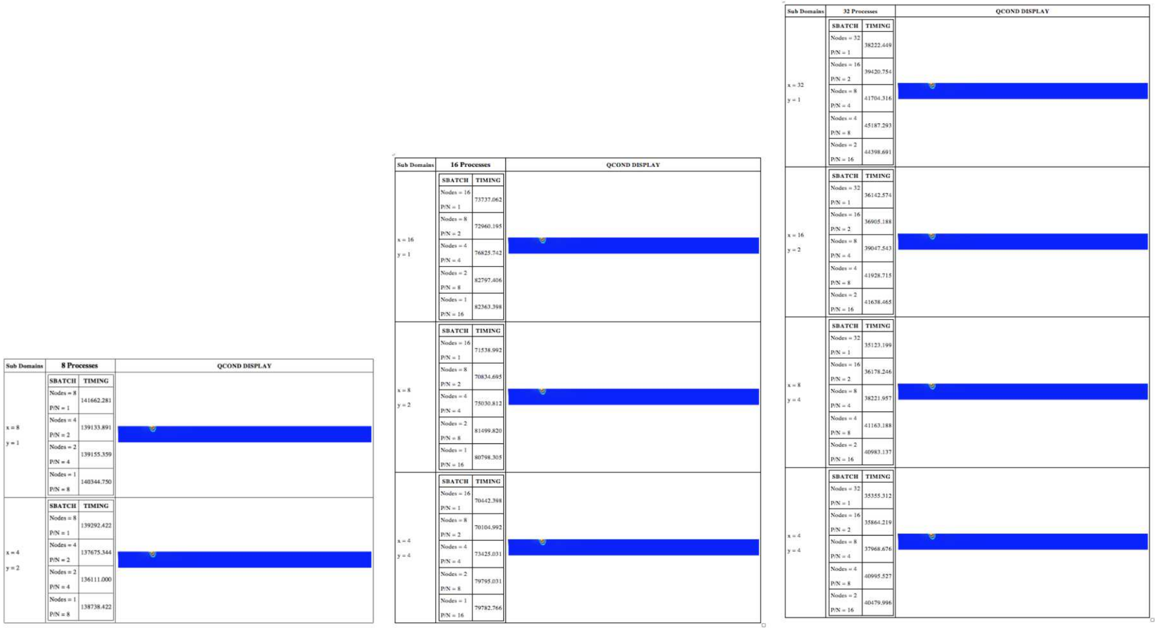

Sub Domains	SBATCH	TIMING	QCOND DISPLAY
	8 Processes		
x = 8 y = 1	Nodes = 8 P/N = 1	141662.281	
	Nodes = 4 P/N = 2	139133.891	
	Nodes = 2 P/N = 4	139155.359	
	Nodes = 1 P/N = 8	140344.750	
x = 4 y = 2	Nodes = 8 P/N = 1	139292.422	
	Nodes = 4 P/N = 2	137675.344	
	Nodes = 2 P/N = 4	136111.000	
	Nodes = 1 P/N = 8	138738.422	

(a) Skybridge with 8 processes

Sub Domains	SBATCH	TIMING	QCOND DISPLAY
	16 Processes		
x = 16 y = 1	Nodes = 16 P/N = 1	73737.062	
	Nodes = 8 P/N = 2	72960.195	
	Nodes = 4 P/N = 4	76825.742	
	Nodes = 2 P/N = 8	82797.406	
	Nodes = 1 P/N = 16	82363.398	
x = 8 y = 2	Nodes = 16 P/N = 1	71538.992	
	Nodes = 8 P/N = 2	70834.695	
	Nodes = 4 P/N = 4	75030.812	
	Nodes = 2 P/N = 8	81499.820	
	Nodes = 1 P/N = 16	80798.305	
x = 4 y = 4	Nodes = 16 P/N = 1	70442.398	
	Nodes = 8 P/N = 2	70104.992	
	Nodes = 4 P/N = 4	73425.031	
	Nodes = 2 P/N = 8	79795.031	
	Nodes = 1 P/N = 16	79782.766	

(b) Skybridge with 16 processes

Sub Domains	SBATCH	TIMING	QCOND DISPLAY
	32 Processes		
x = 32 y = 1	Nodes = 32 P/N = 1	38222.449	
	Nodes = 16 P/N = 2	39420.754	
	Nodes = 8 P/N = 4	41704.316	
	Nodes = 4 P/N = 8	45187.293	
	Nodes = 2 P/N = 16	44398.691	
x = 16 y = 2	Nodes = 32 P/N = 1	36142.574	
	Nodes = 16 P/N = 2	36905.188	
	Nodes = 8 P/N = 4	39047.543	
	Nodes = 4 P/N = 8	41928.715	
	Nodes = 2 P/N = 16	41638.465	
x = 8 y = 4	Nodes = 32 P/N = 1	35123.199	
	Nodes = 16 P/N = 2	36178.246	
	Nodes = 8 P/N = 4	38221.957	
	Nodes = 4 P/N = 8	41163.188	
	Nodes = 2 P/N = 16	40983.137	
x = 4 y = 4	Nodes = 32 P/N = 1	35355.312	
	Nodes = 16 P/N = 2	35864.219	
	Nodes = 8 P/N = 4	37968.676	
	Nodes = 4 P/N = 8	40995.527	
	Nodes = 2 P/N = 16	40479.996	

(c) Skybridge with 32 processes

Sub Domains	SBATCH	TIMING	ERROR MESSAGE	QCOND DISPLAY
	256 processes			
x = 256 y = 1	Nodes = 256 P/N = 1	N/A	SIGSEGV, segmentation fault occurred	
	Nodes = 128 P/N = 2	N/A	SIGSEGV, segmentation fault occurred	
	Nodes = 64 P/N = 4	N/A	SIGSEGV, segmentation fault occurred	
	Nodes = 32 P/N = 8	N/A	SIGSEGV, segmentation fault occurred	
x = 128 y = 2	Nodes = 256 P/N = 1	7819.651		
	Nodes = 128 P/N = 2	7862.561		
	Nodes = 64 P/N = 4	7904.189		
	Nodes = 32 P/N = 8	8383.204		
	Nodes = 16 P/N = 16	8435.068		
x = 64 y = 4	Nodes = 256 P/N = 1	6510.594		
	Nodes = 128 P/N = 2	6564.315		
	Nodes = 64 P/N = 4	6450.100		
	Nodes = 32 P/N = 8	6855.023		
	Nodes = 16 P/N = 16	6888.970		
x = 32 y = 8	Nodes = 256 P/N = 1	5797.471		
	Nodes = 128 P/N = 2	5859.846		
	Nodes = 64 P/N = 4	5834.877		
	Nodes = 32 P/N = 8	6237.289		
	Nodes = 16 P/N = 16	6262.523		
x = 16 y = 16	Nodes = 256 P/N = 1	5677.881		
	Nodes = 128 P/N = 2	5794.081		
	Nodes = 64 P/N = 4	5773.102		
	Nodes = 32 P/N = 8	6067.917		
	Nodes = 16 P/N = 16	6077.191		

Sub Domains	SBATCH	TIMING	ERROR MESSAGE	
	512 processes			
x = 512 y = 1	Nodes = 512 P/N = 1	N/A	SIGSEGV, segmentation fault occurred	
	Nodes = 256 P/N = 2	N/A	SIGSEGV, segmentation fault occurred	
	Nodes = 128 P/N = 4	N/A	SIGSEGV, segmentation fault occurred	
	Nodes = 64 P/N = 8	N/A	SIGSEGV, segmentation fault occurred	
	Nodes = 32 P/N = 16	N/A	SIGSEGV, segmentation fault occurred	
x = 256 y = 2	Nodes = 512 P/N = 1	33549.598		
	Nodes = 256 P/N = 2	34011.598		
	Nodes = 128 P/N = 4	34531.758		
	Nodes = 64 P/N = 8	36931.285		
	Nodes = 32 P/N = 16	36864.215		
x = 128 y = 4	Nodes = 512 P/N = 1	27515.777		
	Nodes = 256 P/N = 2	27966.852		
	Nodes = 128 P/N = 4	35193.074		
	Nodes = 64 P/N = 8	35869.789		
	Nodes = 32 P/N = 16	29375.573		
x = 64 y = 8	Nodes = 512 P/N = 1	N/A	SIGSEGV, segmentation fault occurred	
	Nodes = 256 P/N = 2	25429.051		
	Nodes = 128 P/N = 4	33382.191		
	Nodes = 64 P/N = 8	26451.904		
	Nodes = 32 P/N = 16	26264.195		
x = 32 y = 16	Nodes = 512 P/N = 1	23109.615		
	Nodes = 256 P/N = 2	23996.428		
	Nodes = 128 P/N = 4	24070.115		
	Nodes = 64 P/N = 8	25143.809		
	Nodes = 32 P/N = 16	25214.479		

(d) Skybridge with 256 processes **(e)** Skybridge with 512 processes

Figure A.4. SAM domain decomposition (cartesian grid for x and y coordinates) for processor layout and node ratio on Skybridge with 8, 16, 32, 256, and 512 processes. Time-height profiles of the QCOND (total condensed water mass missing ratio) are shown for comparison between each of the decomposition options, showing how the different configurations are most-likely not answer changing.

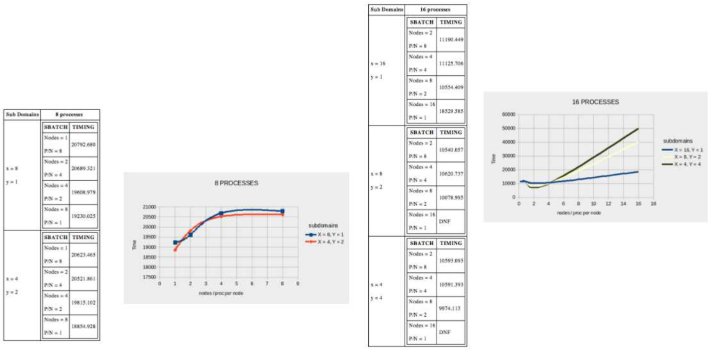

Sub Domains	8 processes	
	SBATCH	TIMING
x = 8 y = 1	Nodes = 1 P/N = 8	20792.680
	Nodes = 2 P/N = 4	20689.321
	Nodes = 4 P/N = 2	19608.979
	Nodes = 8 P/N = 1	19230.025
	SBATCH	TIMING
x = 4 y = 2	Nodes = 1 P/N = 8	20623.465
	Nodes = 2 P/N = 4	20521.861
	Nodes = 4 P/N = 2	19815.102
	Nodes = 8 P/N = 1	18854.928

Sub Domains	16 processes	
	SBATCH	TIMING
x = 16 y = 1	Nodes = 2 P/N = 8	11190.449
	Nodes = 4 P/N = 4	11125.706
	Nodes = 8 P/N = 2	10554.409
	Nodes = 16 P/N = 1	18529.585
	SBATCH	TIMING
x = 8 y = 2	Nodes = 2 P/N = 8	10540.857
	Nodes = 4 P/N = 4	10620.737
	Nodes = 8 P/N = 2	10078.995
	Nodes = 16 P/N = 1	DNF
	SBATCH	TIMING
x = 4 y = 4	Nodes = 2 P/N = 8	10593.093
	Nodes = 4 P/N = 4	10591.393
	Nodes = 8 P/N = 2	9974.113
	Nodes = 16 P/N = 1	DNF

Sub Domains	32 processes	
	SBATCH	TIMING
x = 32 y = 1	Nodes = 4 P/N = 8	7388.735
	Nodes = 8 P/N = 4	7459.682
	Nodes = 16 P/N = 2	6549.656
	Nodes = 32 P/N = 1	6524.374
	SBATCH	TIMING
x = 16 y = 2	Nodes = 4 P/N = 8	6287.830
	Nodes = 8 P/N = 4	6419.189
	Nodes = 16 P/N = 2	6644.139
	Nodes = 32 P/N = 1	5707.615
	SBATCH	TIMING
x = 8 y = 4	Nodes = 4 P/N = 8	5983.377
	Nodes = 8 P/N = 4	5877.892
	Nodes = 16 P/N = 2	5649.302
	Nodes = 32 P/N = 1	5453.477

(a) Redsky with 8 processes **(b)** Redsky with 16 processes **(c)** Redsky with 32 processes

Sub Domains	64 processes	
	SBATCH	TIMING
x = 64 y = 1	Nodes = 8 P/N = 8	4565.228
	Nodes = 16 P/N = 4	4448.986
	Nodes = 32 P/N = 2	DNF
	Nodes = 64 P/N = 1	4070.918
	SBATCH	TIMING
x = 32 y = 2	Nodes = 8 P/N = 8	3359.703
	Nodes = 16 P/N = 4	3237.021
	Nodes = 32 P/N = 2	4382.107
	Nodes = 64 P/N = 1	4590.907
	SBATCH	TIMING
x = 16 y = 4	Nodes = 8 P/N = 8	3953.233
	Nodes = 16 P/N = 4	3804.199
	Nodes = 32 P/N = 2	3418.131
	Nodes = 64 P/N = 1	3273.804
	SBATCH	TIMNG
x = 8 y = 8	Nodes = 8 P/N = 8	3093.355
	Nodes = 16 P/N = 4	3054.307
	Nodes = 32 P/N = 2	2982.469
	Nodes = 64 P/N = 1	3026.749

Sub Domains	128 processes	
	SBATCH	TIMING
x = 128 y = 1	Nodes = 16 P/N = 8	segfault
	Nodes = 32 P/N = 4	segfault
	Nodes = 64 P/N = 2	segfault
	Nodes = 128 P/N = 1	segfault
	SBATCH	TIMING
x = 64 y = 2	Nodes = 16 P/N = 8	3035.785
	Nodes = 32 P/N = 4	2437.562
	Nodes = 64 P/N = 2	2509.605
	Nodes = 128 P/N = 1	3053.721
	SBATCH	TIMING
x = 32 y = 4	Nodes = 16 P/N = 8	2141.674
	Nodes = 32 P/N = 4	2123.281
	Nodes = 64 P/N = 2	2885.976
	Nodes = 128 P/N = 1	2335.812
	SBATCH	TIMING
x = 16 y = 8	Nodes = 16 P/N = 8	2130.459
	Nodes = 32 P/N = 4	2589.767
	Nodes = 64 P/N = 2	2822.146
	Nodes = 128 P/N = 1	1998.857

Sub Domains	256 processes		
	SBATCH	TIMING	ERROR MESSAGE
x = 256 y = 1	Nodes = 256 P/N = 1	N/A	SIGSEGV, segmentation fault occured
	Nodes = 128 P/N = 2	N/A	SIGSEGV, segmentation fault occured
	Nodes = 64 P/N = 4	N/A	SIGSEGV, segmentation fault occured
	Nodes = 32 P/N = 8	N/A	SIGSEGV, segmentation fault occured
	SBATCH	TIMING	
x = 128 y = 2	Nodes = 256 P/N = 1	9124.990	
	Nodes = 128 P/N = 2	9741.000	
	Nodes = 64 P/N = 4	10270.075	
	Nodes = 32 P/N = 8	10739.189	
	SBATCH	TIMING	
x = 64 y = 4	Nodes = 256 P/N = 1	7313.376	
	Nodes = 128 P/N = 2	7966.387	
	Nodes = 64 P/N = 4	7730.375	
	Nodes = 32 P/N = 8	8129.475	
	SBATCH	TIMING	
x = 32 y = 8	Nodes = 256 P/N = 1	7277.205	
	Nodes = 128 P/N = 2	6919.824	
	Nodes = 64 P/N = 4	7066.760	
	Nodes = 32 P/N = 8	7431.660	
	SBATCH	TIMING	
x = 16 y = 16	Nodes = 256 P/N = 1		
	Nodes = 128 P/N = 2	6930.921	
	Nodes = 64 P/N = 4	6985.223	
	Nodes = 32 P/N = 8		

(d) Redsky with 64 processes **(e)** Redsky with 128 processes **(f)** Redsky with 256 processes

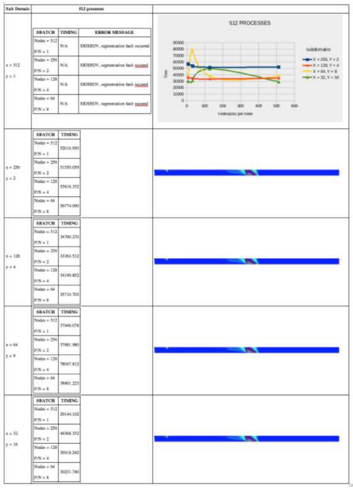

Sub Domain	512 processes		
	SBATCH	TIMING	ERROR MESSAGE
x = 512 y = 1	Nodes = 512 P/N = 1	N/A	SIGSEGV, segmentation fault occured
	Nodes = 256 P/N = 2	N/A	SIGSEGV, segmentation fault occured
	Nodes = 128 P/N = 4	N/A	SIGSEGV, segmentation fault occured
	Nodes = 64 P/N = 8	N/A	SIGSEGV, segmentation fault occured
	SBATCH	TIMING	
x = 256 y = 2	Nodes = 512 P/N = 1	52016.930	
	Nodes = 256 P/N = 2	51530.059	
	Nodes = 128 P/N = 4	53816.332	
	Nodes = 64 P/N = 8	56774.090	
	SBATCH	TIMING	
x = 128 y = 4	Nodes = 512 P/N = 1	34700.270	
	Nodes = 256 P/N = 2	33363.512	
	Nodes = 128 P/N = 4	34199.852	
	Nodes = 64 P/N = 8	35710.703	
	SBATCH	TIMING	
x = 64 y = 8	Nodes = 512 P/N = 1	37948.078	
	Nodes = 256 P/N = 2	37881.980	
	Nodes = 128 P/N = 4	78047.812	
	Nodes = 64 P/N = 8	38801.223	
	SBATCH	TIMING	
x = 32 y = 16	Nodes = 512 P/N = 1	29144.102	
	Nodes = 256 P/N = 2	40366.332	
	Nodes = 128 P/N = 4	30918.242	
	Nodes = 64 P/N = 8	30251.740	

(g) Redsky with 512 processes

Figure A.5. SAM domain decomposition (cartesian grid for x and y coordinates) for processor layout and node ratio on Redsky with 8, 16, 32, 64, 128, 256, and 512 processes. Time-height profiles of the QCOND (total condensed water mass missing ratio) are shown for comparison between each of the decomposition options, showing how the different configurations are most-likely not answer changing.

A.6 Summary

By creating ways to get automatic downloads, comparing compilers, looking at run times, and combining running the model and the conversions at the same time, work was sped up in getting results.

Appendix B

Polar Lows and Arctic Storms

The purpose of this work was ancillary to the main project in that it was going to investigate the climate model bias of storms in the North Slope region of the Arctic as another type of cloud bias stemming from a different meteorological scenario. Two types of storms were to be studied in this work: polar lows and Arctic storms. Polar lows are smaller in size and duration than Arctic storms but have more extreme characteristics (e.g., pressure, wind, precipitation). Goals of this project included investigating the capability of variable resolution models to capture and produce physically realistic polar lows and Arctic storms. Achievement of this goal would be to facilitate future studies regarding the kinetic energy transfer of polar lows from atmosphere to ocean and atmosphere to sea ice. Robustly defining polar lows was to be a key step in this work. Although the polar lows research never materialized from these ideas, some Arctic storm analysis was performed.

Zarzycki and Jablonowski (2014) showed the utility of variable resolution grids in studying the climatology of North Atlantic hurricanes. He found the higher resolution grid spacing produced more realistic storm climatologies when compared to observations. The same hypothesis was made regarding extratropical storms. Vavrus (2013) showed models compare well to observations. Mesquita et al. (2010) showed in reanalysis data that cyclogenesis of Arctic storms occurs in regions such as the Sea of Okhotsk, west of the Asian continent and cyclolysis (or death) of the Arctic storms occurs in the Gulf of Alaska where the storms meet the land and in the Bering Sea where the storms meet the ice edge.

Using the storm-finding software, Stride Search (Bosler et al., 2016), storms were defined as objects in atmospheric data with pressure less than 990 hPa, vorticity greater than 1 x 10^{-5} m s^{-2}, and translational travel speed greater than 20 m s^{-2}. The Community Atmospheric Model (CAM), version 5 (Neale et al., 2012), with the spectral element dynamical core was run for to produce five years of climatological year 1850. Three simulations, one uniform high resolution of one-eighth degree resolution ($\sim$14 km), one uniform low resolution of 1 degree resolution ($\sim$110 km), and one variable resolution of 1 to one-quarter to one-eighth degree ($\sim$110 km to $\sim$25 km to $\sim$14 km), were produced. The variable resolution grid used for this work encompasses the cyclogenesis and cyclolysis regions residing in the North Pacific to include the regions of the Sea of Okhotsk and Gulf of Alaska. To include the North Slope area and sea ice extent through the Bering Sea, the variable resolution went northward into the Bering Strait where the resolution increases to one-eighth degree. This is shown in Figure B.1.

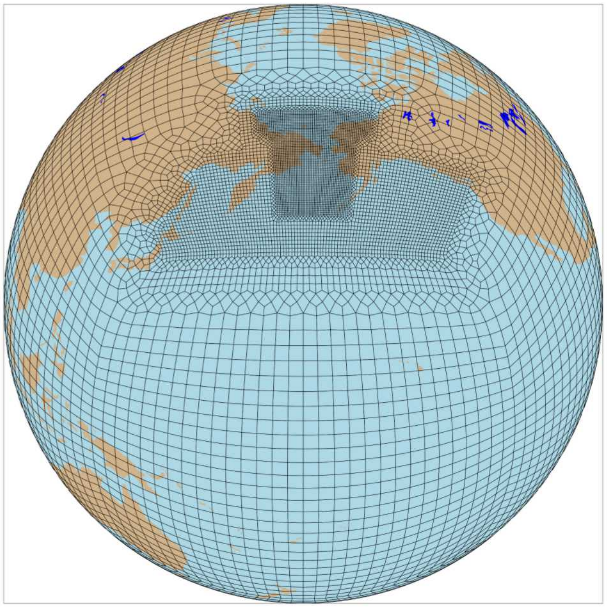

Figure B.1. Variable resolution grid used for Arctic Storms study.

Results of the simulations and the total number of storm tracks found for each simulation, by season, are shown in Table B.1 and Figure B.2.

Table B.1. Total 5-year Storm Count for 30N to 90N

Resolution	Storm Count
Low Resolution	536
High Resolution	833
Variable Resolution	658

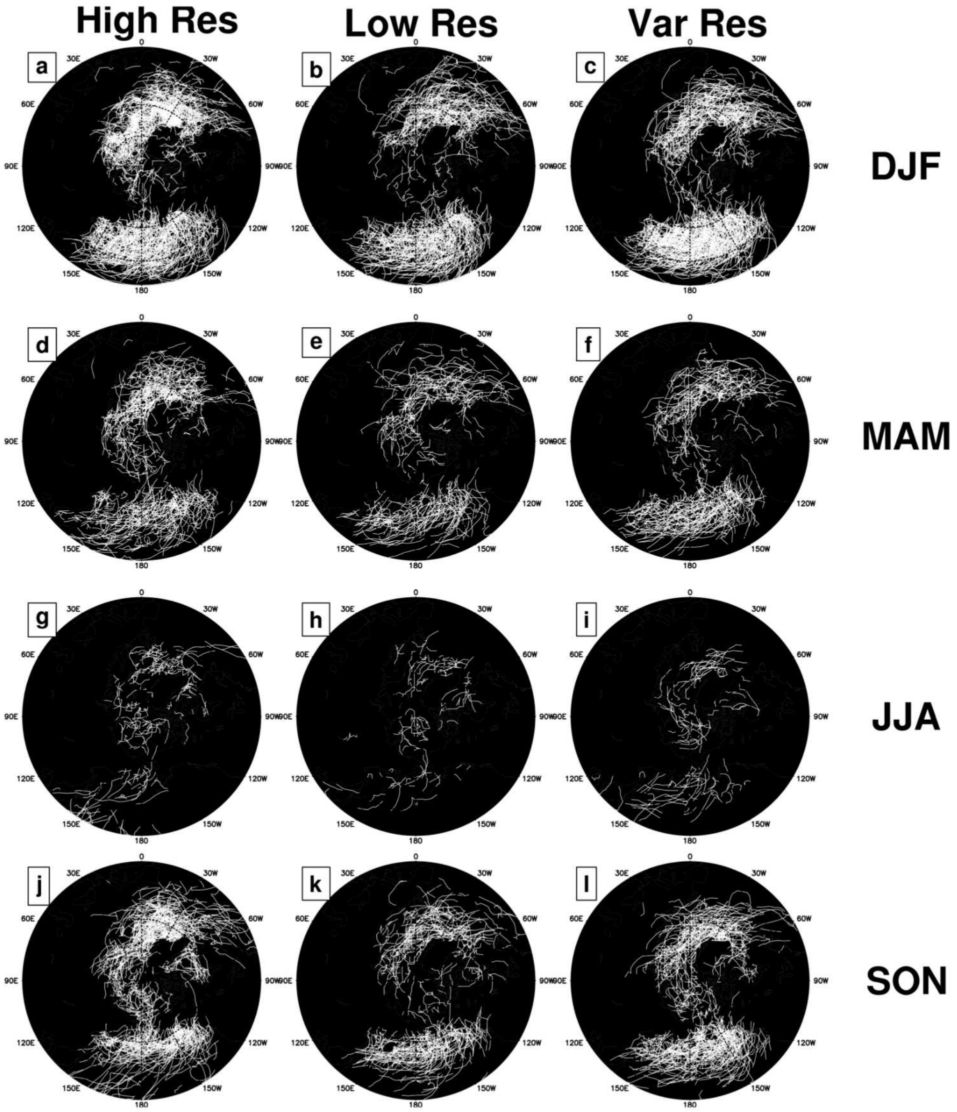

Figure B.2. Storm tracks by season and simulation.

Appendix C

Visualizing Atmospheric Data

Often scientific discoveries are shared with a limited audience in a limited way with line graphs or simple charts. More detailed visualization methods are available for sharing and communicating scientific findings that can enhance relationships between variables during analysis. Given the amount of observational and simulation data produced by this one project, it was wondered how best to analyze and share the findings with a broader audience. Visualizations will be used internally on monitors/tables, externally on posters with augmented reality apps, and hand-held touch surfaces for colleagues at conferences. Even within the project's members, it was desired to view simulations faster to give improved intuition regarding the output and how it can be correlated with the hypothesis of the simulation's experiment.

A subproject was initiated to investigate this question using a new visualization software program called Houdini from SideFx.[1] A license was obtained to use Houdini for this project. Houdini is a Hollywood-class software program, winning Technical Achievement Academy Awards, and can be used to create cinematic scientific visualizations for public outreach and improved understanding. Houdini is a highly procedural program, preserves history, and is memory efficient. It can handle multiple file types, although netCDF was not one of those file types. It also has many scripting interfaces including Python, Hscript, Vex, and C++. An important feature of Houdini is that it has a realistic lighting camera which controls the depth of field and motion blur. These two features are not found in traditional scientific visualization software. One potential disadvantage of Houdini is that it cannot be used for quantitative analysis on the simulation data.

The goal of this subproject was to share results of the simulations in a intuitive way with colleagues, customers, and potential collaborators by showing the data in its full four-dimensional form (i.e., three spatial coordinates and one temporal coordinate). A work flow was developed to produce quality visualizations from atmospheric simulations, minimizing user steps. The work flow is pictured in Figure C.1. It was also necessary to update the graphics card and buy data storage for the computer used to run Houdini. A screenshot of the Houdini workspace is shown in Figure C.2. The data used to create the visualizations were from a simulation of an Arctic Stratocumulus cloud produced by SAM. The simulation domain was 20 m above the surface of Oliktok Point. Outputs were 128 grid points in the cartesian x, y, and z coordinates and 360 time snapshots of environmental variables such as temperature, winds, pressure, liquid cloud, and ice cloud. To make the cloud visualization, all of the water-type variables (precipitating and non-precipitating) were summed to create a total water field for a cloud scene for a given time snapshot. Figure C.3

---

[1] `https://www.sidefx.com/`

shows the final product of the simulated cloud output from the SAM domain superimposed over a Google Earth picture of Oliktok Point. Future work could fully automate the process using the Houdini native programming language.

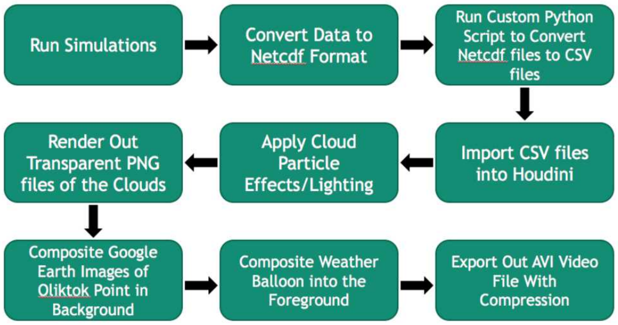

Figure C.1. Workflow developed for preparing simulation data for Houdini and viewing as final product in video file.

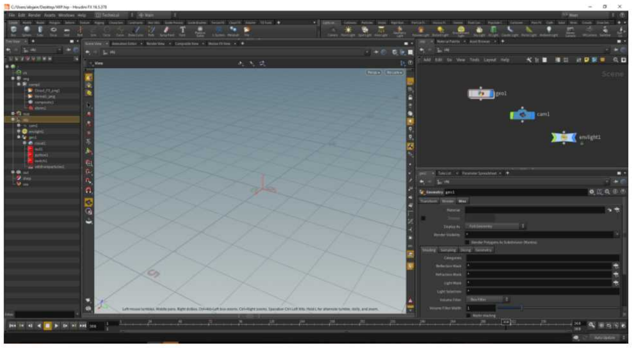

Figure C.2. A screenshot of the workspace in Houdini to process the stratocumulus cloud simulations.

Figure C.3. A screenshot portion of the movie created by using Houdini to improve visualization of three dimensional model output from SAM.

Appendix D

External Communication Media

This chapter serves to archive some selected posters, one-pagers, and other media that were presented during the projects lifetime. Please contact the lead author of the media for a copy.

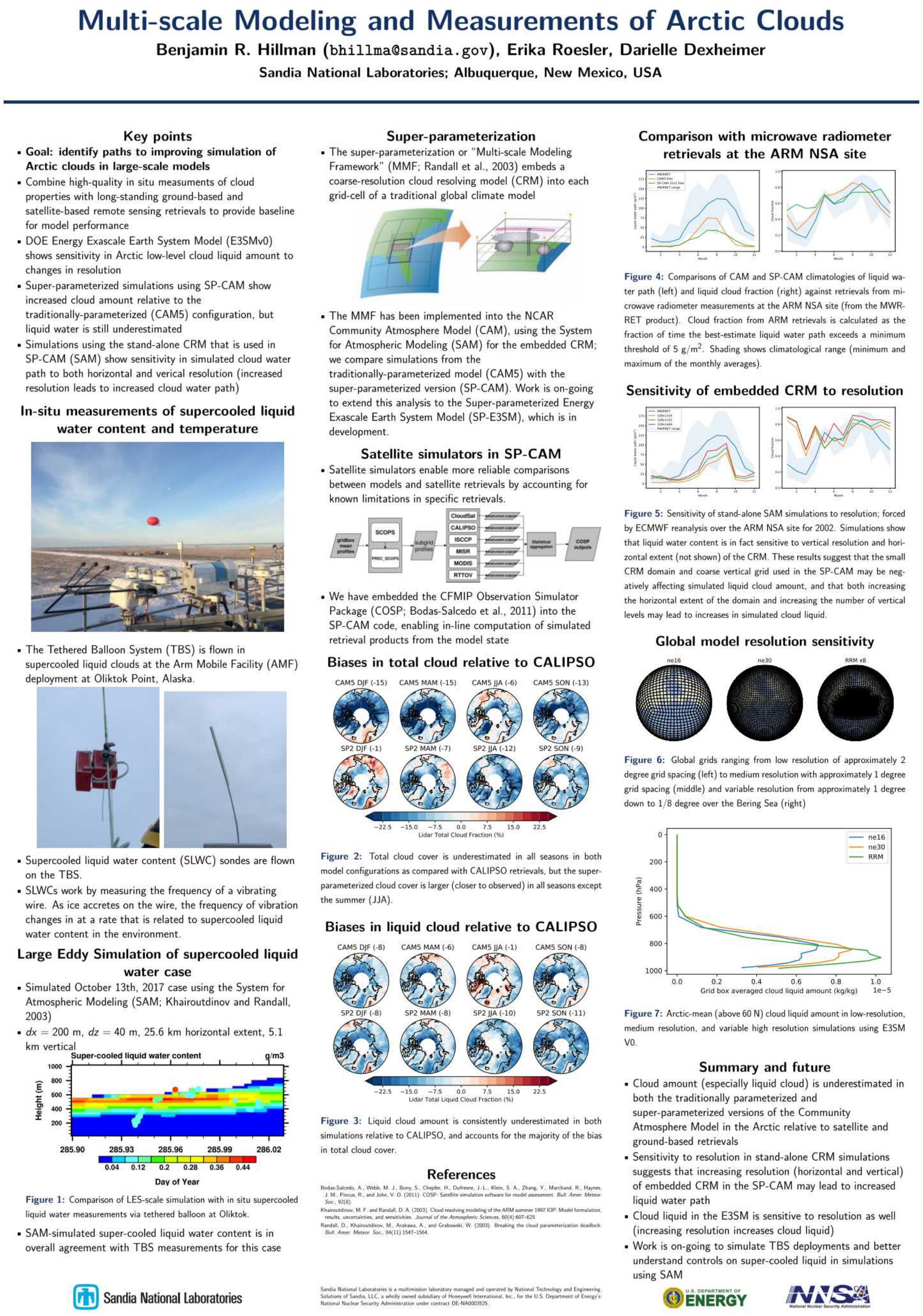

Multi-scale Modeling and Measurements of Arctic Clouds

Benjamin R. Hillman (`bhillma@sandia.gov`), Erika Roesler, Darielle Dexheimer

Sandia National Laboratories; Albuquerque, New Mexico, USA

Key points

- **Goal: identify paths to improving simulation of Arctic clouds in large-scale models**
- Combine high-quality in situ measuments of cloud properties with long-standing ground-based and satellite-based remote sensing retrievals to provide baseline for model performance
- DOE Energy Exascale Earth System Model (E3SMv0) shows sensitivity in Arctic low-level cloud liquid amount to changes in resolution
- Super-parameterized simulations using SP-CAM show increased cloud amount relative to the traditionally-parameterized (CAM5) configuration, but liquid water is still underestimated
- Simulations using the stand-alone CRM that is used in SP-CAM (SAM) show sensitivity in simulated cloud water path to both horizontal and verical resolution (increased resolution leads to increased cloud water path)

In-situ measurements of supercooled liquid water content and temperature

- The Tethered Balloon System (TBS) is flown in supercooled liquid clouds at the Arm Mobile Facility (AMF) deployment at Oliktok Point, Alaska.

- Supercooled liquid water content (SLWC) sondes are flown on the TBS.
- SLWCs work by measuring the frequency of a vibrating wire. As ice accretes on the wire, the frequency of vibration changes in at a rate that is related to supercooled liquid water content in the environment.

Large Eddy Simulation of supercooled liquid water case

- Simulated October 13th, 2017 case using the System for Atmospheric Modeling (SAM; Khairoutdinov and Randall, 2003)
- $dx = 200$ m, $dz = 40$ m, 25.6 km horizontal extent, 5.1 km vertical

Figure 1: Comparison of LES-scale simulation with in situ supercooled liquid water measurements via tethered balloon at Oliktok.

- SAM-simulated super-cooled liquid water content is in overall agreement with TBS measurements for this case

Sandia National Laboratories

Super-parameterization

- The super-parameterization or "Multi-scale Modeling Framework" (MMF; Randall et al., 2003) embeds a coarse-resolution cloud resolving model (CRM) into each grid-cell of a traditional global climate model

- The MMF has been implemented into the NCAR Community Atmosphere Model (CAM), using the System for Atmospheric Modeling (SAM) for the embedded CRM; we compare simulations from the traditionally-parameterized model (CAM5) with the super-parameterized version (SP-CAM). Work is on-going to extend this analysis to the Super-parameterized Energy Exascale Earth System Model (SP-E3SM), which is in development.

Satellite simulators in SP-CAM

- Satellite simulators enable more reliable comparisons between models and satellite retrievals by accounting for known limitations in specific retrievals.

- We have embedded the CFMIP Observation Simulator Package (COSP; Bodas-Salcedo et al., 2011) into the SP-CAM code, enabling in-line computation of simulated retrieval products from the model state

Biases in total cloud relative to CALIPSO

Figure 2: Total cloud cover is underestimated in all seasons in both model configurations as compared with CALIPSO retrievals, but the super-parameterized cloud cover is larger (closer to observed) in all seasons except the summer (JJA).

Biases in liquid cloud relative to CALIPSO

Figure 3: Liquid cloud amount is consistently underestimated in both simulations relative to CALIPSO, and accounts for the majority of the bias in total cloud cover.

References

Bodas-Salcedo, A., Webb, M. J., Bony, S., Chepfer, H., Dufresne, J.-L., Klein, S. A., Zhang, Y., Marchand, R., Haynes, J. M., Pincus, R., and John, V. O. (2011). COSP: Satellite simulation software for model assessment. *Bull. Amer. Meteor. Soc.*, 92(8).

Khairoutdinov, M. F. and Randall, D. A. (2003). Cloud resolving modeling of the ARM summer 1997 IOP: Model formulation, results, uncertainties, and sensitivities. *Journal of the Atmospheric Sciences*, 60(4):607–625.

Randall, D., Khairoutdinov, M., Arakawa, A., and Grabowski, W. (2003). Breaking the cloud parameterization deadlock. *Bull. Amer. Meteor. Soc.*, 84(11):1547–1564.

Sandia National Laboratories is a multimission laboratory managed and operated by National Technology and Engineering Solutions of Sandia, LLC, a wholly owned subsidiary of Honeywell International, Inc., for the U.S. Department of Energy's National Nuclear Security Administration under contract DE-NA0003525.

Comparison with microwave radiometer retrievals at the ARM NSA site

Figure 4: Comparisons of CAM and SP-CAM climatologies of liquid water path (left) and liquid cloud fraction (right) against retrievals from microwave radiometer measurements at the ARM NSA site (from the MWRRET product). Cloud fraction from ARM retrievals is calculated as the fraction of time the best-estimate liquid water path exceeds a minimum threshold of 5 g/m^2. Shading shows climatological range (minimum and maximum of the monthly averages).

Sensitivity of embedded CRM to resolution

Figure 5: Sensitivity of stand-alone SAM simulations to resolution; forced by ECMWF reanalysis over the ARM NSA site for 2002. Simulations show that liquid water content is in fact sensitive to vertical resolution and horizontal extent (not shown) of the CRM. These results suggest that the small CRM domain and coarse vertical grid used in the SP-CAM may be negatively affecting simulated liquid cloud amount, and that both increasing the horizontal extent of the domain and increasing the number of vertical levels may lead to increases in simulated cloud liquid.

Global model resolution sensitivity

Figure 6: Global grids ranging from low resolution of approximately 2 degree grid spacing (left) to medium resolution with approximately 1 degree grid spacing (middle) and variable resolution from approximately 1 degree down to 1/8 degree over the Bering Sea (right)

Figure 7: Arctic-mean (above 60 N) cloud liquid amount in low-resolution, medium resolution, and variable high resolution simulations using E3SM V0.

Summary and future

- Cloud amount (especially liquid cloud) is underestimated in both the traditionally parameterized and super-parameterized versions of the Community Atmosphere Model in the Arctic relative to satellite and ground-based retrievals
- Sensitivity to resolution in stand-alone CRM simulations suggests that increasing resolution (horizontal and vertical) of embedded CRM in the SP-CAM may lead to increased liquid water path
- Cloud liquid in the E3SM is sensitive to resolution as well (increasing resolution increases cloud liquid)
- Work is on-going to simulate TBS deployments and better understand controls on super-cooled liquid in simulations using SAM

U.S. DEPARTMENT OF ENERGY

NNSA National Nuclear Security Administration

Figure D.1. Poster presented at the 2018 Polar Science Conference in Davos, Switzerland by Ben Hillman summarizing the entire project.

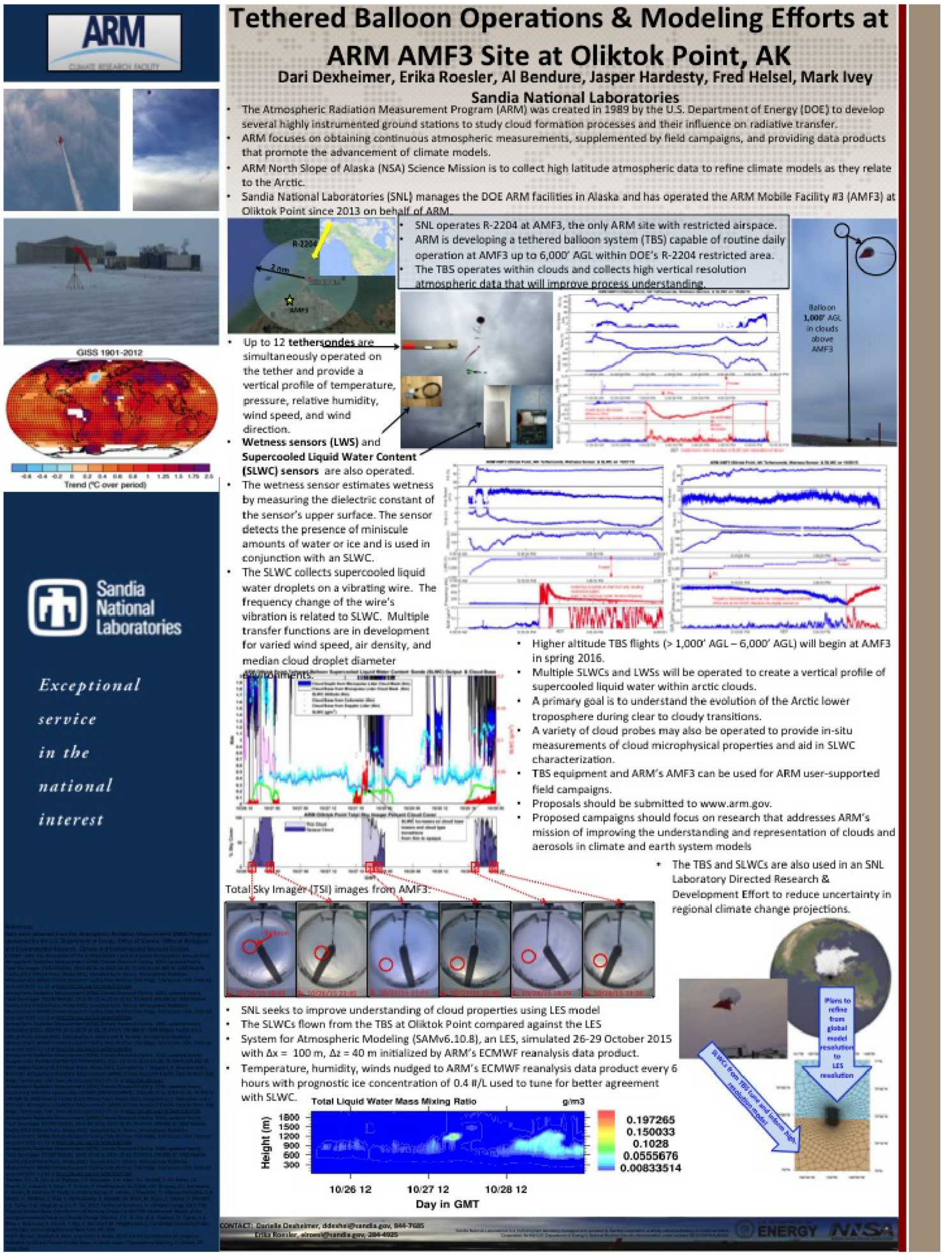

Tethered Balloon Operations & Modeling Efforts at ARM AMF3 Site at Oliktok Point, AK

Dari Dexheimer, Erika Roesler, Al Bendure, Jasper Hardesty, Fred Helsel, Mark Ivey

Sandia National Laboratories

- The Atmospheric Radiation Measurement Program (ARM) was created in 1989 by the U.S. Department of Energy (DOE) to develop several highly instrumented ground stations to study cloud formation processes and their influence on radiative transfer.
- ARM focuses on obtaining continuous atmospheric measurements, supplemented by field campaigns, and providing data products that promote the advancement of climate models.
- ARM North Slope of Alaska (NSA) Science Mission is to collect high latitude atmospheric data to refine climate models as they relate to the Arctic.
- Sandia National Laboratories (SNL) manages the DOE ARM facilities in Alaska and has operated the ARM Mobile Facility #3 (AMF3) at Oliktok Point since 2013 on behalf of ARM.

- SNL operates R-2204 at AMF3, the only ARM site with restricted airspace.
- ARM is developing a tethered balloon system (TBS) capable of routine daily operation at AMF3 up to 6,000' AGL within DOE's R-2204 restricted area.
- The TBS operates within clouds and collects high vertical resolution atmospheric data that will improve process understanding.

- Up to 12 **tethersondes** are simultaneously operated on the tether and provide a vertical profile of temperature, pressure, relative humidity, wind speed, and wind direction.
- **Wetness sensors (LWS)** and **Supercooled Liquid Water Content (SLWC) sensors** are also operated.
- The wetness sensor estimates wetness by measuring the dielectric constant of the sensor's upper surface. The sensor detects the presence of miniscule amounts of water or ice and is used in conjunction with an SLWC.
- The SLWC collects supercooled liquid water droplets on a vibrating wire. The frequency change of the wire's vibration is related to SLWC. Multiple transfer functions are in development for varied wind speed, air density, and median cloud droplet diameter environments.

- Higher altitude TBS flights (> 1,000' AGL – 6,000' AGL) will begin at AMF3 in spring 2016.
- Multiple SLWCs and LWSs will be operated to create a vertical profile of supercooled liquid water within arctic clouds.
- A primary goal is to understand the evolution of the Arctic lower troposphere during clear to cloudy transitions.
- A variety of cloud probes may also be operated to provide in-situ measurements of cloud microphysical properties and aid in SLWC characterization.
- TBS equipment and ARM's AMF3 can be used for ARM user-supported field campaigns.
- Proposals should be submitted to www.arm.gov.
- Proposed campaigns should focus on research that addresses ARM's mission of improving the understanding and representation of clouds and aerosols in climate and earth system models

- The TBS and SLWCs are also used in an SNL Laboratory Directed Research & Development Effort to reduce uncertainty in regional climate change projections.

- SNL seeks to improve understanding of cloud properties using LES model
- The SLWCs flown from the TBS at Oliktok Point compared against the LES
- System for Atmospheric Modeling (SAMv6.10.8), an LES, simulated 26-29 October 2015 with Δx = 100 m, Δz = 40 m initialized by ARM's ECMWF reanalysis data product.
- Temperature, humidity, winds nudged to ARM's ECMWF reanalysis data product every 6 hours with prognostic ice concentration of 0.4 #/L used to tune for better agreement with SLWC.

Sandia National Laboratories

Exceptional service in the national interest

Figure D.2. Poster presented at the 2016 American Meteorological Society's Annual Meeting by Darielle Dexheimer introducing preliminary analysis of the TBS and sensors.

Appendix E

Project Management

The project management was organized through Sandia's Confluence wiki space. Within that space were sections for the Measurements, Modeling, and Project Management. Presentations, results, and documentation were shared within the group in the wiki space. Figure E.1 shows a screenshot of the mature confluence space with branches for each of the sub-topics of study supported in this project. Three tasks were created for this project: project management, measurements, and modeling. Figure E.2 show the variety of measurements datasets and modeling tools that were envisioned to be useful for this project. Not all tools were eventually used or investigated equally. The wiki will remain a space for housing this SAND report.

The wiki was useful, but in retrospect, using Jupyter notebooks and LaTeX from in Gitlab might have simplified final documentation for reports and publications.

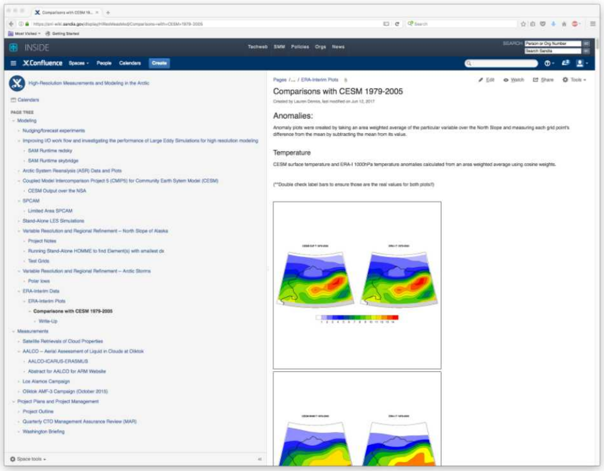

Comparisons with CESM 1979-2005

Created by Lauren Dennis, last modified on Jun 12, 2017

Anomalies:

Anomaly plots were created by taking an area weighted average of the particular variable over the North Slope and measuring each grid point's difference from the mean by subtracting the mean from its value.

Temperature

CESM surface temperature and ERA-I 1000hPa temperature anomalies calculated from an area weighted average using cosine weights.

(**Double check label bars to ensure those are the real values for both plots!!)

Figure E.1. An example of the wiki-space used to share results, presentations, and project organization throughout the three-year term.

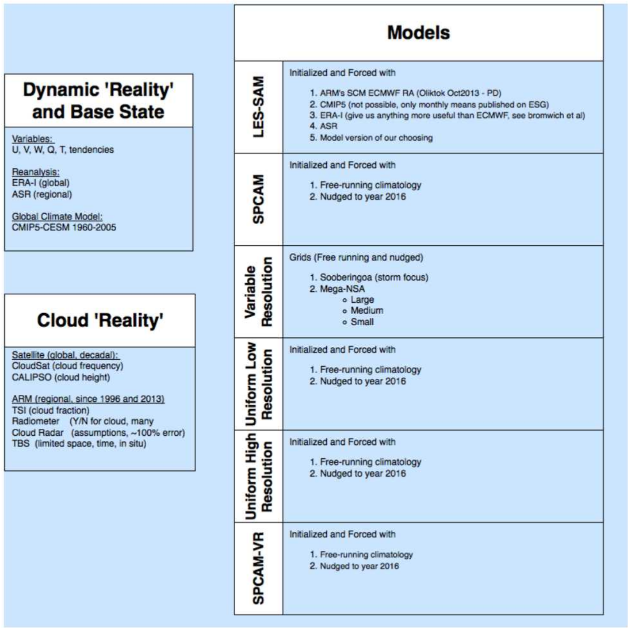

Dynamic 'Reality' and Base State

Variables:
U, V, W, Q, T, tendencies

Reanalysis:
ERA-I (global)
ASR (regional)

Global Climate Model:
CMIP5-CESM 1960-2005

Cloud 'Reality'

Satellite (global, decadal):
CloudSat (cloud frequency)
CALIPSO (cloud height)

ARM (regional, since 1996 and 2013)
TSI (cloud fraction)
Radiometer (Y/N for cloud, many
Cloud Radar (assumptions, ~100% error)
TBS (limited space, time, in situ)

Models	
LES-SAM	Initialized and Forced with 1. ARM's SCM ECMWF RA (Oliktok Oct2013 - PD) 2. CMIP5 (not possible, only monthly means published on ESG) 3. ERA-I (give us anything more useful than ECMWF, see bromwich et al) 4. ASR 5. Model version of our choosing
SPCAM	Initialized and Forced with 1. Free-running climatology 2. Nudged to year 2016
Variable Resolution	Grids (Free running and nudged) 1. Sooberingoa (storm focus) 2. Mega-NSA ∘ Large ∘ Medium ∘ Small
Uniform Low Resolution	Initialized and Forced with 1. Free-running climatology 2. Nudged to year 2016
Uniform High Resolution	Initialized and Forced with 1. Free-running climatology 2. Nudged to year 2016
SPCAM-VR	Initialized and Forced with 1. Free-running climatology 2. Nudged to year 2016

Figure E.2. All components, measurements and modeling, envisioned to be used in this project.

DISTRIBUTION:

1	MS 0359	D. Chavez, LDRD Office, 1911
1	MS 0899	Technical Library, 9536 (electronic copy)

Sandia National Laboratories